

MASTER THESIS FOR THE ACQUISITION OF THE ACADEMIC DEGREE
MASTER OF SCIENCE IN PHYSICS

Space- and Polarization-Resolved Investigations of Rear Side Optical Radiation from High-Intensity Laser-Solid Interaction



**FRIEDRICH-SCHILLER-
UNIVERSITÄT
JENA**

Physikalisch-Astronomische Fakultät

Sebastian Hell

born on July 25, 1997, in Heilbronn (Germany)

This Master thesis has been carried out by Sebastian Hell at the Institute of Optics and Quantum Electronics in Jena under the supervision of **Prof. Dr. Malte C. Kaluza** and **Dr. Yasmina Azamoum**.

DECEMBER 2021

Abstract

Thin aluminum foils ($0.4 - 8\mu\text{m}$) have been irradiated by laser pulses at relativistic intensities. Hot electrons, which are periodically accelerated in the laser field at the foil front side, emit coherent optical radiation (COR) at the foil rear side. COR has been investigated space- and polarization-resolved to study hot electron transport through dense matter. This is important for further progress in laser-driven ion acceleration and fast ignition inertial confinement fusion. The COR's source size increased from $1.2\mu\text{m}$ to $2.3\mu\text{m}$ with foil thickness. This is significantly smaller than the laser focal width of $4\mu\text{m}$ and therefore indicates that pinching or filamentation influenced the propagation of the diverging hot electron current. The strong increase of the COR energy at the laser wavelength $\lambda_L = 1030\text{nm}$ and $\lambda_L/2$ with laser intensity I_L has been explained by considering an intensity dependent hot electron number N and temperature T_h in a coherent transition radiation (CTR) model. Fitting this CTR model to the experimental data allowed to determine T_h which increases with I_L but slower than expected. The CTR model fits also showed that $\approx 40\%$ of the hot electrons have been accelerated at the laser frequency ω_L and $\approx 60\%$ at $2\omega_L$, without significant changes with I_L . Hence, hole boring must have deformed the plasma surface. The COR's polarization, measured at $2\omega_L$, shows strong spatial changes along the COR emission region and varies with I_L , foil thickness and the COR's source size at the foil rear surface.

Zusammenfassung

Dünne Aluminiumfolien ($0.4 - 8\mu\text{m}$) wurden mit Laserpulsen bei relativistischen Intensitäten bestrahlt. Heiße Elektronen, welche periodisch im Laserfeld an der Folienvorderseite beschleunigt werden, emittieren kohärente optische Strahlung (COR) an der Folienrückseite. COR wurde orts- und polarisationsaufgelöst untersucht um den Transport heißer Elektronen durch dichte Materie zu untersuchen. Dies ist wichtig für weitere Fortschritte in lasergetriebener Ionenbeschleunigung und schnellzündender Trägheitsfusion ist. Die Quellgröße der COR nimmt von $1.2\mu\text{m}$ zu $2.3\mu\text{m}$ mit der Foliendicke zu. Dies ist signifikant kleiner als die Laserfokusgröße von $4\mu\text{m}$ und deutet daher darauf hin, dass Einschnürung oder Filamentierung die Propagation des divergierenden heißen Elektronenstroms beeinflussen. Der starke Anstieg der emittierten COR Energie bei der Laserwellenlänge $\lambda_L = 1030\text{nm}$ und $\lambda_L/2$ mit der Laserintensität I_L wurde durch Verwendung einer intensitätsabhängigen Anzahl N und Temperatur T_h der heißen Elektronen in einem Modell für kohärente Übergangsstrahlung (CTR) erklärt. Das Fitten dieses CTR Modells an die experimentellen Daten erlaubte die Temperatur der heißen Elektronen zu bestimmen, welche mit der Laserintensität I_L ansteigt, jedoch langsamer als erwartet. Außerdem zeigen die CTR Modell-Fits, dass $\approx 40\%$ der heißen Elektronenpakete bei der Laserfrequenz ω_L und $\approx 60\%$ bei $2\omega_L$ erzeugt wurden, ohne signifikante Änderungen mit I_L . Daher muss die Plasmaoberfläche durch Lochbohrung deformiert worden sein. Die Polarisation der COR, gemessen bei $2\omega_L$, zeigt starke räumliche Unterschiede entlang der COR Emissionsregion und variiert mit Laserintensität, Foliendicke und Quellgröße der COR auf der Folienrückseite.

Acknowledgment

The present thesis would not have been possible without the great support of colleagues, friends and family. These people I owe a lot and I therefore want to thank all who encouraged, supported and motivated me during the last year.

First, I would like to thank Prof. Dr. Malte C. Kaluza who allowed me to work on this fascinating topic in the relativistic laser physics group. I'm very grateful for his technical support and the good discussions which motivated me to deeply analyze the experimental data in search for interesting insights into laser-plasma physics. I owe him the great opportunity to further develop my strengths and knowledge.

Moreover, I want to thank Dr. Yasmina Azamoum for her great and encouraging supervision as well as her help in the experiments. It is rare to find someone with so much passion for a detailed understanding of things in order to give good advice. From her, I learned a great deal about scientific work and good writing.

Next, I would like to express my special thanks to Dr. Georg A. Becker for his great patience with my countless questions, his good suggestions and the great technical support. Without him I would not have learned so much about optics and laser-plasma physics. Moreover, I would like to thank him for his help in the lab and in the experiment.

A functioning laser is the basis for every laser-plasma experiment. Hence, I would like to thank Marco Hellwing and Dr. Marco Hornung for the time and effort they put into enabling the experiments of this thesis. Their work has been essential for the experiments conducted in the present thesis. Furthermore, I want to thank both of them for the interesting conversations we had about physics, lasers and life. Thanks to them, I learned a lot about lasers, pulse compressors and high-intensity laser systems.

I also want to express my special thanks to Dr. Marco Hornung for the great time I had in our shared office. It is rare to find such an empathetic and great person like him.

Next, I would like to thank Alexander Kessler for his help with camera, computer and network issues and Frank Schorcht for his technical support.

A warm word of thanks goes to Carola Zepter for her helpful comments on some sections of this thesis and to Matthew Schwab for the interesting discussions. Furthermore, I would like to thank Dr. Joachim Hein for providing a powerful server to run the calculations which have been presented in this thesis. His server made it possible to try a large variety of different parameter combinations which is essential for a systematic investigation.

An open and pleasant atmosphere is very important for successful work. In that sense, I would like to thank the whole relativistic laser physics group for the warm welcome, the good time and the nice and interesting talks that I had with you from time to time.

Ein riesiges Dankeschön geht an meine Freunde, für die unzähligen schönen Momente,

den riesen Spaß den wir immer gemeinsam haben und das offene Ohr und die warmen Umarmungen mit denen ihr immer für mich da wart. Zu guter Letzt möchte ich von ganzem Herzen meiner Familie danken. Eure Liebe und bedingungslose Unterstützung sind meine größte Inspiration und der Fels der mich auch in schwierigen Zeiten trägt. Ohne euch hätte ich es nie so weit geschafft. Ich bin unendlich dankbar, dass es euch gibt und ich mich immer auf euch verlassen kann.

Contents

Abstract	iii
1. Introduction	1
2. Basics of Laser-Solid Interaction	3
2.1. Ionization Mechanisms for Plasma Creation	3
2.2. Basic Plasma Properties	5
2.3. Laser Absorption in a Plasma	8
2.3.1. Absorption Mechanisms for Intense and Short Laser Pulses	8
2.3.2. Hot Electron Generation	10
2.4. Hot Electron Propagation in Overdense Plasmas	11
2.4.1. Return Current, Divergence and Self-Generated Fields	11
2.4.2. Transport Instabilities, Filamentation, and Recirculation	12
2.5. Optical Radiation from Hot Electrons in High-Intensity Laser-Plasma Interac- tions	13
2.5.1. Synchrotron Radiation (SR)	14
2.5.2. Transition Radiation (TR)	17
2.5.3. Coherent TR and Coherent SR from a Hot Electron Current	20
3. Methods	29
3.1. Experimental Setup	29
3.2. Laser, Plasma Mirror and Target	30
3.3. Rear-Side Optical Radiation Diagnostics	33
3.3.1. Imaging	33
3.3.2. Wollaston Prism	37
4. Experimental Investigation of Optical Rear Surface Radiation	41
4.1. Exemplary Camera Images of Coherent Optical Radiation (COR)	42
4.1.1. Shape and Position of the COR Intensity Distribution	44
4.1.2. COR Spatial Intensity Distribution for Different Target Thicknesses and Spectral Regions	46
4.1.3. Space-Resolved Polarization of COR	49
4.2. Scaling of COR Energy with Laser Intensity	49
4.2.1. Intensity Scaling of COR Energy: CTR Model	52
4.2.2. Energy Ratio of COR Emitted at 515 nm to COR Emitted at 1030 nm	55
4.3. Scaling of COR Energy with Target Thickness	56
4.3.1. Results of the CTR Model Fit	57

4.3.2. Variations of the Hot Electron Temperature and the Laser Absorption with Laser Intensity	60
4.4. Polarization Characteristics of COR	62
4.4.1. Experimental Results	62
5. Conclusion	65
Bibliography	67
Acronyms	81
Mathematical Notation	83
A. Light and Lasers	89
A.1. Spatial Characteristics of High-Intensity Laser Pulses	90
A.2. Temporal Characteristics of High-Intensity Laser Pulses	91
A.3. Chirped Pulse Amplification	93
B. A Brief Description of Coherent Wake Emission	95
C. Exemplary Calculated CTR Spectra	97
D. Calculations of Polarization Characteristics of COR	99
D.1. Simulation Model	99
D.1.1. Hot Electron Distribution Function	99
D.1.2. Electron Trajectory Model for SR	101
D.1.3. Acceptance Cone of Microscope Objective	103
D.1.4. Numerical Evaluation and Parameters	103
D.2. Results of Simulations and Comparison to Experiment	106
E. Additional Experimental Data	111
Selbstständigkeits- und Nutzungserklärung	117

1. Introduction

For thousands of years, humans have been fascinated by light and curious to reveal its nature. As the eye is our most important sensory organ, this curiosity about light comes not by surprise. Accordingly, light is the most valuable source of information that we have about the world we live in. However, the sensitivity and magnification of the eye is limited. Nonetheless, the developments of the most important principles and instruments of geometrical optics in the 17th century, like telescopes and microscopes, allowed mankind to reach beyond the limitations of the human eye. Around 200 years later, the propagation of light was explained by describing light as an electromagnetic wave. However, it needed the development of quantum physics in the beginning of the 20th century to acquire an uniform theoretical description and understanding of light ([1, 2] and references within). It was at that time, that A. EINSTEIN proposed the idea of stimulated emission [3–5] which laid the foundation for the development of lasers [6]. Since their proposal [7] and first realization [8, 9], lasers have become an indispensable part of our lives due to their broad range of applications in medicine (e.g. for surgery), in industry (e.g. cutting and welding of metals and glasses), in optical communication using fiber optics, in information storage (e.g. on CDs, DVDs or blue-ray discs) and in scientific research [10].

With the invention of Chirped Pulse Amplification (CPA) in 1985 [11], table-top IR lasers became capable of reaching relativistic intensities of the order of 10^{18} W/cm^2 at which the quiver motion of electrons exposed to the laser field becomes relativistic [10]. If such high-intensity lasers are focused onto targets made of solids or gases, energetic particles such as electrons [12], positrons [13], protons and heavy ions [14–18], neutrons and x-rays [19–24] and γ -rays [25] are produced after rapid ionization of the target by the laser.

Laser-driven energetic ion beams [14–18], for instance, are of interest to cancer therapy [26, 27] but also have various other applications [28–37]. Compared to conventional ion accelerators, laser-driven ion beams provide very small effective source sizes [38–46] and ultra-short ion bunches which are only several picoseconds long [47]. Furthermore, the acceleration gradients of laser-driven ion accelerators are of the order of $\text{MeV}/\mu\text{m}$ and therefore orders of magnitude larger than the acceleration gradients of $\sim \text{MeV/m}$ of conventional (radio frequency wave based) accelerators [48]. However, the success of sheath-accelerated ion beams [15–18] depends crucially on the transport of large currents of energetic ($W_{\text{kin}} \approx \text{MeV}$), relativistic electrons. These hot electrons have been accelerated by the laser and set up an electric field at the target rear side which accelerates the ions.

Another application of high-intensity lasers which requires the transport of large currents of energetic electrons is Fast Ignition (FI) in Inertial Confinement Fusion (ICF). FI ICF is an approach to fusion energy proposed by M. TABAK *et al.* in 1994 [49]. In ICF, the surface

of a spherical solid target is ablated by an high-intensity laser pulse. The pressure of the ablation causes an implosion and compression of the target. In that way, the high densities and temperatures needed for fusion are reached. FI ICF is based on using a laser-accelerated, energetic beam of electrons to deliver energy and hence ignite the compressed fuel to start fusion. The success of FI ICF requires energetic electrons to be transported through several hundreds of micrometer of very dense plasma without significant divergence or energy loss to ignite the compressed deuterium-tritium fuel [50, 51].

There are several promising routes towards improving the understanding of electron transport through an overdense plasma which is needed for the success of laser-driven ion acceleration and FI ICF: One can probe the laser-plasma interaction with an additional laser pulse [52–55] or study the various types of radiation emitted by hot electrons, depending on their energy. Such radiation was investigated in different spectral regimes, like K_α and extreme ultraviolet (XUV) emission [56–61], coherent radiation at multiples of the laser frequency [62–65] or coherent radiation close to or in the visible spectral regime [66–77].

This thesis builds on the ideas of previous research [66–77] and examines the optical radiation emitted by hot electrons to investigate their acceleration in the laser field at the target front surface and their propagation through the target. In the experiments of this thesis, ultra-short laser pulses, provided by the POLARIS laser system at the Helmholtz Institute in Jena, were focused onto thin aluminum (Al) foils to reach intensities of up to $3 \times 10^{19} \text{ W/cm}^2$. The investigated target thicknesses range from $0.4 \mu\text{m}$ to $8 \mu\text{m}$. The coherent optical radiation (COR) emitted by hot electrons was measured space- and polarization-resolved in different spectral regimes (wavelengths between 500 nm and 1100 nm) via imaging the target rear surface radiation onto three cameras equipped with different spectral filters.

This thesis is organized as follows: A brief introduction to the basics of laser-plasma interaction is given in chapter 2. This includes a discussion of the hot electron generation and propagation as well as the radiation processes induced by these hot electrons in laser-plasma interactions. In chapter 3, the methods, which were employed to measure and analyze the COR emitted by hot electrons at the target rear surface in the experiment, are presented. Chapter 4 is dedicated to the results of the experimental investigations of rear surface COR in high-intensity laser-solid interactions. First, some exemplary camera images of COR are presented and discussed. Next, the total pixel count of these images, being proportional to the total emitted COR energy per laser shot, is investigated as a function of laser intensity and target thickness. In comparison to most of the previous research, laser intensity and target thickness are both varied during the experimental investigation. In that way, the influence of laser intensity and target thickness on the COR emission can be studied and a broader picture of the hot electron acceleration and propagation can be acquired. Furthermore, the polarization of COR was measured spatially resolved and its dependence on laser intensity, target thickness and the COR's source size was investigated. To the best of the author's knowledge, there is only one comparable study where the polarization of CTR was investigated [75]. In the last chapter, the results of this thesis are summarized and a brief outlook on prospective investigations is given.

2. Basics of Laser-Solid Interaction

This thesis deals with the coherent optical radiation (COR) produced by accelerated electrons in the interaction of a very intense, ultrashort laser pulse with an overdense plasma, created from thin aluminum foil targets. Whereas the physical framework of lasers is discussed in more detail in appendix A, this chapter rather focuses on the interaction between laser light and matter. Lasers (an abbreviation for Light Amplification by Stimulated Emission of Radiation) allow the concentration of light in very small volumes to achieve extremely high intensities of up to 10^{22} W/cm^2 [78, 79]. Focusing such an intense laser pulse onto dense matter like a liquid or a solid target creates a plasma as the matter is ionized by the laser. Compared to gases, ionizing solid or liquid targets results in an overdense plasma for lasers with a wavelength of $\lambda_L \approx 1 \mu\text{m}$, i.e. the laser cannot propagate through the plasma but is reflected. During the interaction of the laser pulse with an overdense plasma, a fraction of the laser is absorbed and heats the plasma [80]. The laser absorption is closely related to the acceleration of electrons to very high velocities [81]. These energetic electrons produce COR [62, 64–77, 82, 83] and therefore an introduction to the concepts relevant to the understanding of laser-plasma interaction is given in the following.

The present chapter is structured as follows. First, ionization mechanisms and general plasma properties are discussed. Next, the laser absorption by the plasma and the consequent generation and propagation of energetic electrons is considered. Finally, an overview over the characteristics of the optical radiation emitted by these fast electrons at the target rear surface is given.

2.1. Ionization Mechanisms for Plasma Creation

Ionization is the creation of free electrons and ions. Ionization requires the transfer of energy to the bound electron to free it from the potential of the atomic core. The required energy transfer for ionization can be caused for instance through collisions or the absorption of photons [84]. To classify the mixture of charged and neutral particles, created by ionization, as a plasma, several conditions must be fulfilled [85] which are described in section 2.2. First, the different models of photoionization are described in the following.

Photoelectric Effect As explained by A. EINSTEIN in 1906 [86], an absorbed photon transfers all its energy $h\nu$ to one electron, where h is the Planck constant and ν the frequency of the incident light. The atom is then ionized if the photon energy which is absorbed by the electron is larger than the work function U_{wf} of the solid. The energy difference $h\nu - U_{\text{wf}} =$

W_{kin} corresponds to the maximum kinetic energy W_{kin} of the released electron (the "photo electron"). For gases, the work function U_{wf} is replaced by the ionization potential U_{ion} .

In the framework of this "classical" photoelectric effect, an atom cannot be ionized if the energy of an incident photon is smaller than the potential of the atomic core. The POLARIS laser, for instance, operates at a central wavelength of 1030 nm and hence provides photons with an energy of $W_{\text{ph}} \approx 1.2 \text{ eV}$. According to the photoelectric effect, no ionization should occur if an Aluminum (Al) foil with a work function of $U_{\text{wf}} \approx 4.2 \text{ eV}$ (for the first ionization) [87] is irradiated by the POLARIS laser. However, other ionization mechanisms become probable if the light intensity is drastically increased to above 10^{12} W/cm^2 for a laser with a wavelength of $1 \mu\text{m}$ [88]. In this case, the ionization is induced by the strong field of the laser which is well described by the Keldysh theory [89].

Multi-Photon Ionization (MPI) The invention and development of lasers allowed focusing of light to such high intensities that the interaction of more than one photon with one atom becomes probable. In this situation, a bound electron can absorb several photons to overcome the ionization potential, as depicted in Fig. 2.1a. To account for MPI, the condition for ionization from the photoelectric effect is therefore slightly modified to $j \cdot h\nu = U_{\text{ion}} + W_{\text{kin}}$, where j is the number of absorbed photons by one electron. The ionization rate Γ_j is then given as $\Gamma_j = \sigma_j \cdot I_L^j$, where σ_j corresponds to the j -photon ionization cross-section and I_L is the laser intensity [80].

Tunnel Ionization (TI) If the intensity is further increased, the electric field E of the laser perturbs the atomic potential, as illustrated in Fig. 2.1b, and a potential barrier forms. The resulting potential $U(x)$ of an atomic core with positive charge Ze which is exposed to the electric field E of a laser is given by

$$U(x) = -\frac{Ze^2}{4\pi\epsilon_0|x|} - eEx. \quad (2.1)$$

In this one-dimensional model, x is the spatial position. Moreover, e is the absolute electric charge of an electron (and proton) and ϵ_0 corresponds to the vacuum permittivity. If the electron successfully tunnels through this potential barrier $U(x)$, the atom becomes ionized. In the Wentzel, Kramers and Brillouin approximation (WKB), the tunnel rate Γ_{tunnel} fulfills

$$\Gamma_{\text{tunnel}} \propto \exp\left(-\frac{2}{\hbar} \left| \int_{x_1}^{x_2} \sqrt{2m_e(U(x) - U_{\text{ion}})} dx \right| \right), \quad (2.2)$$

with the positions x_1 and x_2 where $V(x_{1,2}) = U_{\text{ion}}$ and the electron rest mass m_e [90, 91].

Over-The-Barrier Ionization (OTBI) After the discussion of tunnel-ionization, it is natural to ask about the consequences of increasing the laser intensity even further. It turns out that increasing the intensity to values above 10^{13} W/cm^2 leads to a stronger suppression of the potential barrier. If the potential barrier of the atomic core is sufficiently low, the electron can freely escape the potential [92] as shown in Fig. 2.1c. The threshold intensity above

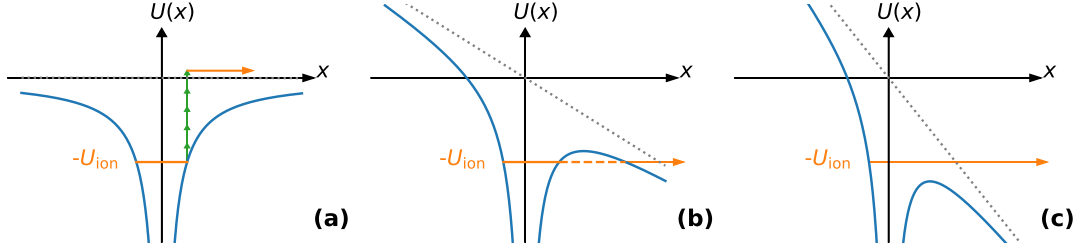


Figure 2.1.: The influence of a laser field (dotted gray line) on the Coulomb potential (blue line) to illustrate different ionization processes. With increasing intensity, the dominating ionization mechanism changes from the photoelectric effect (not displayed here) to Multi-Photon Ionization (a) and Tunnel Ionization (b). If the electric field of the laser is strong enough, Over-The-Barrier Ionization (c) dominates.

which OTBI occurs is given as $I_{\text{OTBI}} = \frac{c\epsilon_0(4\pi\epsilon_0)^2}{32Z^2e^6} U_{\text{ion}}^4$ for the Z^{th} electron, where c is the speed of light in vacuum [80, 90].

Keldysh Parameter The two domains of MPI and TI, both described in the Keldysh theory [89], can be distinguished by the Keldysh parameter $\xi = \sqrt{U_{\text{ion}}/2U_P}$ with the ionization potential U_{ion} and the ponderomotive potential $U_P = \frac{e^2}{4m_e\omega_L^2} E_s^2$. The ponderomotive potential corresponds to the kinetic energy averaged over one optical period $\mathcal{T}_L = 2\pi/\omega_L$ of an electron oscillating in the laser field. Here, E_s is the temporally averaged absolute electric field of the laser and $\omega_L = 2\pi\nu_L$ is the angular laser frequency. For $\xi < 1$, TI dominates, whereas for $\xi \gg 1$ MPI prevails. However, if ξ is small enough, the threshold intensity for OTBI is surpassed and the electron is ionized by OTBI instead of TI [90, 91]. In general, not only the electric field strength varies during the laser-matter interaction but also the ionization potential differs for electrons in different shells. Hence, the ionization of matter by a high-intensity laser may occur as a combination of MPI, TI, and OTBI [91].

In Eq. 2.1, the electric field strength E of the laser is assumed to be constant during tunneling. This assumption is only valid if the Keldysh time $\tau_\xi = \xi/\omega_L$ is much smaller than the optical period \mathcal{T}_L , thus for $\xi = 2\pi\tau_\xi/\mathcal{T}_L < 1$. Depending on the ionization potential and the laser intensity, this assumption ($E = \text{const.}$) usually fails for $\lambda_L \ll 1\mu\text{m}$ [90, 91].

2.2. Basic Plasma Properties

The last section was dedicated to ionization, which describes the creation of a mixture of charged (and neutral) particles due to the interaction between light and matter. Such a mixture is called a plasma if it is macroscopically neutral and shows collective behavior due to long-range electromagnetic forces [93].

In a thermal equilibrium, the particle velocities follow a Maxwellian distribution (in the nonrelativistic case) and the average kinetic energy in three dimensions is $W_{\text{kin}} = \frac{3}{2}k_B T$. Consequently, it is clear that the plasma electrons and ions recombine if the plasma temperature T drops and the thermal energy is not sufficiently large to withstand the electrostatic potential of the charge separation in a plasma [93]. In a laser-produced plasma the relax-

ation time and thus the lifetime of the plasma is typically of the order of the electron-ion relaxation time

$$\tau_{ei} = \frac{m_i}{2m_e} \frac{1}{\nu_{ei}}, \quad \nu_{ei} \simeq (1-2) \cdot 10^{-5} \frac{Z^2 n_i [\text{cm}^{-3}]}{(T_h [\text{eV}])^{3/2}} [\text{s}^{-1}], \quad (2.3)$$

with the electron-ion collision frequency ν_{ei} and the ion charge Z in units of e [94]. For a fully ionized aluminum plasma and the typical parameters of the experiments presented in this thesis ($I_L = 10^{19} \text{ W/cm}^2$, $\lambda_L = 1030 \text{ nm} \rightarrow T_e \approx 0.4 \text{ MeV}$ (Eq. 2.13)) the relaxation time at the critical density n_{cr} (Eq. 2.7) is calculated to be of the order of microseconds which is much longer than the laser pulse duration.

The meaning of the term "macroscopically neutral" in the plasma definition is closely related to the concept of Debye Shielding. Such shielding is the fundamental ability of a plasma to shield electric potentials which have been applied to it. If, for instance, a positive charge is placed in a plasma, then the electrons arrange themselves around this charge to shield its electrostatic potential U_0 . In an one-dimensional model, the resulting electrostatic potential is

$$U(x) = U_0 \exp(-|x|/\lambda_D), \quad \text{with } \lambda_D = \left(\frac{\epsilon_0 k_B T_e}{n_e e^2} \right)^{1/2}, \quad (2.4)$$

where the Debye length λ_D is a function of the electron density n_e (asymptotic density far away from plasma perturbation) and the electron temperature T_e with the Boltzmann constant k_B . Due to the smaller mass of electrons compared to protons ($m_e/m_p \leq 5.45 \times 10^{-4}$), the electrons move on a shorter timescale than the ions. Therefore, the faster electrons generally do the shielding in a plasma by moving to create a local deficit or surplus of negative charge. The plasma characteristic "macroscopically neutral" requires two conditions to be fulfilled. First, the spatial dimension of the system must be much larger than λ_D . Second, the particle mixture is neutral, i.e. the net resulting electric charge is zero ($\int n_i dV \simeq \int n_e dV$) on length scales of the order of the dimension of the system. However, this charge balance may be violated causing the local presence of electromagnetic forces. Moreover, for Debye shielding to be a statistically valid concept, there must be many particles in a "Debye sphere", so $N_D = n \frac{4}{3} \pi \lambda_D^3 \gg 1$ [93].

If a plasma in equilibrium is perturbed by displacing the plasma electrons from the uniform (slow) ion background, an electric field builds up which acts as a restoring force and pushes the electrons back to their equilibrium position. Together with the electron inertia, all necessary ingredients for an oscillation are present. Because of their much larger mass, the ions are considered immobile and the electrons oscillate at the plasma frequency around their equilibrium position. If thermal effects, magnetic fields and higher order terms are neglected, the equation of motion (e.o.m.) can be solved for an electron density, electron velocity, and electric field which oscillate longitudinally around an equilibrium value at the plasma frequency

$$\omega_p = \sqrt{\frac{n_{e,0} e^2}{m_e \epsilon_0}}, \quad (2.5)$$

where $n_{e,0}$ is the equilibrium electron density whereas the equilibrium velocity and the equilibrium electric field are zero. The plasma frequency describes also the time scale of electron

motion. Thus, the thermal velocity of an electron is of the order of $v_{\text{th}} = \omega_p \lambda_D$ [93].

As the group velocity $\frac{d\omega}{dk}$, with the wavenumber $k = 2\pi/\lambda$, is zero, the plasma oscillation does not propagate in case of infinite extended oscillating plane charge sheets. Confined plasma oscillations, however, propagate due to fringing fields which extend beyond the region of initial plasma disturbance and couple the disturbance to adjacent layers. In addition, also thermal motion causes the propagation of a plasma oscillation which is then called a plasma wave. Electron density gradients then translate to thermal pressure gradients in the e.o.m. and the dispersion relation for the linearized problem becomes $\omega^2 = \omega_p^2 + \frac{3}{2}k^2 v_{\text{th}}^2$, with the thermal velocity $v_{\text{th}} = (2k_B T_e / m_e)^{1/2}$ [93].

As this thesis deals with laser-plasma interaction, one should discuss the propagation of electromagnetic waves in the medium plasma. In comparison to light propagation in vacuum, the current density \vec{j} is not zero anymore and must be considered in the Maxwell equations. Due to the high frequency of laser light, the ions can be considered as fixed and the current density is given by the electron motion, so $\vec{j} = -n_{e,0} e \vec{v}_e$. The linearized e.o.m. derived from the Maxwell equations can then be solved by transverse waves to arrive at the dispersion relation

$$\omega^2 = \omega_p^2 + c^2 k^2 \quad (2.6)$$

for electromagnetic waves in a plasma. For $\omega < \omega_p$, the wavenumber k in Eq. 2.6 becomes imaginary and therefore only light with $\omega > \omega_p(n_e)$ can propagate in a plasma [93].

When a short laser pulse is focused onto a thin foil, the rising edge of the laser pulse ionizes the foil to produce a high-density plasma which reflects the laser pulse. During the laser-plasma interaction, energy is transferred from the laser to the plasma, as discussed in the next section. Therefore, the plasma expands due to the plasma pressure at the speed of sound $c_s = \sqrt{k_B(Z^* T_e + T_i)/m_i}$, with the effective ion charge Z^* , the ion mass m_i , and the temperature $T_{e,i}$ of the electron and ion population [88]. Assuming an exponentially decreasing plasma density at the front surface of the foil and isothermal plasma expansion, the laser pulse interacts with a plasma exhibiting a scale length of $L = c_s \tau_{L,\text{ion}}$, where $\tau_{L,\text{ion}}$ is the pulse length of the ionizing part of the laser. Thus, the laser pulse with frequency $\omega = \omega_L$ is reflected at the position x_{cr} where the electron density n_e equals the critical density

$$n_{\text{cr}}(\omega) = \epsilon_0 m_e \omega^2 / e^2. \quad (2.7)$$

Hence, light of a different frequency ω is reflected at a different position. For oblique incidence at angle θ_0 , the laser is reflected at the position where the electron density equals $n_{\text{cr}} \cos^2 \theta_0 < n_{\text{cr}}$. Correspondingly, the plasma is divided into an undercritical/underdense ($n_e < n_{\text{cr}}$) and an overcritical/overdense region ($n_e > n_{\text{cr}}$). Due to the frequency dependence of n_{cr} , a dense plasma which is for example opaque to an infrared (IR) laser may be transparent to radiation in the XUV regime. At the reflection point, the laser pulse tunnels into the overdense ($n_e > n_{\text{cr}}$) plasma over a characteristic skin depth $l_s = c/\omega_p$ [80]. In the undercritical plasma, the laser experiences a refractive index

$$\eta(\omega) = \sqrt{\epsilon(\omega)} = c/v_{\text{ph}} = \sqrt{1 - n_e/n_{\text{cr}}} = \sqrt{1 - \omega_p^2/\omega^2}, \quad (2.8)$$

with the dielectric constant $\epsilon(\omega)$ of the plasma, as a function of the frequency ω . At relativistic intensities, the effective plasma frequency is lowered and the critical density is enhanced as the electron mass increases from m_e to $\gamma_e m_e$ with the relativistic factor $\gamma_e = (1 - \beta_e^2)^{-1/2}$ and the normalized velocity $\beta_e = v_e/c$ [80]. Thus, the relativistic laser pulse can propagate further into the plasma in a process called relativistic self-induced transparency [95, 96].

2.3. Laser Absorption in a Plasma

To discuss the interaction of the plasma constituents with the EM field of a laser, we consider the Lorentz equation

$$\frac{d\vec{p}}{dt} = q(\vec{E} + \vec{v} \times \vec{B}) , \quad (2.9)$$

which describes the change of momentum \vec{p} of a particle with charge q and velocity \vec{v} in the presence of an electromagnetic field. Due to the much higher mass of ions compared to electrons, direct interaction between the plasma and the short laser pulse is governed by the electrons [80]. As the optical radiation at the target rear side is created by fast electrons, it is important to understand how the laser pulse transfers energy to the electrons.

The strongly simplified model of an electron in an infinitely extended plane EM wave cannot explain the energy gain of electrons after the laser pulse has passed. Therefore, we additionally take into account the ponderomotive force for a focused laser pulse: An electron which oscillates in the laser field tends to move towards a position where its temporally averaged kinetic energy (ponderomotive potential) U_P is lower. Hence, the ponderomotive force is given by

$$\vec{F}_P = -\vec{\nabla} U_P = -\frac{e^2}{4\langle\gamma_e\rangle m_e \omega_L^2} \vec{\nabla} (\vec{E}_s^2) , \quad (2.10)$$

where \vec{E}_s contains the spatial dependencies of the electric component of the laser field and $\langle\gamma_e\rangle$ is the relativistic γ -factor of an electron, averaged over an optical laser cycle. Thus, the ponderomotive force accelerates electrons out of regions of high intensity [80, 94]. Nevertheless, the presence of many electrons in an overdense plasma and the strong confinement of laser energy in space and time requires more sophisticated models of plasma heating, as presented in the following, to explain the origin of accelerated electrons in laser-solid experiments.

2.3.1. Absorption Mechanisms for Intense and Short Laser Pulses

Collisional Absorption The plasma electrons are accelerated by the electric field of the laser pulse and perform oscillations. These oscillations are damped by collision with ions (and electrons) which transfers energy from the laser to the plasma [80]. In the limit of a perfect density step, the situation corresponds to the Fresnel-like absorption of metal optics in case of a finite conductivity [97]. At higher laser intensities, the plasma temperature rises quickly and the collision frequency ν_{ei} (Eq. 2.3) is reduced. The effective collision frequency is further reduced if the quiver velocity becomes comparable to the thermal velocity at higher intensities. Thus, collisional absorption becomes ineffective at intensities

above 10^{15} W/cm^2 . To explain the experimentally observed high absorption efficiency above 10^{15} W/cm^2 , collisionless absorption mechanisms must be considered which are discussed in the following [80]. The behavior of a collisionless plasma is dominated by long-range electro-magnetic forces instead of ordinary local collisions which can be neglected [93].

Resonance Absorption This absorption mechanism is based on a non-zero electric field component of a p-polarized laser light wave along the target normal, usually present at oblique laser incidence. The laser field tunnels to the critical density $n_e = n_{\text{cr}}$ where it can resonantly excite a plasma wave as $\omega_p(n_e = n_{\text{cr}}) = \omega_L$. The plasma wave then travels into the overdense target where it is eventually damped by electron-ion collisions at low intensity or by particle trapping or wave breaking in case of higher intensities. In that way, the laser transfers energy to the plasma via the plasma wave [80, 98]. At very high intensities, the ponderomotive force overcomes the thermal pressure and pushes the plasma surface substantially inwards in a process called hole boring. Hence, resonance absorption can also occur at normal laser incidence if hole boring deformed the plasma surface and therefore there exists a locally nonzero electric field component normal to the plasma surface [99]. The efficiency of resonance absorption depends on the angle of incidence and the plasma density scale length L [80, 94]. In general, the resonance absorption stops to work in its usual form at steep density gradients and high laser intensities. In such a situation, the resonance of the plasma wave breaks down if the oscillation amplitude of the electrons exceed the density scale length L and a slightly different absorption mechanism, called vacuum heating, becomes relevant [80].

Vacuum Heating In a plasma with a steep density gradient, the electrons are directly exposed to the laser. The laser light wave penetrates only to a skin depth $\sim c/\omega_p$ into the overdense plasma. Like for resonance absorption, vacuum heating requires a non-zero electric field component of the p-polarized laser normal to the target surface. Thermal electrons which arrive at the plasma surface at the right moment during a laser cycle are then dragged out of the plasma, way beyond the thermal Debye length. When the electric field of the laser changes its direction, the corresponding electric force acting on the electrons points towards the plasma. Hence, the electrons are accelerated back into the plasma due to combined electric fields from charge separation and the laser electric field momentarily pointing towards the target. Inside the plasma, the accelerated electrons propagate free from the influence of the laser. Usually, the accelerated electrons from resonance absorption and vacuum heating (also called Brunel heating [100]) are directed parallel to the density gradient of the plasma.

Relativistic $\vec{j} \times \vec{B}$ heating This plasma heating mechanism, first discussed in 1985 by W. L. I. KRUEER and K. ESTABROOK [101], is quite similar to vacuum heating. However, now the $\vec{j} \times \vec{B}$ component of the Lorentz force is the driving term which accelerates electrons directly at twice the laser frequency along the propagation direction of the laser. These fast electrons are then eventually absorbed via collisions and heat the plasma. For a linearly polarized wave with the electric field $E = E_0(x)\hat{y}\sin\omega t$, the ponderomotive force in \hat{x} -direction acting

on one electron is

$$F_p = -\frac{m_e}{4} \frac{\partial \nu_{os}^2(x)}{\partial x} (1 - \cos 2\omega t) \hat{x}, \quad (2.11)$$

where ν_{os} is the oscillation velocity of the electron due to the electric force of the laser field. The first term in Eq. 2.11 pushes the electron density profile inwards, as described earlier, while the second term makes the electrons at the plasma-vacuum interface oscillate along the propagation direction of the laser pulse [80]. Electrons with the "correct" phase, with respect to the driving force F_p , may receive a "nonadiabatic kick" into the overdense plasma and escape the influence of the laser field. However, the fraction of electrons which escapes the plasma oscillation and propagates into the overdense plasma depends on the strength of the oscillating ponderomotive force [88]. The $\vec{j} \times \vec{B}$ heating becomes relevant at relativistic electron quiver velocities ($a_0 \geq 1$) and works for non-circular polarization. Moreover, the efficiency of $\vec{j} \times \vec{B}$ heating is the largest at normal laser incidence [80].

2.3.2. Hot Electron Generation

Via collisionless laser absorption, a certain fraction of electrons is accelerated to much higher energies $k_B T_h$ than the initial bulk plasma temperature $T_e \ll T_h$ [80, 81]. These so called hot (or fast) electrons exhibit a Maxwellian velocity distribution due to the stochastic nature of their acceleration with cycle-to-cycle fluctuations in electron trajectories and hence acquired energies [81]. At relativistic intensities, however, the Maxwell-Jüttner distribution [102] needs to be considered instead to describe the energy distribution of fast electrons.

To estimate the hot electron temperature T_h from the laser parameters in the focus, different scaling laws are available which vary due to the different assumptions considered in modeling the plasma heating [80]. The experiments in this thesis mostly deal with relativistic intensities and normal laser incidence and therefore $\vec{j} \times \vec{B}$ heating is expected to dominate the absorption process. At relativistic intensities, it is argued [99] that the hot electron temperature is proportional to the ponderomotive potential which corresponds to the temporally averaged kinetic energy of the oscillating electrons. Therefore, the relevant scaling law for T_h , corresponding to the $\vec{j} \times \vec{B}$ heating mechanism, is expressed as follows:

$$k_B T_h \simeq m_e c^2 (\langle \gamma \rangle - 1) \simeq 511 [\text{keV}] \left(\sqrt{1 + a_0^2} - 1 \right), \quad \text{with } a_0 = \frac{e E_0}{\omega_L m_e c} = \sqrt{0.73 I_{18} \lambda_\mu^2}. \quad (2.12)$$

Here, a_0 is the amplitude of the normalized vector potential \vec{a} of the electromagnetic field¹, as defined in appendix A. Moreover, E_0 refers to the amplitude of the electric field of the laser, I_{18} corresponds to the laser intensity in units of $10^{18} \text{ W cm}^{-2}$ and λ_μ is the wavelength in μm [80]. The ponderomotive scaling in Eq. 2.12 is consistent with simulations and experiments [106, 107].

As noted in [103], the ponderomotive scaling (Eq. 2.12) is, however, not valid at relativistic intensities $I \geq 10^{18} \text{ W/cm}^2$. Experimentally shown [108–110] for the range of 10^{18} W/cm^2

¹As pointed out in [103], the definition of $\langle \gamma \rangle$ is not consistent in literature. E.g. in [94, 104, 105] it is distinguished between linear laser polarization $\langle \gamma \rangle = \sqrt{1 + \langle \vec{a}^2 \rangle} = \sqrt{1 + a_0^2/2}$ and circular laser polarization $\langle \gamma \rangle = \sqrt{1 + a_0^2}$.

to 10^{21} W/cm², the hot electron temperature scales much weaker with laser intensity (e.g. $k_B T_h \propto (I_L \lambda_L^2)^{1/3}$ [108] or $k_B T_h \propto (I_L \lambda_L^2)^{0.4}$ [109]). This weaker scaling was explained by pre-plasma modifications due to the ponderomotive force of the laser [99, 111]. Moreover, M. G. HAINES *et al.* argues that the electrons escape the influence of the accelerating laser into the overcritical plasma before the maximum possible acceleration is experienced. Hence, the acquired energy of the hot electrons lies below the ponderomotive potential [112]. T. KLUGE *et al.* [113] developed a model which converges to the ponderomotive scaling for $a_0 \ll 1$ but shows a weaker scaling at relativistic laser intensities in good agreement with experiments and PIC simulations:

$$k_B T_h = m_e c^2 \left(\frac{\pi}{2\mathcal{K}(-a_0^2)} - 1 \right) \approx \begin{cases} m_e c^2 \frac{a_0^2}{4} & \text{for } a_0 \ll 1 \\ m_e c^2 \left(\frac{\pi a_0}{2\ln(16) + 2\ln(a_0)} - 1 \right) & \text{for } a_0 \gg 1 \end{cases}, \quad (2.13)$$

with the complete elliptical integral of first kind $\mathcal{K}(x) = \int_0^{\pi/2} [1 - x \sin^2(t)]^{-1/2} dt$ and the natural logarithm $\ln(x)$. For $I_L = 10^{19}$ W/cm² and $\lambda_L = 1.03 \mu\text{m}$, Eq. 2.13 gives $T_h \approx 400$ keV.

2.4. Hot Electron Propagation in Overdense Plasmas

To understand the processes responsible for rear side optical emission from hot electrons in thin foils irradiated by an intense laser pulse, it is necessary to discuss the hot electron propagation through the target.

Collisions The fast electron transport, and hence its penetration depth, is affected by collisions with electrons and ions. Hot electrons can scatter and lose energy due to acceleration and consequent emission of radiation (Bremsstrahlung), usually in the x-ray regime. Moreover, the hot electrons can lose energy via excitation or ionization of atoms which also results in the emission of radiation [80]. In a solid density plasma, however, most collisions are due to the slow return current, as discussed in the next paragraph, because slow electrons lose energy through scattering more efficiently than fast electrons [81]. These collision-based energy loss mechanisms dominate at moderate laser intensities $< 10^{17}$ W/cm². At higher intensities, collisions have increasingly less influence on the hot electron transport and the hot electrons may reach the target rear side where they emit radiation as explained in section 2.5. However, self-generated electric and magnetic fields, induced by the highly energetic electron beam, need to be considered at higher laser intensities. Those self-generated fields act back on the hot electrons and influence their propagation through the target [80].

2.4.1. Return Current, Divergence and Self-Generated Fields

According to the Maxwell equations, a current of energetic electrons generates a magnetic field which deflects the electrons and, if intense enough, acts to reverse the electron current [81]. Therefore, the maximum electron current which is able to propagate in the absence of free charges (e.g. in vacuum) is given by the Alfvén limit $J_A \approx \beta \gamma m_e c^2 / e = \beta \gamma \cdot 1.7 \times 10^4$ A

[114]. Considering the focal spot size, the temperature of fast electrons and their total absorbed energy, the calculated hot electron current is, however, of the order of 10^6 A. Hence, the propagation of such a multi-MA current in plasma requires local current compensation through a return current density \vec{j}_{ret} . The return current is drawn from the background plasma electrons and contains many slow electrons propagating in the opposite direction of the fast hot electron current density \vec{j}_f to neutralize it such that $\vec{j}_f + \vec{j}_{\text{ret}} \approx 0$. In that way, the self-generated magnetic fields from \vec{j}_f and \vec{j}_{ret} cancel each other [80]. The hot electron current forms an Ohmic potential and therefore sets up an electric field which transfers energy to the return current in a process called Ohmic stopping. In a plasma with finite conductivity, the formation of a return current takes a longer time which can lead to the stopping and reflection of electrons by the induced electric field $\vec{E} = -\vec{j}_f/\sigma_e$, where σ_e corresponds to the conductivity [81].

For applications like FI ICF and laser-driven ion acceleration (e.g. via Target-Normal-Sheath-Acceleration (TNSA)), the electron beam divergence should be as low as possible. However, self-generated magnetic fields due to radial changes in the fast electron current density \vec{j}_f and the resistivity $\chi_e = \sigma_e^{-1}$ influence the divergence, as the Maxwell equations in combination with Ohm's law show:

$$\frac{\partial \vec{B}}{\partial t} = -\vec{\nabla} \times \vec{E} = \vec{\nabla} \times (\chi_e \vec{j}_f) = \chi_e (\vec{\nabla} \times \vec{j}_f) + (\vec{\nabla} \chi_e) \times \vec{j}_f, \quad (2.14)$$

where the first term on the right-hand side (RHS) results in pinching (reduction of beam radius) of \vec{j}_f , whereas the second term on the RHS in Eq. 2.14 pushes electrons away from the beam center (beam hollowing) [81].

2.4.2. Transport Instabilities, Filamentation, and Recirculation

The propagation of fast electrons through an overdense target can be further influenced by various transport instabilities. Among those, the electromagnetic Weibel-like filamentation is the main instability type of relevance to counter-streaming electron currents in an overdense plasma. The collisionless Weibel instability can be seeded by the return current and is based on the generation of self-reinforcing, localized magnetic fields (Eq. 2.14) which leads to electron beam breakup into filaments. The timescale of filament formation for the Weibel instability is $\Gamma_\omega^{-1} = \omega_f^{-1} (\gamma n_e/n_f)^{1/2} \beta_f^{-1}$ [s]. For the typical experimental parameters ($I = 10^{19}$ W/cm², $\lambda = 1030$ nm $\rightarrow \gamma = k_B T_h/m_e c^2 + 1 \approx 1.8$ with $T_h = 0.4$ MeV from Eq. 2.13), a typical fast electron density of $n_f = 0.01 n_e$ and assuming that the Weibel instability forms near the critical density at the target front side (thus $\omega_f = \omega_L$), the timescale of formation of a Weibel instability corresponds to a propagation length of $\approx 3 \mu\text{m}$. In case of a sufficient high transverse electron beam temperature, the Weibel instability can be suppressed by the thermal pressure. Other Weibel-like instabilities cause filamentation due to self-reinforcing modulations in resistivity or return current (ionization instability) [81].

If the electrons finally reach the target rear side, the most energetic electrons escape the target and set up a quasi-electrostatic space-charge sheath field at the target rear. This

sheath field reflects most of the fast electrons back towards the target front side. Here, a similar sheath potential forms which also reflects the electrons back into the target. Consequently, the electrons recirculate (or reflux) in the target. Additionally, the recirculation leads to lateral electron transport as the axial velocity is reduced at every electron reflection while the transverse velocity remains mostly unchanged [81]. If the laser pulse duration (during which electrons are accelerated) is much longer than the double transit time of the electrons through the target, the recirculating electrons overlap with the laser accelerated electrons. Hence, electron recirculation can lead to an enhanced electron density at the target rear side which results in enhanced proton energies in laser-driven ion acceleration [115].

2.5. Optical Radiation from Hot Electrons in High-Intensity Laser-Plasma Interactions

In this thesis, the optical radiation emitted by fast electrons is studied spatially and spectrally resolved to investigate the nature of this radiation and to gain information about the properties of the fast electron current which is responsible for the radiation in the first place. Therefore, a basic introduction to the theory of radiation emitted by fast electrons in laser-plasma interactions with overdense targets is given in this section.

In an experiment, more than one fast electron is accelerated and therefore the radiation from the single emitting electrons at the target rear side interferes. This interference consists of a coherent and an incoherent part (see Eq. 2.24). Due to the relatively large number N of fast electrons ($N \sim 10^{12}$ according to Eq. 4.1), the coherent optical radiation (COR) is usually orders of magnitude more intense in the investigated spectral range ($\lambda = 500\text{--}1100\text{ nm}$) than the incoherent part. Therefore, it is expected that COR dominates the radiation observed in the experiment. There are several mechanisms leading to the emission of electromagnetic radiation by hot electrons. In the following, these mechanisms are analyzed and it is deduced which types of radiation might explain the optical radiation observed in the experiments of this thesis.

Different Types of Radiation An energetic electron which moves through matter interacts with the Coulomb potential of the constituent atoms. As the electron is decelerated during such interactions (i.e. collisions), it emits radiation, called bremsstrahlung [81, 116]. Fast electrons can also cause fluorescence light during such collisions [56, 58]. However, due to the high energy of the laser-accelerated electrons of several hundred keV to MeV, the emitted bremsstrahlung and fluorescence (e.g. K_α [56, 58]) lies in the XUV and X-ray regime, far beyond the spectral range investigated in this work. Thermal radiation due to collisions between constituents of the hot plasma is incoherent (and unpolarized) [10] and therefore may contribute only to the background in the spectrum of COR emitted by fast electrons. Besides the collision-based emission phenomena presented so far, a charged particle moving at constant velocity through a medium excites an electric dipole moment in the atoms and molecules along its path. When the polarized atoms or molecules return to their original

states, electromagnetic radiation is emitted. The electromagnetic waves from such induced dielectric polarization interfere coherently to form a wave front if the particle's velocity is greater than the phase velocity $c/\sqrt{\epsilon(\omega)}$ of the light wave in the medium, as Huygens' principle illustrates [116–118]. This emission process is called Čerenkov radiation [119–124] and usually observed in a nuclear power station when energetic, charged particles move through water [125–127]. However, as $\sqrt{\epsilon(\omega)} < 1$ in an underdense plasma, Čerenkov radiation is not emitted by fast electrons in this case. In an overdense plasma, all light of frequency $\omega < \omega_p$ is absorbed as the refractive index $\sqrt{\epsilon(\omega)}$ is imaginary and therefore Čerenkov radiation cannot be emitted either. Moreover, a charged particle in uniform motion does not radiate if it moves in vacuum. However, transition radiation (TR) is emitted if a charged particle crosses the interface of two media. For instance, TR is emitted if an electron moves from an overdense plasma into vacuum. Besides, accelerated charges are well known to emit radiation [116].

Radiation processes such as coherent wake emission (CWE) [62, 82, 83], coherent synchrotron radiation (CSR) [64, 65] or coherent transition radiation (CTR) [66–77] may be the source of COR in our experiments. In fact, they are all triggered by fast electrons traversing the target rear side (and setting up an electric field). The COR in our case may be, thus, even a combination of those mechanisms. However, CWE, CSR and CTR can be distinguished by their polarization state [75]. Based on the polarization studies of this thesis, CWE provides the least probable explanation for the measured polarization of the COR. Hence, the following sections will focus on CSR and CTR. The interested reader can find a short description of CWE in appendix B. Throughout the rest of this chapter, the geometrical parameters and the orientation of the target as defined in Fig. 2.2 are used.

2.5.1. Synchrotron Radiation (SR)

When the hot electrons cross the target rear surface into vacuum, they set up an electrostatic sheath field, oriented normal to the rear surface, which acts back on themselves [66, 128] and accelerates the electrons to turn back to the target [64, 129]. An accelerated relativistic electron emits radiation inside a small cone which points in the direction of the momentary velocity vector \vec{v} of the fast electron, independent of the electron acceleration direction $\dot{\vec{v}}$.

Angular Characteristics In this paragraph, the charge is assumed to be accelerated only for a short time and hence the velocity $\vec{\beta} = \vec{v}/c$ and acceleration $\dot{\vec{\beta}}$ can be considered constant. Without loss of generality, we can therefore choose $\vec{\beta} \parallel z$ -axis. Furthermore, the radiation is assumed to be observed at large distances and therefore the observation direction \vec{n} can be considered to remain unchanged on timescales of the acceleration. Now, two examples are considered to illustrate the angular characteristics of the radiation emitted by an accelerated charge. For $\vec{v} \parallel \dot{\vec{v}}$, the radiated energy per solid angle is given as [116]

$$\frac{dP}{d\Omega} = \frac{e^2 \dot{v}^2}{16\pi^2 \epsilon_0 c^3} \frac{\sin^2 \theta}{(1 - \beta \cos \theta)^5}. \quad (2.15)$$

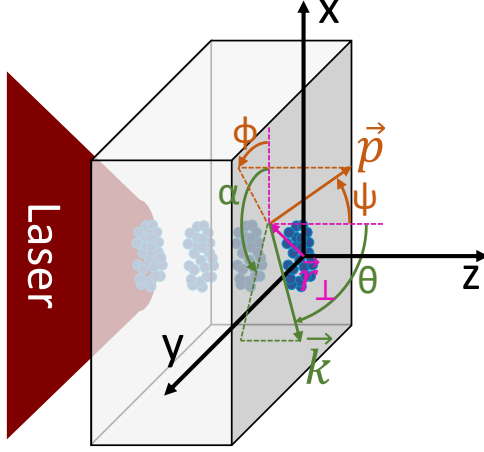


Figure 2.2.: A schematic drawing of the laser-solid interaction. The target (e.g. a thin aluminum foil) and its orientation is indicated as a gray plate. The laser accelerates bunches of electrons (blue circles) at the target front side (left) towards the target rear side (right). At the moment of arrival at the target rear side, every accelerated electron (at position \vec{r}_\perp in the xy -plane and with momentum \vec{p}) produces optical radiation. The total emitted radiation is a superposition of the radiation from the single electrons which follow a certain momentum and position distribution (more details in section 2.5.3). The radiation is measured in observation direction $\vec{n} = \vec{k}/|\vec{k}|$, with the wave vector \vec{k} .

This variation in radiated energy with observation direction is plotted as a radiation pattern in Fig. 2.3a. A radiation pattern shows the radiated energy per solid angle in a particular direction as the distance to the origin. Here, the maximum radiation intensity is given at an angle of $\theta_{\max} = \arccos \left[\left(\sqrt{1 + 15\beta^2} - 1 \right) / (3\beta) \right]$. For the orange curve in Fig. 2.3a, one gets $\theta_{\max}(\beta = 0.83) \approx 18.1^\circ$. In Fig. 2.3, $\beta = 0.83$ was chosen as an example because this is the velocity of an electron with energy $T_h = 400 \text{ keV}$ as calculated from Eq. 2.13 for typical experimental parameters ($I_L = 10^{19} \text{ W/cm}^2$). For $\vec{v} \perp \vec{\dot{v}}$, on the other hand, the radiation pattern in Fig. 2.3b has been calculated from [116]

$$\frac{dP}{d\Omega} = \frac{e^2 \dot{v}^2}{16\pi^2 \epsilon_0 c^3} \frac{1}{(1 - \beta \cos \theta)^3} \left[1 - \frac{\sin^2 \theta \cos^2 \alpha}{\gamma^2 (1 - \beta \cos \theta)^3} \right]. \quad (2.16)$$

The radiation pattern for $\vec{v} \perp \vec{\dot{v}}$ (Fig. 2.3b) is slightly different from the angular energy distribution in case of $\vec{v} \parallel \vec{\dot{v}}$ (Fig. 2.3a) but still exhibits the typical maximum in propagation direction. However, the total radiated power (integrated over all angles) is lower by a factor of γ^{-2} for the case of $\vec{v} \parallel \vec{\dot{v}}$ as compared to a situation where $\vec{v} \perp \vec{\dot{v}}$. In the latter case, the electron moves on a momentary circular orbit and the emitted radiation is called synchrotron radiation (SR) [116]. However, one should note that most publications about SR in laser-plasma interactions with overdense targets focus on SR which is emitted at the target front side towards the target rear side by electrons accelerated in the laser field. As the overdense target is transparent in the XUV regime, the high-frequency SR can propagate through the target [64, 65, 129–132].

Spectral Characteristics As derived in [116], the radiation energy per solid angle and frequency interval in observation direction $\vec{n} = \vec{k}/|\vec{k}|$, with the wavevector \vec{k} , by a charge with arbitrary velocity $\vec{\beta} = \vec{v}/c$ and acceleration $\vec{\dot{\beta}}$ is given by

$$\frac{d^2 W}{d\omega d\Omega} = \frac{e^2}{16\pi^3 \epsilon_0 c} |\vec{E}(\omega, \Omega)|^2 = \frac{e^2}{16\pi^3 \epsilon_0 c} \left| \int_{-\infty}^{\infty} \frac{\vec{n} \times [(\vec{n} - \vec{\beta}) \times \vec{\dot{\beta}}]}{(1 - \vec{\beta} \cdot \vec{n})^2} e^{i\omega[t - \vec{n} \cdot \vec{r}(t)/c]} dt \right|^2, \quad (2.17)$$

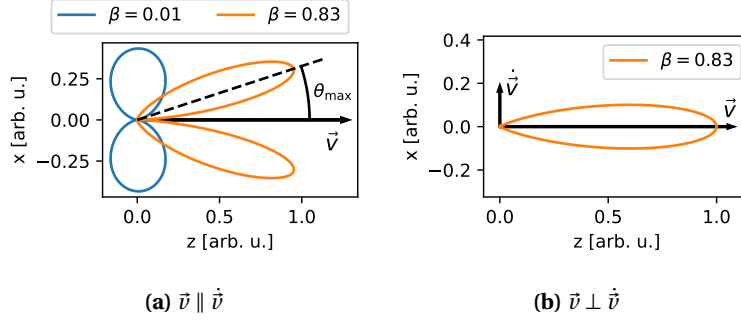


Figure 2.3.: (a) The radiation pattern for a charge (located at the origin of the coordinate system) which is accelerated in propagation direction ($\vec{v} \parallel \vec{v} \parallel z$ -axis), shown for a non-relativistic (blue line, $\beta = 0.01$, $\gamma = 1.00005$) and a relativistic particle (orange line, $\beta = 0.83$, $\gamma = 1.8$). The relativistic radiation pattern ($\beta = 0.83$) was scaled by a factor 10^{-2} whereas the acceleration is the same for the two shown radiation patterns. (b) The normalized radiation pattern for a charge (located at the origin of the coordinate system) which is accelerated perpendicular to its current velocity vector $\vec{v} \perp \vec{v}$.

and depends on the trajectory $\vec{r}(t)$ of the charged particle [133]. Here, $\vec{E}(\omega, \Omega)$ refers to the electric field of SR emitted per $d\omega$ and $d\Omega$. Again, the geometrical setup as defined in Fig. 2.2 is used. Due to the electric sheath field and magnetic fields induced by the return current at the target rear side, the hot electrons are accelerated back to the target on a curved trajectory in a phenomenon called "fountain effect" [134, 135]. Therefore, an accelerated charge which moves on a momentary circular orbit, emitting SR, is considered next as a special case of Eq. 2.17. Approximating the trigonometric functions for small angles and small times around $t = 0^1$ and choosing $\vec{v}(t = 0) \parallel z$ -axis, the radiated energy by an accelerated relativistic charge per solid angle and frequency interval becomes

$$\frac{d^2 W}{d\omega d\Omega} = \frac{e^2}{12\pi^3 \epsilon_0 c} \left(\frac{\omega \rho}{c} \right)^2 \left(\frac{1}{\gamma^2} + \theta^2 \right)^2 \left[K_{2/3}^2(\zeta) + \frac{\theta^2}{(1/\gamma^2) + \theta^2} K_{1/3}^2(\zeta) \right], \quad (2.18)$$

with the parameter $\zeta = \frac{\omega \rho}{3c} \left(\frac{1}{\gamma^2} + \theta^2 \right)^{3/2}$, the radius ρ of the momentary circular trajectory and the modified Bessel function of second kind $K_\alpha(x)$ of order α . The first term inside the square brackets in Eq. 2.18 contains the contribution of SR polarized in the plane of motion whereas the second term contains the SR polarized perpendicular to the plane of motion [116].

Depending on the strength of the electric sheath field (which may change during the interaction due to variations in the rear side electron density), the high energy tail in the fast electron energy distribution may escape the target rear side electric sheath field whereas the low energy fast electrons recirculate towards the target [136]. However, calculating an exemplary radiation spectrum for typical experimental parameters requires an assumption about the radius ρ of the hot electron trajectory at the target rear side. Thus, we assume that the ra-

¹This approximation is valid for relativistic particles where the SR is confined to a small cone around the momentary velocity vector. Thus, \vec{v} points only for a short amount of time in the observation direction and radiation is observed at small angles around \vec{v} .

dius of the momentary circular electron trajectory is comparable to the Debye length¹, hence $\rho \approx \lambda_{D, \text{rear}}$ [66]. Nevertheless, the hot electron current is carried by many electrons with an approximately relativistic Maxwellian velocity distribution [81]. Therefore, the hot electron radius ρ varies throughout the hot electron velocity distribution, as observed also in PIC simulations [64, 129]. However, for most hot electrons $\rho \approx \lambda_{D, \text{rear}}$ is a reasonable approximation. Based on a TNSA model [128], the Debye length at the target rear side is approximately given by

$$\lambda_{D, \text{rear}} \approx 1.37 \mu\text{m} \frac{r_0 + d \tan \Delta_\psi}{r_0} \frac{\sqrt{1 + 0.73 I_{18} \lambda_\mu^2} - 1}{I_{18}^{7/8}}, \quad (2.19)$$

with the focal spot radius r_0 of the laser, the target thickness d , the divergence half angle Δ_ψ of the hot electron current, the laser intensity I_{18} in units of 10^{18} W/cm^2 , and the laser wavelength λ_μ in units of μm . For typical experimental conditions ($I_L = 10^{19} \text{ W/cm}^2$, $\lambda_L = 1030 \text{ nm}$) and assuming no divergence ($\Delta_\psi = 0$), $\lambda_{D, \text{rear}} \approx 0.4 \mu\text{m}$ at the target rear surface. The hot electron temperature is estimated from Eq. 2.13 to be around 0.4 MeV. After integrating Eq. 2.18 over θ from $-\pi/2$ to $\pi/2$, the SR energy spectrum for a single electron of such a hot electron current is given as

$$\frac{dW}{d\omega} = \sqrt{3} \frac{e^2}{4\pi\epsilon_0 c} \gamma \omega / \omega_c \int_{\omega/\omega_c}^{\infty} K_{5/3}(x) dx, \quad (2.20)$$

with the critical frequency $\omega_c = 1.5\gamma^3 c / \rho$. Above ω_c , the SR spectral intensity falls rapidly to zero [116], as shown in Fig. 2.4a, whereas the SR remains rather flat in the spectral range investigated in the experiments of this thesis. Besides in [116], the derivation of Eq. 2.18 and Eq. 2.20, using a slightly different approach, can also be found in [138].

Polarization Characteristics The electric field component of SR oriented perpendicular to the plane of motion is a factor of seven lower than the electric field component which lies in the plane of motion. Hence, SR is mainly polarized in the plane of motion of the fast, relativistic electron [116]. Consequently, in case of SR, the polarization can vary across the region of emission of optical radiation, depending on the direction in which the electrons travel before they hit the target rear surface again.

2.5.2. Transition Radiation (TR)

First mentioned and theoretically described in 1946 by V. L. GINZBURG and I. M. FRANK [139], TR is emitted, when a charged particle crosses the interface between two media with different refractive indices [139, 140]. With respect to the electron propagation direction, TR is emitted into the front and back hemispheres (in the following called forward and backward direction) which are separated by the interface between the two media [140].

¹ It turns out that equating the relativistic centripetal force $\gamma m_e v^2 / \rho$ [137] and the force of the electric sheath field ($F_E(z) = 2k_B T_{\text{hot}} / [z + \sqrt{2}\lambda_{D, \text{rear}}]$, based on a TNSA model [128]) on an electron comes to a similar result for the approximation of the hot electron radius ρ .

To understand the origin of TR, one should consider the time- and space-dependent dielectric polarization $\vec{P}(\vec{x}, t)$ which is induced by the EM field of the moving charged particle and which results in the emission of EM radiation. The radiation from different positions in a medium only overlaps coherently near the interface inside a certain region [116] which is called the formation zone [141]. For normal incidence of the charged particle on the interface, the thickness of this formation zone is called formation length and given by

$$d(\omega) = \frac{c}{\omega} \frac{\beta}{|1 - \beta\sqrt{\epsilon(\omega)}\cos\theta|}, \quad (2.21)$$

with the dielectric constant $\epsilon(\omega)$ of the medium at the radiation (angular) frequency ω [141] which is given by $\epsilon = \eta^2 = 1 - \omega_p^2/\omega^2$ for a plasma. Because the existence of an interface requires two media, there are also two formation lengths, one for each medium.

Angular Characteristics For normal incidence and at relativistic particle velocities, qualitative arguments show that TR only adds up coherently if $\eta(\omega)\gamma\theta \lesssim 1$, where $\eta(\omega)$ is the refractive index of the material. Hence, TR is confined to a cone with $\theta \lesssim 1/\gamma$ around the velocity vector of the charged particle [116], as shown in Fig. 2.4b. The plotted angular TR distribution in Fig. 2.4b also illustrates that the emission cone of TR becomes narrower with increasing electron energy $W_{\text{kin}} = (\gamma - 1)m_e c^2$. For an electron at oblique incidence ($\psi \neq 0$) on the plasma-vacuum interface, the angular TR distribution becomes asymmetrical [142].

In case of a relativistic, charged particle ($\cos\theta \simeq 1$), the upper limit of the formation length is reached at $\omega = \gamma\omega_p$ and given by $D = d_{\text{max}} = \gamma c/\omega_p$ [116]. For aluminum ($\hbar\omega_p = 15.2 \text{ eV}$ [143]) and typical experimental parameters of this thesis ($I = 10^{19} \text{ W/cm}^2$, $\lambda = 1030 \text{ nm} \rightarrow \gamma = \frac{k_B T_{\text{hot}}}{mc^2} + 1 = 1.8$, T_{hot} from Eq. 2.13), the formation length in the optical (i.e. visible) regime becomes $d(515 \text{ nm}) \approx 13 \text{ nm}$ under the assumption of $\cos\theta \simeq 1$. Hence, the efficiency of TR emission is expected to decrease if the scale length of the plasma at the target rear side is longer than the formation length $d(\omega)$ [142]. In comparison, the formation length in vacuum is quite large (around $1.4 \mu\text{m}$ at 515 nm). The electric sheath field at the target rear side will hinder less energetic electrons to travel beyond the formation zone in vacuum. Consequently, only the high-energy tail in the hot electron momentum distribution is expected to contribute significantly to the emitted TR [144].

Spectral Characteristics The Maxwell equations for the particular problem of an electron traversing the interface between two media of different dielectric properties can be solved using Fourier integration, as shown by M. L. TER-MIKAELIAN [140], to calculate the TR emitted by a single charged particle. The discussion below follows the equations derived in [140], which are however often quite complex. For reasons of simplicity, we first consider an electron which traverses the interface from plasma into vacuum at normal incidence. The emitted TR energy in forward direction (i.e. into vacuum for the current geometry) per unit

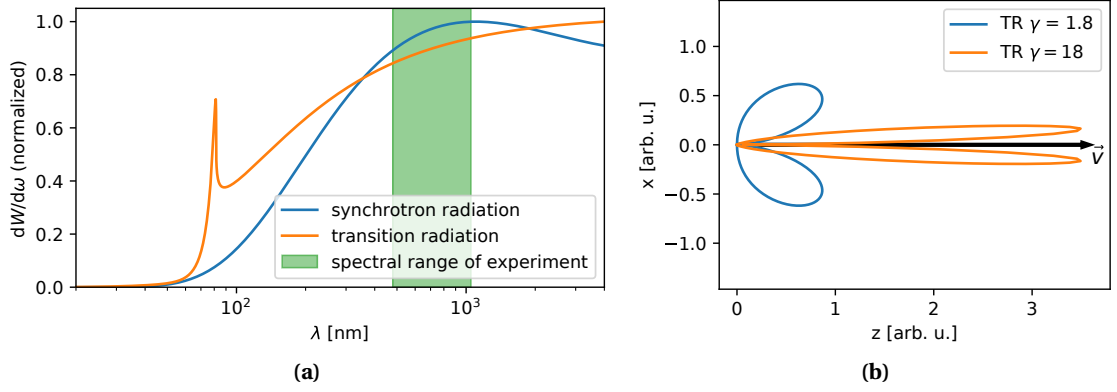


Figure 2.4.: (a) The spectral energy distribution of SR (blue line) and TR (orange line) emitted by a single electron. For both spectra, the typical experimental parameters of this thesis are used ($I = 10^{19} \text{ W/cm}^2$, $\lambda = 1030 \text{ nm}$), leading to $\rho \approx \lambda_D = 0.4 \mu\text{m}$ (Eq. 2.19) and $\gamma \approx 1.8$ (T_{hot} from Eq. 2.13). The SR spectrum is calculated from Eq. 2.20. The TR intensity is calculated for an electron traversing normal to the aluminum-vacuum interface ($\hbar\omega_p = 15.2 \text{ eV}$ [143]) into vacuum. The TR spectrum (orange line in Fig. 2.4a) is calculated by numerically integrating Eq. 2.22 over θ from $-\pi/2$ to $\pi/2$. To calculate the angular energy distribution of TR emitted by a single electron, Eq. 2.22 is numerically integrated over $\hbar\omega$ from $\approx 0 \text{ eV}$ to 62 eV . This angular distribution of TR, emitted by a charge located in the origin, is plotted in form of a radiation pattern for two different electron energies in (b). A radiation pattern shows the radiated energy per solid angle in a particular direction as the distance to the origin. The orange curve ($\gamma = 18$) was scaled by the factor 3×10^{-3} .

angular frequency and solid angle is given by

$$\frac{d^2 W^{\parallel}}{d\omega d\Omega} = \frac{e^2}{4\pi^3 \epsilon_0 c} \frac{\beta^2 \sin^2 \theta \cos^2 \theta}{(1 - \beta^2 \cos^2 \theta)^2} \left| \frac{(\epsilon - 1)(1 - \beta^2 - \beta \sqrt{\epsilon - \sin^2 \theta})}{(1 - \beta \sqrt{\epsilon - \sin^2 \theta})(\epsilon \cos \theta + \sqrt{\epsilon - \sin^2 \theta})} \right|^2, \quad (2.22)$$

where the superscript \parallel indicates that the radiation is polarized parallel to the radiation plane, which is the plane containing the momentum vector \vec{p} and the normal to the interface (here the z -axis; see Fig. 2.2) [140]. For aluminum ($\hbar\omega_p = 15.2 \text{ eV}$ [143]) and typical experimental parameters, the spectrum of TR emitted by a single electron traversing normal to the plasma-vacuum interface is plotted in Fig. 2.4a. The TR spectrum falls rapidly to zero for $\omega > \gamma\omega_p$, as it can be seen in Fig. 2.4a. In the spectral region which is considered in the experiment of this thesis ($\omega \ll \gamma\omega_p$), however, the spectrum of TR emitted by a single electron remains rather flat. In case of $\omega \ll \omega_p$ (as valid for aluminum or a highly overdense plasma), the dielectric constant of the plasma can be approximated by $\epsilon \rightarrow -\infty$ and Eq. 2.22 becomes

$$\frac{d^2 W^{\parallel}}{d\omega d\Omega} = \frac{e^2}{4\pi^3 \epsilon_0 c} \frac{\beta^2 \sin^2 \theta}{(1 - \beta^2 \cos^2 \theta)^2}. \quad (2.23)$$

Hence, for $\epsilon \rightarrow -\infty$, the emitted TR energy per unit angular frequency and solid angle does not depend on the frequency which results in a flat spectrum.

Polarization Characteristics The direction of polarization of TR depends on the propagation direction of the charged particle and the direction of observation. For a charged particle at normal incidence onto the plasma-vacuum interface, TR is radially polarized. Thus, the

polarization lies exclusively in the radiation plane formed by the wavevector \vec{k} (direction of observation) and the normal to the interface (here z -axis, see Fig. 2.2). At oblique particle incidence, there is an additional polarization perpendicular to the radiation plane¹ [140]. The general electric fields for the different polarization directions are given in the next section.

2.5.3. Coherent TR and Coherent SR from a Hot Electron Current

The existing treatments of CSR describe the coherent superposition of SR emitted by successive bunches of electrons in synchrotron light facilities [145, 146] or in astrophysics [147]. However, the approximations applied in [145, 147] are only valid for highly relativistic electrons ($\gamma \gg 1$) with a narrow emission cone, which does not apply to the experiments performed in this thesis. Thus, the general formula for CSR in laser-plasma interactions is discussed in the end of this section, without the simplifications that $\gamma \gg 1$ allows. Despite the differences, CSR and CTR at the target rear side are both composed of a train of attosecond bursts of radiation initiated by the periodically spaced bunches of fast electrons [70, 75, 148, 149]. As shown in Fig. 2.4a, the spectra of TR and SR are rather flat in the spectral region considered in this thesis with an intensity variation of maximum 12 % between 480 nm and 1050 nm. The spectral properties of the observed COR are therefore mostly due to the temporal structure of the fast electron current, whereas the type of radiation which gave rise to this COR plays only a minor role. Hence, the coherent superposition of optical radiation at the target rear side in laser-plasma experiments is discussed in the following using TR as an example.

The treatment of CTR in this section follows closely the work on CTR by C. BELLEI *et al.* [142, 144] who unified the theoretical descriptions by J. ZHENG *et al.* [150, 151] and C.B. SCHROEDER [152]. In comparison to the work by C. BELLEI *et al.* [142, 144], the model presented in the following keeps the flexibility to vary the temporal structure of the hot electron current to a certain extent. This allows to calculate the influence of variations in the hot electron acceleration at the target front side on the COR spectrum.

2.5.3.1. Coherent transition radiation (CTR)

Instead of a single electron as before, we now consider a beam of electrons which is accelerated at the target front side and propagates to the target rear side where it emits TR when crossing the plasma-vacuum interface (see Fig. 2.2). The intensity I of the emitted TR contains the sum of the electric fields \vec{E} of the TR induced by the individual electrons

$$I \propto \sum_{i=1}^N \sum_{j=1}^N \vec{E}_i \cdot \vec{E}_j^* = \underbrace{\sum_{i=1}^N |\vec{E}_i|^2}_{\text{ITR}} + \underbrace{\sum_{i,j=1; i \neq j}^N \vec{E}_i \cdot \vec{E}_j^*}_{\text{CTR}}, \quad (2.24)$$

¹If significant absorption is present, the TR will actually be elliptically polarized [140]. This is however neglected here.

where the superscript $*$ marks the complex conjugate and N is the number of electrons. In contrast to incoherent transition radiation (ITR), the CTR term is made up of the interference of the TR fields emitted by different electrons. Hence, CTR, scaling with $N(N-1)$, is usually orders of magnitude more intense than ITR which scales with N [142].

Next, the sums in Eq. 2.24 are replaced by integrals over the electron beam distribution $h(\vec{r}, \vec{u})$, with the normalized momentum $\vec{u} = [|\vec{p}|/m_e c](\sin \psi \cos \phi, \sin \psi \sin \phi, \cos \psi)^T$ and the position \vec{r} . The absolute normalized momentum is therefore $u = \gamma\beta$. The total emitted TR energy per unit angular frequency and solid angle then becomes

$$\frac{d^2 W}{d\omega d\Omega} = \frac{e^2 N}{4\pi^3 \epsilon_0 c} \left[\underbrace{\int d^3 \vec{u} g(\vec{u}) (E_{\parallel}^2 + E_{\perp}^2)}_{\text{ITR}} + (N-1) \underbrace{\left(\left| \int d^3 \vec{u} g(\vec{u}) E_{\parallel} F \right|^2 + \left| \int d^3 \vec{u} g(\vec{u}) E_{\perp} F \right|^2 \right)}_{\text{CTR}} \right], \quad (2.25)$$

where the variables \vec{E}_{\parallel} and \vec{E}_{\perp} refer to the Fourier-transformed electric fields of TR of a single particle with polarization parallel and perpendicular to the radiation plane. The radiation plane is spanned by the wave vector $\vec{k} = \omega/c(\sin \theta \cos \alpha, \sin \theta \sin \alpha, \cos \theta)$ and the target rear surface normal. For aluminum ($\hbar\omega_p = 15.2 \text{ eV}$ [143]), one can safely assume the target to be a perfect conductor ($|\epsilon| \rightarrow \infty$). Then, the expressions for the electric fields \vec{E}_{\parallel} and \vec{E}_{\perp} , as derived in [140], can be simplified to become

$$E_{\parallel}(\theta, \alpha, \phi, \psi, u) = \frac{u \cos \psi \left[u \sin \psi \cos(\phi - \alpha) - \sqrt{1 + u^2} \sin \theta \right]}{\left[\sqrt{1 + u^2} - u \sin \psi \cos(\phi - \alpha) \sin \theta \right]^2 - u^2 \cos^2 \psi \cos^2 \theta}, \quad (2.26)$$

$$E_{\perp}(\theta, \alpha, \phi, \psi, u) = \frac{u^2 \cos \psi \sin \psi \sin(\phi - \alpha) \cos \theta}{\left[\sqrt{1 + u^2} - u \sin \psi \cos(\phi - \alpha) \sin \theta \right]^2 - u^2 \cos^2 \psi \cos^2 \theta}. \quad (2.27)$$

Additionally, Eq. 2.25 contains the momentum distribution function $g(\vec{u}) = \int d^3 \vec{r} h(\vec{r}, \vec{u})$ and the coherence function F [144, 152].

For the calculation of the emitted TR energy per unit angular frequency and solid angle, knowledge of the coherence function F and the momentum distribution function $g(\vec{u})$ is needed. Both, F and $g(\vec{u})$, depend on the electron distribution function $h(\vec{r}_{\perp}, t, \vec{u})$. Based on the choice of C. BELLEI *et al.* [144] and H. POPESCU *et al.* [70], the accelerated fast electrons are modeled by a **train of bunches** with Gaussian **temporal** and **transverse spatial** distribution. In accordance with the approaches in [67, 70, 72], a **relativistic Maxwellian (Jüttner) momentum distribution** ([153] and references therein)

$$h(\vec{u}) = \exp\left(-\sqrt{1 + \vec{u}^2}/W_T\right) / \left[4\pi W_T K_2(W_T^{-1})\right] \propto \exp(-W_e/k_B T_h) \quad (2.28)$$

is assumed to model the hot electron momentum distribution. Here, the modified Bessel function of the second kind of order n is denoted by K_n , $W_T = \frac{k_B T_h}{m_e c^2}$ is the normalized thermal energy, and $W_e = \gamma_e m_e c^2$ refers to the relativistic energy of an electron. A Jüttner momentum distribution is a reasonable assumption due to randomness in the electron acceleration at

the target front surface [81] and in good agreement with experiments [110]. Consequently, the hot electron distribution function is given as

$$h(\vec{r}_\perp, t, \vec{u}) = C f(\phi, \psi) \exp\left(-\frac{\sqrt{1+\vec{u}^2}}{W_T}\right) \times \sum_{l=1}^{l=n_b} Q_l \exp\left(-\frac{\left(t - t_l - \frac{d_0}{\beta c \cos \psi}\right)^2}{2\sigma_t^2}\right) \exp\left(-\frac{|\vec{r}_\perp - \vec{v}_\perp(t - t_l)|^2}{2\sigma_r^2}\right). \quad (2.29)$$

Here, C is a normalization constant, $f(\phi, \psi)$ denotes the angular momentum distribution of the fast electron current, and n_b is the number of electron bunches. Q_l is the number of electrons (specified later) in the l^{th} bunch which is "created" at time t_l at the target front. Moreover, d_0 is the target thickness and \vec{v} refers to the electron velocity. The subscript \perp denotes that the corresponding variable is oriented perpendicular to the z -axis as defined in Fig. 2.2. The arrival time of an electron bunch at the target rear side is given by $t = t_l + \frac{d_0}{\beta c \cos \psi}$. Here, it is taken into account that electrons of different velocity arrive at different times at the target rear side. Due to the high energy of the hot electrons, their propagation through the target is assumed to be ballistic [70]. In accordance with [144], the arrival time t of an electron bunch at the target rear side is used as a variable to model the longitudinal hot electron distribution instead of defining the hot electron distribution $h(\vec{r}_\perp, t, \vec{u})$ as a function of the longitudinal spatial axis z (see Fig. 2.2).

As derived in [152], the normalized coherence function F contains a phase term from the single-electron TR theory and can be expressed in terms of the arrival time t of an electron at the interface and the transverse position \vec{r}_\perp perpendicular to the z -axis, thus

$$F = \frac{1}{g(\vec{u})} \int d^2\vec{r}_\perp e^{-i\vec{k}_\perp \cdot \vec{r}_\perp} \int_{-\infty}^{\infty} dt e^{i\omega t} h(\vec{r}_\perp, t, \vec{u}). \quad (2.30)$$

After inserting Eq. 2.29 in Eq. 2.30 and evaluating the integrals, the coherence function is written as

$$F = \frac{1}{g(\vec{u})} C f(\phi, \psi) (2\pi)^{3/2} \sqrt{\sigma_r^2 + \vec{v}_\perp^2 \sigma_t^2} |\sigma_t| |\sigma_r| \left(\sum_{l=1}^{l=n_b} Q_l \exp(i\omega t_l) \right) \exp\left(-\frac{\sqrt{1+\vec{u}^2}}{W_T}\right) \times \exp\left(-\frac{\omega^2 \sigma_t^2}{2}\right) \exp\left(-\frac{\sigma_r^2 \vec{k}_\perp^2}{2}\right) \exp\left(i \left[\omega \frac{d_0}{\beta c \cos \psi} - \vec{k}_\perp \cdot \vec{v}_\perp \left(\frac{d_0}{\beta c \cos \psi} + i\omega \sigma_t^2 \right) \right]\right). \quad (2.31)$$

Following [144], a collimated electron current directed along ψ_0 and ϕ_0 is assumed to simplify the equations and hence

$$f(\phi, \psi) = \delta(\phi - \phi_0) \delta(\psi - \psi_0), \quad \vec{v}_\perp = 0, \quad (2.32)$$

where $\delta(x)$ is the Dirac delta function. A collimated beam does not suffer from transverse dephasing but only from longitudinal dephasing. Hence, we set $\vec{v}_\perp = 0$. Longitudinal dephasing, also called velocity dispersion in this context, is the longitudinal (i.e. in propagation direction) expansion of an electron bunch during propagation for a non-monoenergetic

electron bunch due to the different velocities of the electrons in the bunch. This longitudinal dephasing is considered by the term $\exp\left(i\omega \frac{d_0}{\beta c \cos \psi}\right)$ in Eq. 2.31. For a collimated electron beam, the normalization constant is obtained from $\int dtd^2\vec{r}_\perp d^3\vec{u} h(\vec{r}_\perp, t, \vec{u}) = 1$ and given by

$$C = \left((2\pi)^{3/2} \sigma_r^2 |\sigma_t| \sin \psi_0 W_T K_2(W_T^{-1}) \sum_{l=1}^{l=n_b} Q_l \right)^{-1}, \quad (2.33)$$

where the modified Bessel function of the second kind of order n is denoted by K_n . For comparability to [144], the transformation from u to $\tau = \frac{d_0}{c \cos \psi_0} \cdot \frac{\sqrt{1-u^2}}{u}$ is applied in the following. After inserting Eq. 2.31, 2.32, and 2.33 into Eq. 2.25, the total emitted CTR energy per unit angular frequency and solid angle becomes

$$\begin{aligned} \left. \frac{d^2 W}{d\omega d\Omega} \right|_{\text{CTR}} &= \frac{e^2 N(N-1)}{4\pi^3 \epsilon_0 c [W_T K_2(W_T^{-1})]^2 \left(\sum_{l=1}^{l=n_b} Q_l \right)^2} \left| \sum_{l=1}^{l=n_b} Q_l \exp(i\omega t_l) \right|^2 \exp(-\omega^2 \sigma_t^2) \\ &\quad \times \exp(-\vec{k}_\perp^2 \sigma_r^2) (\tau_0)^8 \left[\left| \int_{\tau_0}^{\infty} d\tau I_1(\tau) \exp(i\omega \tau) \right|^2 + (\tau_0)^2 \left| \int_{\tau_0}^{\infty} d\tau I_2(\tau) \exp(i\omega \tau) \right|^2 \right], \end{aligned} \quad (2.34)$$

with $|\vec{k}_\perp| = \frac{\omega}{c} \sin \theta$, $\tau_0 = d_0 / c \cos \psi_0$ and the following quantities:

$$I_{1,2}(\tau) = A_{1,2} \frac{\tau}{(\tau^2 - \tau_0^2)^{5/2}} \exp\left(-\frac{\tau}{W_T \sqrt{\tau^2 - \tau_0^2}}\right), \quad (2.35)$$

$$A_1(\tau) = \frac{\cos \psi_0 [\tau_0 \sin \psi_0 \cos(\phi_0 - \alpha) - \tau \sin \theta]}{[\tau - \tau_0 \sin \psi_0 \cos(\phi_0 - \alpha) \sin \theta]^2 - \tau_0^2 \cos^2 \psi_0 \cos^2 \theta}, \quad (2.36)$$

$$A_2(\tau) = \frac{\cos \psi_0 \sin \psi_0 \sin(\phi_0 - \alpha) \cos \theta}{[\tau - \tau_0 \sin \psi_0 \cos(\phi_0 - \alpha) \sin \theta]^2 - \tau_0^2 \cos^2 \psi_0 \cos^2 \theta}. \quad (2.37)$$

Throughout this thesis, the integrals in Eq. 2.34 are evaluated numerically. This works sufficiently well because the integrands in Eq. 2.34 are non-negligible only close to τ_0 , as most hot electrons have a velocity close to c .

A CTR Model for an Imaging Setup For comparability, the consideration of CTR was, so far, closely related to the work of C. BELLEI *et al.* [144]. However, Eq. 2.34 gives the total emitted CTR energy per unit angular frequency and solid angle and therefore describes the CTR energy in the far-field. By contrast, the CTR emission spot on the rear surface of thin Al foils was imaged (see experimental setup in Fig. 3.1) in the experiments presented in this thesis. In an imaging setup, the CTR emission in different directions from one point \vec{r}_\perp in the object plane (i.e. on the target rear surface) is imaged onto one point in the image plane [10] where the camera chip is placed. Therefore, the spatial averaging in Eq. 2.30 is omitted to get an adequate description of CTR for this thesis and Eq. 2.30 is replaced by

$$F_{\vec{r}_\perp} = \frac{1}{g(\vec{u})} e^{-i\vec{k}_\perp \cdot \vec{r}_\perp} \int_{-\infty}^{\infty} dt e^{i\omega t} h(\vec{r}_\perp, t, \vec{u}), \quad (2.38)$$

where the spatial phase factor from the single electron theory is preserved [152]. Analogous to before, Eq. 2.29 is inserted in Eq. 2.38 and the integrals are evaluated. The new coherence function is then given by

$$F_{\vec{r}_\perp} = \frac{1}{g(\vec{u})} C f(\phi, \psi) \frac{(2\pi)^{1/2} |\sigma_t| |\sigma_r|}{\sqrt{\sigma_r^2 + \vec{v}_\perp^2 \sigma_t^2}} \left(\sum_{l=1}^{l=n_b} Q_l \exp(i\omega t_l) \right) \exp\left(-\frac{\sqrt{1+\vec{u}^2}}{W_T}\right) \exp\left(-\frac{\omega^2 \sigma_t^2}{2}\right) \times \exp\left(i \left[\omega \frac{d_0}{\beta c \cos \psi} - \vec{k}_\perp \cdot \vec{r}_\perp \right]\right) \exp\left(-\frac{\left| \vec{r}_\perp - \vec{v}_\perp \left[\frac{d_0}{\beta c \cos \psi} + i\omega \sigma_t^2 \right] \right|^2}{2 [\sigma_t^2 \vec{v}_\perp^2 + \sigma_r^2]}\right). \quad (2.39)$$

For a collimated electron beam (see Eq. 2.32), the normalization constant is obtained from evaluating $\int d\tau d^3 \vec{u} h(t, \vec{u}) = 1$ (i.e. neglecting any terms depending on \vec{r}_\perp) and given as

$$C_{\vec{r}_\perp} = \left((2\pi)^{1/2} |\sigma_t| \sin \psi_0 W_T K_2(W_T^{-1}) \sum_{l=1}^{l=n_b} Q_l \right)^{-1}. \quad (2.40)$$

Now, Eq. 2.32, Eq. 2.39, and Eq. 2.40 are inserted into Eq. 2.25 which gives the total emitted CTR energy per unit angular frequency, solid angle and area (on the target rear surface)

$$\left. \frac{d^2 W}{d\omega d\Omega dx dy} \right|_{\text{CTR}} = \frac{e^2 N(N-1)}{4\pi^3 \epsilon_0 c [W_T K_2(W_T^{-1})]^2 \left(\sum_{l=1}^{l=n_b} Q_l \right)^2} \left| \sum_{l=1}^{l=n_b} Q_l \exp(i\omega t_l) \right|^2 \exp(-\omega^2 \sigma_t^2) \times \exp\left(-\frac{\vec{r}_\perp^2}{\sigma_r^2}\right) (\tau_0)^8 \left[\left| \int_{\tau_0}^{\infty} d\tau I_1(\tau) e^{i\omega \tau} \right|^2 + (\tau_0)^2 \left| \int_{\tau_0}^{\infty} d\tau I_2(\tau) e^{i\omega \tau} \right|^2 \right], \quad (2.41)$$

with $I_{1,2}(\tau)$ as introduced in Eq. 2.35.

Qualitative Discussion of Spectral CTR Characteristics For the sake of a better qualitative understanding of Eq. 2.34 and Eq. 2.41, the general properties of the CTR spectrum are discussed next. Coherence is reduced with increasing longitudinal dephasing and temporal duration σ_t . The longitudinal dephasing of an electron bunch is stronger for thicker targets because the longitudinal bunch expansion, due to electrons propagating at different velocities, increases with propagation. Longitudinal dephasing, and hence a coherence reduction, is less pronounced at higher hot electron temperatures as relatively more electrons move at $v \approx c$. Moreover, the coherence loss due to longitudinal dephasing increases with decreasing wavelength. This is reflected in the integrals in Eq. 2.34, Eq. 2.41, and the term $\exp(-\omega^2 \sigma_t^2)$ which both cause a spectral decay of the CTR energy with decreasing wavelength. For short pulses, it is more realistic to assume a non-constant number of electrons Q_l per bunch. Having, for example, Q_l following the Gaussian envelope of the electric field of the laser pulse results in a reduced intensity of the subpeaks between the harmonics and to an increased spectral width of the harmonics as compared to a constant Q_l . Hence, Eq. 2.34 and Eq. 2.41 provide the flexibility to calculate the CTR spectrum for an arbitrary distribution of Gaussian electron bunches of varying charge. Nevertheless, it is more instructive to consider the two most relevant cases to laser-plasma physics as discussed by C. BELLEI *et al.* [144] and H.

POPESCU *et al.* [70].

In the simple case of an odd number of electron bunches n_b with a constant time delay $\Delta t = t_l - t_{l-1}$ between two successive bunches and $Q_l = 1$, the substitution

$$\left| \sum_{l=1}^{l=n_b} Q_l \exp(i\omega t_l) \right|^2 \rightarrow \frac{\sin^2(n_b \omega \Delta t / 2)}{\sin^2(\omega \Delta t / 2)} \quad (2.42)$$

can be applied. The consequent CTR spectrum shows peaks at multiples of the acceleration frequency at the target front side, hence at $\omega = m2\pi/\Delta t$ with $m = 0, 1, 2, \dots$ (see Fig. C.1). The width of those harmonics scales inversely with the number of electron bunches n_b [144]. Between two harmonics, there are $n_b - 2$ subpeaks of much lower amplitude.

A more realistic model, called "Popescu model" in the following, considers n_b electron bunches accelerated at ω_L and $2n_b$ electron bunches accelerated at $2\omega_L$. In that way, the presence of different plasma heating mechanisms at the target front side is taken into account [70]. A schematic cross section of the laser-solid interaction to which the Popescu model corresponds is given in Fig. 2.5. For the Popescu model, the substitution

$$\left| \sum_{l=1}^{l=n_b} Q_l \exp(i\omega t_l) \right|^2 \rightarrow \frac{\sin^2\left(n_b \frac{\pi\omega}{\omega_L}\right)}{\sin^2\left(\frac{\pi\omega}{\omega_L}\right)} \left[P_1^2 + 4P_2^2 \cos^2\left(\frac{\pi\omega}{2\omega_L}\right) + 4P_1 P_2 \cos\left(\frac{\pi\omega}{2\omega_L}\right) \cos\left(\frac{\pi\omega}{2\omega_L} + a\omega\right) \right] \quad (2.43)$$

can be applied. Here, P_1 (P_2) refers to the relative amount of electrons per bunch accelerated at ω_L ($2\omega_L$) and a is the relative temporal delay between the two electron populations as indicated in Fig. 2.5. Now, the relative intensity of the harmonics in the spectrum of CTR with respect to each other depends on the ratio P_1/P_2 and a [70], which is discussed in more detail in chapter 4. A typical example of a CTR spectrum and the underlying temporal hot electron distribution in high-intensity laser-plasma interactions is plotted in Fig. 2.6. In comparison to the upper subplot in Fig. 2.6, the peaks in the number of electrons at the target rear side, referring to the electron bunches, are smeared out due to longitudinal dephasing. The CTR spectrum in the lower subplot in Fig. 2.6 shows the typical peaks at harmonics of the laser frequency with $n_b - 2$ subpeaks between neighboring harmonics.

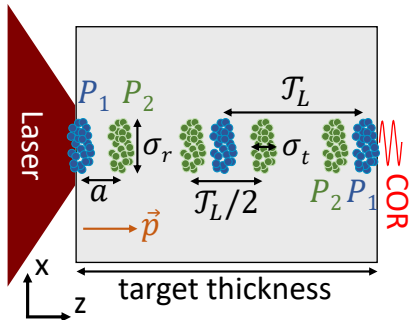


Figure 2.5.: A schematic cross section of the laser-solid interaction with the parameters of the CTR model inspired by [70]. The target (e.g. a thin Al foil) is indicated as a gray box. The sketched situation ($\mathcal{T}_L \approx 3.44\text{fs}$) corresponds to a target which is approximately $2\mu\text{m}$ thick. The laser accelerates bunches of electrons (blue and green circles) at the target front side (left) towards the target rear side (right) where they emit radiation.

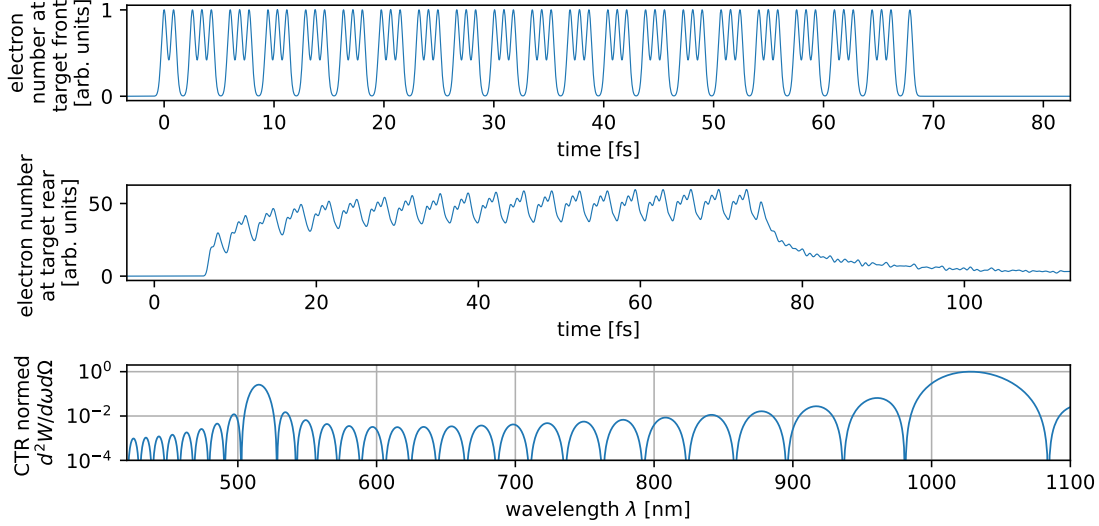


Figure 2.6.: Plots based on the presented CTR model, which depict the temporal hot electron distribution at the target front and rear side together with the corresponding CTR spectrum for an exemplary hot electron distribution. The hot electron distribution at the target front side (upper subplot) as a function of time is acquired from $h(\vec{r}_\perp, t, \vec{u})$ by neglecting all terms depending on \vec{r}_\perp and \vec{u} and setting $d_0 = 0$. The hot electron distribution at the target rear side (middle subplot) is calculated by numerically evaluating the integral $\int d^3\vec{u} h(\vec{r}_\perp, t, \vec{u})$. The normalized differential CTR energy (lower subplot) is calculated from Eq. 2.41 with the substitution from Eq. 2.43 for typical experimental parameters of this thesis, namely $T_h = 0.4$ MeV, $d_0 = 2 \mu\text{m}$ and $\sigma_t = \mathcal{T}_L / (10 \cdot \sqrt{2}) = 0.243$ fs (as proposed in [70] based on PIC results and fits to experimental data). Moreover, $P_1 = 1$, $P_2 = 1$, $a = 0.25\mathcal{T}_L$ and a combination of 20 bunches spaced at \mathcal{T}_L and 40 bunches spaced at $\mathcal{T}_L/2$ which emit CTR was chosen. For simplification, only one spatial dimension is considered by setting $\vec{r}_\perp = 0$. Analogous to the geometry in the experiments of this thesis, the CTR is calculated for $\theta = 37^\circ$ and $\alpha = 90^\circ$ (see Fig. 2.2). Moreover, it is assumed that the electrons propagate normal to the target rear side ($\phi = 90^\circ$, $\psi = 0^\circ$) with no divergence (see Eq. 2.32).

2.5.3.2. Coherent synchrotron radiation (CSR)

The transition from the single-particle theory of SR to the superposition of SR emitted by an ensemble of particles follows in general the same approach as for TR. As discussed by J. D. JACKSON [116], the first step towards SR emitted by an ensemble of electrons would be to substitute the velocity and acceleration in Eq. 2.17 by a sum over all the electrons in the ensemble, thus

$$\frac{\vec{n} \times [(\vec{n} - \vec{\beta}) \times \dot{\vec{\beta}}]}{(1 - \vec{\beta} \cdot \vec{n})^2} e^{i\omega[t - \vec{n} \cdot \vec{r}(t)/c]} \rightarrow \sum_{j=1}^N \frac{\vec{n} \times [(\vec{n} - \vec{\beta}_j) \times \dot{\vec{\beta}}_j]}{(1 - \vec{\beta}_j \cdot \vec{n})^2} e^{i\omega[t - \vec{n} \cdot \vec{r}_j(t)/c]}. \quad (2.44)$$

In the limit of a continuous electron distribution, this sum may be replaced by an ensemble average over the normalized fast electron distribution $h(\vec{r}, t, \vec{u})$, as suggested in [116, 147, 152]. The emitted CSR energy per unit of angular frequency and solid angle then becomes

$$\frac{d^2W}{d\omega d\Omega} = \frac{e^2 N^2}{16\pi^3 \epsilon_0 c} \left| \int d^3\vec{u} \int d^3\vec{r} \int_{-\infty}^{\infty} dt h(\vec{r}, t, \vec{u}) \frac{\vec{n} \times [(\vec{n} - \vec{\beta}) \times \dot{\vec{\beta}}]}{(1 - \vec{\beta} \cdot \vec{n})^2} e^{i\omega[t - \vec{n} \cdot \vec{r}/c]} \right|^2. \quad (2.45)$$

In contrast to TR, one cannot consider a single point of emission for an electron but rather

needs to integrate over the curved particle trajectory which complicates the evaluation of Eq. 2.45. Moreover, the hot electron beam quite likely evolves into a fountain-like shape [134, 135] if the electrons recirculate towards the target at the target rear side. Thus, most of the integrals in Eq. 2.45 would need to be evaluated numerically which requires extensive computational resources and considerations beyond the scope of this work. Hence, most of the discussion of the experimental results in chapter 4 rather relies on a qualitative discussion of CSR. Due to the similarity of CSR and CTR, it can be safely expected that the influences of the hot electron distribution $h(\vec{r}, t, \vec{u})$ on the CTR spectrum hold also approximately true for CSR. However, in section D.1 a very simplified version of Eq. 2.45 is introduced and numerically evaluated for a diverging electron beam to understand the polarization characteristics of the measured COR.

3. Methods

This chapter gives an overview over the methods used to investigate, measure, and analyze the optical radiation emitted from the rear side of thin foils which were irradiated by high-intensity laser pulses. First, the setup used for the experiments of this thesis is shown. Next, the single components of the experimental arrangement and their limitations are described in more detail, namely the laser, the plasma mirror, the target and the polarization resolved imaging of the rear side optical radiation. All the data analysis and calculations have been performed using the programming language python [154–157]. However, the raw png-images have been converted to txt-files, for better handling in python, using the graphical system engineering software LabView 2014 [158].

3.1. Experimental Setup

The experiments of this thesis, were conducted at the POLARIS laser system [159, 160], operated at the Helmholtz Institute in Jena. The experimental setup is depicted in Fig. 3.1. After the POLARIS laser pulses entered the target vacuum chamber, they were focused with a 6° off-axis parabola ($f = 90$ cm focal length, f-number $F \approx f/6$, silver coating) onto a plasma mirror (PM). The reflected laser pulses from the PM were recollimated by an identical off-axis parabola. Finally, the laser pulses were focused by a 19° off-axis parabola ($f = 30$ cm focal length, f-number $F \approx f/2$, silver coating) onto the thin Al target foils where intensities up to 3×10^{19} W/cm² are reached. The target rear side optical radiation was collected at an angle of $\theta = 37^\circ$ by an Mitutoyo apochromatic near-infrared (NIR) microscope objective with a tenfold magnification¹. The radiation collected by the microscope objective was brought to an elevated beam line via a periscope to direct the radiation out of the vacuum chamber through a window. The intensity of the rear side optical radiation varies strongly with the laser intensity (chapter 4). To prevent saturation of the rear side radiation diagnostics, three different neutral density (ND) absorption filter were mounted on a motorized stage (labeled c_{tot} in Fig. 3.1) which was located behind the exit window of the vacuum chamber. A wedged fused silica (also called quartz glass) plate was placed behind the ND filter stage (c_{tot}) to couple part of the radiation out to an imaging spectrometer. Behind the fused silica wedge, a second periscope was used to lower the beam path height to the diagnostics level. An achromatic lens ($f = 40$ cm) was positioned after the second periscope to image the radiation onto three cameras. To do so, three fused silica plates were used to couple part of the beam out

¹The microscope objective is designed for a working distance of 30.5 mm and a wavelength range from 480 nm to 1800 nm. The numerical aperture is 0.26. More details can be found at [161].

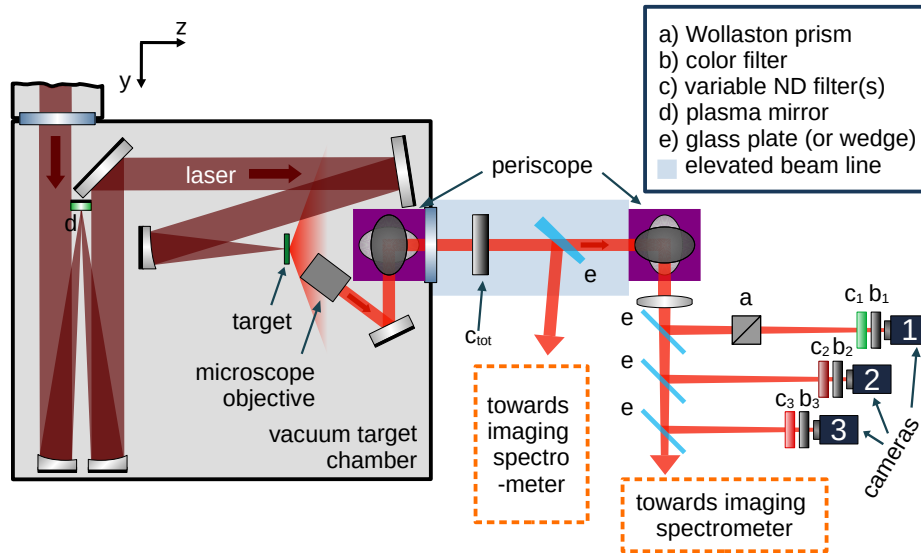


Figure 3.1.: Schematic drawing of the experimental setup used for the laser-solid interaction experiments presented in this thesis. The drawing is not to scale. If not specified differently, the following color filters are used: b_1 = bandpass filter at (520 ± 20) nm, b_2 = 1000 nm longpass filter, and b_3 = 900 nm longpass + 1000 nm shortpass filter. The ND absorption filters (c_1 , c_2 , c_3 , and c_{tot}) are adjusted to the COR intensity during the experiment but always considered in the data evaluation.

onto the cameras. In front of the three cameras, there were different ND filters and spectral filters as specified in the subheading of Fig. 3.1. Additionally, a Wollaston prism was placed in front of Camera 1 which allows to separate the light incident on Camera 1 into radiation polarized parallel and perpendicular to the optical axes of the Wollaston prism. In the following sections, the single components of the experimental setup in Fig. 3.1 are considered in more detail.

Comment on the Imaging Spectrometers For the sake of completeness, the imaging spectrometers are mentioned in the experimental setup (Fig. 3.1). However, the data from the two imaging spectrometers are not analyzed in this thesis. After a few experiments and an extensive literature research, it became clear that the COR needs to be measured over a broad wavelength range. Moreover, the phase information is lost during the spectral intensity measurement and phase retrieval algorithms must be employed to investigate the temporal structure of COR [162–166]. All this was, however, not feasible with the experimental possibilities at hand in this thesis.

3.2. Laser, Plasma Mirror and Target

POLARIS is a completely diode-pumped CPA laser system (see section A.3). After amplification and compression (see Fig. A.1), the POLARIS laser provides, on average, 170 fs short laser pulses at a central wavelength of $\lambda_L = 1030$ nm which contain up to 3.5 J of energy on the target at a repetition rate of 0.02 Hz on a daily basis. However, pulse duration and energy vary for successive laser pulses due to fluctuations in the POLARIS laser system. The

next paragraph describes briefly how these laser parameters were measured during an experiment. In that way, the laser intensity on the target surface could be calculated for every laser shot.

Laser Parameter Diagnostics during Experiment Knowledge about the laser intensity in the focal spot, where the target was placed, is of great importance for the interpretation of high-intensity laser-matter interactions. As indicated by Eq. A.2, a calculation of the laser intensity in the focal spot requires a measurement of the laser pulse energy, the pulse duration of the laser pulses and the focal spot area \mathcal{A} .

The pulse energy was measured using a calibrated pyroelectric energy measurement device which absorbs the laser pulse and calculates the laser pulse energy from current which is generated by the temperature increase of the sensor head. The laser pulse duration was estimated via second-order single-shot intensity autocorrelation (more details can be found in section A.1 of [167]). Because the autocorrelation (AC) trace does not contain the full information about the amplitude and phase of the electric field of the laser pulse, a pulse shape has to be assumed to calculate the pulse duration from the AC measurement [10]. Assuming a Gaussian laser pulse shape (see Eq. A.5), the FWHM pulse duration $\tau_{\text{FWHM,AC}}$ can be calculated from the AC signal. Additionally, a Gaussian distribution

$$I_{\text{Gauss}}(t) = I_0 \exp\left(-4 \ln 2 \left(t/\tau_{\text{FWHM,Gauss}}\right)^2\right) \quad (3.1)$$

was fitted to the AC to determine $\tau_{\text{FWHM,Gauss}}$. Using only $\tau_{\text{FWHM,AC}}$ would, however, overestimate the calculated laser peak intensity because a real laser pulse deviates from a perfect Gaussian shape and the energy in the side-wings of the AC would be neglected, as it can be seen in Fig. 3.2. To approximately consider the peak intensity reduction due to energy in the side-wings of the AC, it has been chosen to approximate the pulse duration as $\tau_{\text{FWHM}} = (\tau_{\text{FWHM,AC}} + \tau_{\text{FWHM,Gauss}})/2$. A more accurate measurement of τ_{FWHM} would require techniques which utilize optical correlation methods like, e.g., Frequency-Resolved Optical Gating (FROG) or Spectral Phase Interferometry for Direct Electric Field Reconstruction (SPIDER) [10]. An exemplary AC measurement of an POLARIS laser pulse together with a fitted Gaussian pulse can be seen in Fig. 3.2. Both, pulse duration τ_{FWHM} and pulse energy W_L can be measured online during an experiment for every laser pulse (also called laser shot). To do so, the (low-energy) leakage light of a highly reflective mirror was used. The pulse duration τ_{FWHM} was measured behind the compressor (see Fig. A.1) whereas W_L was measured before pulse compression. The focal spot area $\mathcal{A}_{\text{FWHM}}$, however, had to be measured at low intensity to prevent the damaging of the diagnostics.

The focal spot area was measured by imaging the focal plane in the target chamber onto a CCD-camera using a microscope objective (focal length $f = 10\text{ mm}$) placed behind the focus position and a lens (focal length $f = 50\text{ cm}$) positioned outside of the vacuum chamber (Fig. 3.2 in [103] shows the geometrical setup of the focal spot imaging). The exposure time of the camera is $250\text{ }\mu\text{s}$ and therefore exceeds the laser pulse duration by orders of magnitude. Hence, a non-calibrated, time integrated intensity distribution $I_{\text{meas}}(x, y)$ (i.e. the energy

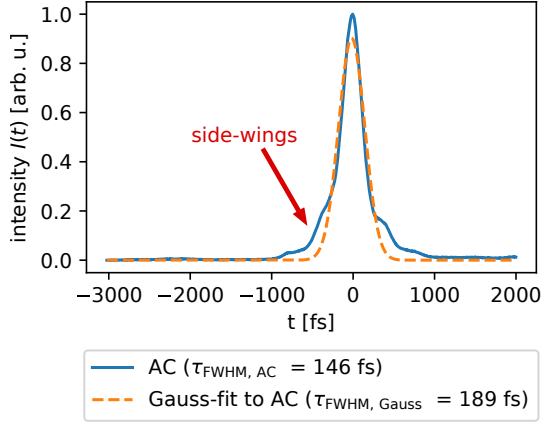


Figure 3.2.: Exemplary autocorrelation (AC) measurement of one POLARIS laser pulse. Shown is the AC intensity as a function of time. Assuming an Gaussian pulse shape, the pulse width has been calculated and denoted in the legend for the AC. Additionally, a Gaussian distribution (Eq. 3.1) has been fitted to the AC.

fluence) was acquired after taking the magnification into account. $I_{\text{meas}}(x, y)$ has then been used to calculate the area $\mathcal{A}_{\text{FWHM}}$ and the quality factor q_{FWHM} with respect to the Full Width at Half Maximum (FWHM):

$$\mathcal{A}_{\text{FWHM}} = \iint_{I_{\text{meas}}(x, y) > \frac{1}{2} \max(I_{\text{meas}}(x, y))} dx dy \quad (3.2)$$

$$q_{\text{FWHM}} = \frac{\iint_{I_{\text{meas}}(x, y) > \frac{1}{2} \max(I_{\text{meas}}(x, y))} I_{\text{meas}}(x, y) dx dy}{\iint_{\mathbb{R}^2} I_{\text{meas}}(x, y) dx dy}. \quad (3.3)$$

For the discretized camera images, these integrals transform into finite sums. The quality factor q_{FWHM} corresponds to the percentage of laser energy contained in $\mathcal{A}_{\text{FWHM}}$. In case of an ideal Gaussian intensity distribution in the focus (Eq. A.3 for $z = 0$), the quality factor becomes $q_{\text{FWHM, Gauss}} = 0.5$.

Assuming a Gaussian intensity distribution in space and time, the peak intensity I_0 can be calculated from the measured pulse properties

$$I_0 = \sqrt{\frac{\ln 16 \ln 256}{\pi} \frac{W_L}{8 \mathcal{A}_{\text{FWHM}} \tau_{\text{FWHM}}}} \approx 0.65 \frac{W_L}{\mathcal{A}_{\text{FWHM}} \tau_{\text{FWHM}}}, \quad (3.4)$$

with the natural logarithm \ln . Because the real laser focal spot deviates from a perfect Gaussian shape, the ratio of the measured quality factor $q_{\text{FWHM, meas}}$ (usually between 0.12 and 0.15) to $q_{\text{FWHM, Gauss}}$ needs to be considered in the calculation of the laser intensity on the target. Moreover, the laser energy on target is additionally reduced by the compressor transmittance (60 %) and the reflectivity of the PM (70 %). Hence, the peak intensity on target is

$$I_{0, \text{ on target}} \approx 0.65 \frac{q_{\text{FWHM, meas}}}{q_{\text{FWHM, Gauss}}} \frac{W_L \cdot 0.6 \cdot 0.7}{\tau_{\text{FWHM}} \mathcal{A}_{\text{FWHM}}}, \quad (3.5)$$

which was varied during an experiment by changing the laser pulse energy W_L .

Plasma Mirror (PM) The PM is made of a substrate with an anti-reflective coating designed for the laser wavelength. Hence, the PM has a very low reflectivity ($R < 0.1\%$) until a certain threshold laser intensity on the PM is reached. Then, the PM is ionized and becomes reflective. In that way, the PM lowers the intensity of the rising edge of the laser pulse to

reduce early ionization and expansion of the target before the arrival of the main laser pulse [168].

Target Positioning The accuracy of the calculated intensity in Eq. 3.5 depends not only on the precision of the measured quantities W_L , \mathcal{A}_{FWHM} , and τ_{FWHM} , but also on the precise positioning of the target in the laser focus. Hence, the Al foils used as targets were placed on a target holder which is mounted on a motorized stage with three degrees of freedom (xyz-translation) for precise positioning. As described on page 45 in [103] in more detail, the target rear surface was illuminated with a cw-laser and imaged with the focus (microscope) objective to place the Al foils at the laser focal position with a precision of $\Delta z \approx 10 \mu\text{m}$. However, the Rayleigh length of the laser ($z_R \approx 11.7 \mu\text{m}$) is comparable to Δz . Therefore, the calculated $I_{0, \text{on target}}$ provides an upper limit for the peak intensity on target. The actual peak intensity on target might be reduced by up to 42 % if the target was placed out of focus by $10 \mu\text{m}$.

3.3. Rear-Side Optical Radiation Diagnostics

3.3.1. Imaging

In chapter 2, it is explained how electrons are accelerated at the target front side towards the target rear where they give rise to COR. As sketched in Fig. 3.1, the COR emission spot on the target rear surface was imaged onto three CCD-cameras using an apochromatic microscope objective in combination with an achromatic focusing lens outside of the target chamber. Due to the design of the microscope objective, the object (i.e. the COR from the target rear side) needs to be placed at the focal position of the microscope objective to correct for aberrations. The magnified image of the object is thus at infinite distance and therefore a second lens, which is also called tube lens, was placed behind the microscope objective to produce an image of the object in its focal plane where also the camera chip was located [10]. The microscope objective collected radiation at an angle of $\theta = 37^\circ$ and $\alpha = 90^\circ$ with respect to the coordinate system defined in Fig. 2.2. In that way, we were close to imaging at $\theta = 0^\circ$ without risking that laser light which tunnels through the target is collected by the rear side radiation diagnostics [169].

3.3.1.1. Calibration and Systematic Errors

To calibrate the imaging setup, a positive 1951 USAF test target [170] was placed at the position of the target and illuminated with a green alignment laser incident at 37° to the test target front surface normal. The corresponding calibration images¹ for camera 1 can be seen in Fig. 3.3a and Fig. 3.3b. The size of the bars seen in Fig. 3.3 is provided by the manufacturer of the test target and can be compared to the size in pixel of the image of those bars on the

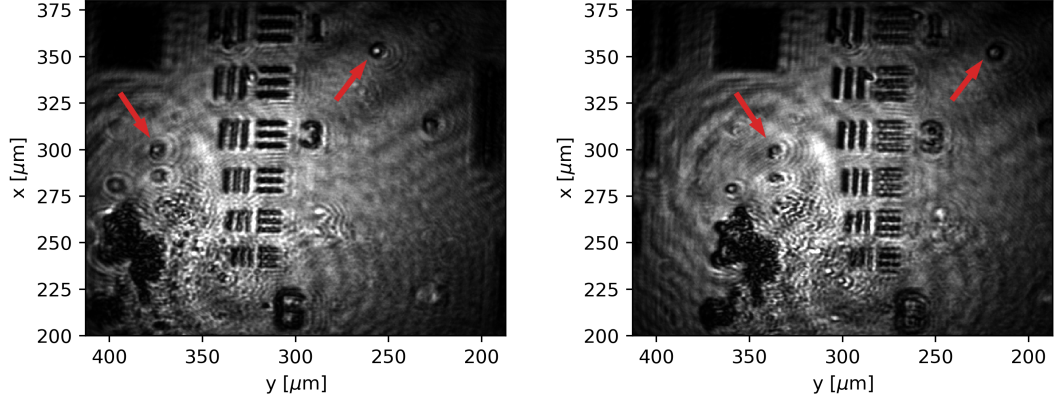
¹ Calibration images were also acquired with camera 2 and 3. However, there is no significant difference between the calibration images of the different cameras. Hence, only the calibration images of camera 1 are shown as an example in Fig. 3.3a and Fig. 3.3b.

camera. In that way, the imaging has been calibrated by rescaling the image axes from pixel to micrometer. The rescaling factors acquired from the calibration images (Fig. 3.3a and Fig. 3.3b) have been used throughout this thesis for the presented data.

Looking at Fig. 3.3a and 3.3b, the systematic errors of the imaging setup become clear. First of all, only a limited region of around $20\mu\text{m}$ in y -direction was in focus. Hence, parts of the imaged rear surface COR emission spot, as presented in section 4.1, were not in focus. This is aggravated by the fact that the pointing of the POLARIS laser was not stable and therefore the position of the focal spot changed for consecutive shots by several micrometers. This translates into a fluctuating position of the imaged COR emission spot. As suggested by J. HEIN [171], one can prevent the limited sharp region in y -direction by rearranging the experimental setup (see Fig. 3.1) to fulfill the Scheimpflug condition¹ [172]. By rotating the camera to fulfill the Scheimpflug condition, a sharp image of the target rear side could be acquired also for imaging at oblique angle. This could be particularly interesting for future experiments.

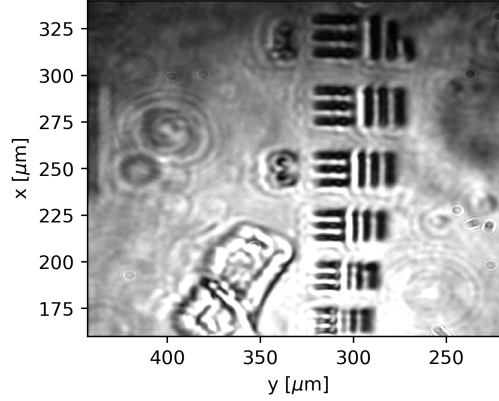
Moreover, the dust particles on the test target, marked by red arrows in Fig. 3.3a and 3.3b, show an asymmetric diffraction pattern. Such asymmetric diffraction patterns look like the imaging error coma. Whereas the microscope objective is corrected for coma, the lens in front of the cameras in Fig. 3.1 is only corrected for chromatic aberrations but not for coma. Coma is a monochromatic aberration which results in asymmetric images of point sources if the incident light rays are not parallel to the symmetry axis (i.e. its optical axis in this case) of the lens. This is illustrated in Fig. 3.4. Because the outer light rays (B) experience a different magnification than central rays (A), the off-axis light rays from the object are not imaged onto a single point (A') but rather form circles which are shifted with respect to each other. The larger the distance of the light rays to the center of the lens, the larger is the circle (and its distance d to the smallest circle) which those rays form on the image screen. The resulting image of a point object on the screen looks like a comet and hence the name coma [117]. Moreover, the direction of the asymmetry introduced by coma is the same even if the object is out of focus of the microscope objective. This can be understood from the analogy of shifting the screen in Fig. 3.4 along the optical axis. Hence, misalignment in the imaging setup (Fig. 3.1), namely an off-axis incident angle on the lens in front of the cameras, causes coma which is a reasonable explanation for the asymmetric diffraction patterns in Fig. 3.3a and 3.3b. In Fig. 3.3c, an one and a half years older calibration image taken by G. A. BECKER can be seen. Here, the test target was illuminated by a broadband nonlinear optical parametric amplification (NOPA) light pulse [169] and the diffraction pattern of small dirt particles are symmetric. Hence, the experimental setup in Fig. 3.1 was probably slightly misaligned during the experiments of this thesis. Due to limited laser beam time, the systematic calibration of the imaging setup has been done after the laser-solid experiments. Hence, the experimental data shown in chapter 4 is most likely influenced by coma. This shows, that

¹The Scheimpflug condition states for imaging at an oblique angle (like in the present thesis) that an object plane is imaged sharply onto an image plane if the image plane is tilted so the intersection of the object plane and the middle plane of the lens lies in the object plane [172]



(a) Calibration image taken on July 29, 2021.

(b) Calibration image taken on July 29, 2021.



(c) Calibration image taken on January 21, 2020, by G. A. BECKER (georg.becker@uni-jena.de).

Figure 3.3.: Images of a positive 1951 USAF resolution test target taken with camera 1. In contrast to the setup shown in Fig. 3.1, the Wollaston prism, the ND filters, and the color filters were removed from the beam path. Moreover, the test target (located at the target position) was illuminated with a green alignment cw laser incident at 37° to the test target front surface normal in (a) and (b). The width of the visible structures in the images has already been taken into account to calibrate the scaling of the x- and y-axes. The axis labels refer to the geometrical setup specified in Fig. 2.2. Due to imaging at an angle of $\theta = 37^\circ$, only a limited region (in y-direction) of the test target was positioned in the focal plane of the microscope objective and hence sharp. In (a), the horizontal bars are sharp whereas in (b) the test target was moved to bring the vertical bars into focus. Red arrows mark dust particle which show an asymmetric diffraction pattern. (c) shows also an image of a positive 1951 USAF resolution test target taken one and a half year ago with the same experimental setup (without the fused silica wedge). In that way, the influence of changes in the alignment on the imaging is illustrated. Moreover, the test target was illuminated with a broadband (700 nm to 900 nm) nonlinear optical parametric amplification (NOPA) light pulse in (c).

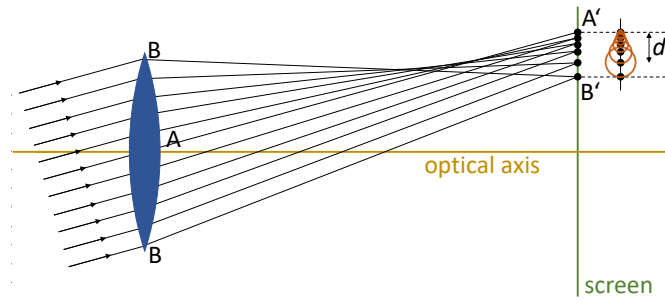


Figure 3.4.: Illustration of coma. The off-axis incident rays from a point object at infinite distance are imaged onto different points on the screen. In two dimensions, those points form circles (orange) as schematically shown on the right. Figure reproduced in modified form from [117].

it is important to check the alignment of the experimental setup before the experiment to correct for any misalignment.

Due to these systematic errors, the size and shape of the rear surface COR emission spot, as imaged in the experiment, can be trusted only to a certain extent. The total pixel count, however, is proportional to the energy of the emitted COR and therefore unaffected by these systematic errors. Moreover, either the test target was slightly rotated or the periscopes were misaligned because the horizontal bars in Fig. 3.3a are supposed to be parallel to the edges of the image which they are not.

Relative Intensity Calibration In the experiments of this thesis, rear surface COR was investigated in three different wavelength regimes with three cameras (as sketched in Fig. 3.1). To compare the data from the three cameras, they need to be intensity-calibrated with respect to each other. To do so, the spectral transmission data of the absorptive ND filters provided by the manufacturer [173] has been used. As described in section 2.5.3, the spectrum of COR shows maxima at harmonics of the central laser frequency with increasing spectral intensity at wavelengths closer to those harmonics. Thus, the spectral transmission data has been interpolated and evaluated at 515 nm for camera 1, at 1030 nm for camera 2, and at 975 nm for camera 3 due to the chosen spectral filters¹. Now, the camera images have been divided by the product of the spectral transmission of the ND filters placed between the microscope objective and the corresponding camera to relatively calibrate the measured intensity. Next, the images have been divided by the quantum efficiency of the camera, provided by the manufacturer. As discussed before in the context of the ND filters, the quantum efficiency is evaluated at the wavelength of the spectral regime investigated by the respective camera. Moreover, the camera images have been noise-corrected. To do so, the mean value of a camera region without COR-signal (at an edge of the image) has been subtracted from the image. As the benefit does not justify the effort, the cameras are not absolutely intensity-calibrated but only relatively with respect to each other. Therefore, the measured COR intensity is given in arbitrary units (arb. u.) throughout this thesis.

¹Camera 3 investigated the spectral region from 900 nm to 1000 nm. However, the spectral intensity of the measured COR is expected to be much stronger close to 1000 nm than close to 900 nm. Therefore, it has been chosen to use the spectral transmission of the ND filters at 975 nm instead of 950 nm which would lie in the middle of the investigated region. After all, the difference in transmission between 975 nm and 950 nm is relatively small.

3.3.2. Wollaston Prism

In section 2.5, it is discussed how the polarization of the observed TR and SR depends on the direction of motion of the hot electrons. Moreover, C. BELLEI *et al.* demonstrated that analyzing the polarization of the emitted COR allows to determine if SR or TR is the main emission mechanism of the observed radiation [75]. To measure the polarization of the COR at the second harmonic (515 nm), a Wollaston prism has been positioned in front of camera 1. The Wollaston prism¹ was rotated in a way that it vertically separates radiation perpendicular (S-polarization in geometry of Fig. 2.2) and parallel (P-polarization in geometry of Fig. 2.2) to the optical table by 1.06° (at 515 nm). Hence, both polarizations were separated spatially after a few centimeter propagation but still could be measured on the same camera.

General Working Principle A Wollaston prism is formed of two birefringent prism, usually made of quartz or calcite, which are cut at a certain angle and glued together so the optical axes of the two prisms are perpendicular to each other and to the front and rear surface normal of the prism. This is sketched in Fig. 3.5. Light entering from the left in Fig. 3.5 travels until the intersection of the two prisms where double refraction takes place. Double refraction refers to the fact that light which is polarized parallel to the optical axis of the second prism is refracted at a different angle than light which is polarized perpendicular to the optical axis of the second prism [117].

Evaluation of Polarization Resolved Images Due to the angular separation introduced by the Wollaston prism, two images, one for each polarization direction, appeared on camera 1. This can be seen in the calibration camera image of an Al foil edge in Fig. 3.6. The foil covered half of the hole in the target holder. The reflection from the rear side of the fused silica beam splitter can be seen on the right side of the camera image in Fig. 3.6 but is ignored in the analysis of the experimental data. The upper image (inside the magenta rectangle) corresponds to the image of the P-polarized radiation transmitted through the hole whereas the lower image (inside the lime rectangle) corresponds to the S-polarized radiation. In an actual experiment (as presented in section 4.1), the magenta (lime) rectangle in Fig. 3.6 contains the image of the P-polarized (S-polarized) COR from the target rear side. The analysis of the experimental results requires to overlap the two images on camera 1. Hence, the vertical and horizontal separation of the two images in Fig. 3.6 needs to be determined as a calibration. To do so, a green alignment laser incident at 37° to the target front surface normal was used to image the edge of an Al foil, which covered half of the hole in the target holder, on camera 1. The two normalized images of the edge on camera 1 (regions framed in magenta and lime in Fig. 3.6) have been overlapped and the absolute difference has been minimized by shifting the position of one image with respect to the other one. Using the calibrated vertical and horizontal separation between the two images on camera 1, the space-resolved polarization

¹The uncoated prism is made from Crystal Quartz for a wavelength range from 400 nm to 2 μ m. More details can be found at [174].

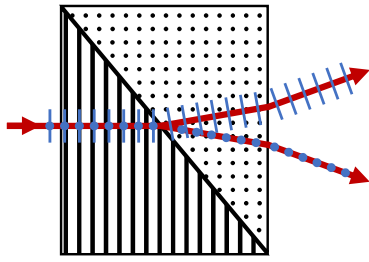


Figure 3.5.: Schematic drawing of the cross-section of a Wollaston prism which consists of two birefringent crystals whose optical axes (indicated as black dots and lines) are perpendicular to each other. The light is incident normal to the front surface. The polarization direction of the light is indicated by blue lines and dots. Due to double-refraction at the intersection of the two prisms, the light is separated in two beams which are polarized perpendicular (upper beam) and parallel (lower beam) to the optical axis of the second crystal.

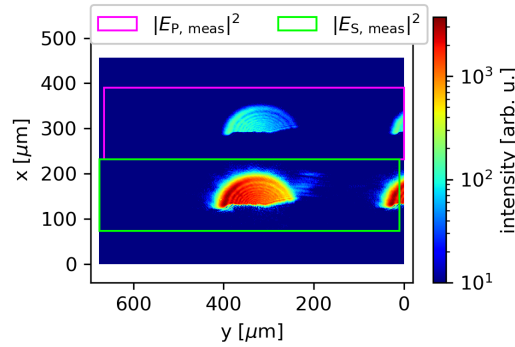


Figure 3.6.: Raw camera image (acquired with camera 1) of the edge of an Al foil, which covered half of the hole in the target holder. In contrast to the experimental setup in Fig. 3.1, no ND filters and no color filters were used and the target was illuminated with a green alignment laser incident at 37° to the front surface normal. The Wollaston prism splits the slightly diagonal polarized light transmitted through the hole into two images on the camera chip, one for each polarization direction (as specified in the legend). The noise level was determined from an empty image region and subtracted from every pixel. The lower limit of the color scale is chosen to lie above the noise.

ratio of the measured electric field strengths $|E_S(x, y)|/|E_P(x, y)|$ of S- and P-polarized COR could be calculated (see section 4.1).

For a Wollaston prism which is aligned perfectly parallel to the optical table, the horizontal separation is zero. This is however not the case in Fig. 3.6. Due to an alignment error before the experiment, the Wollaston prism was rotated. Hence, the polarization was measured in reference to the optical axes of the rotated Wollaston prism. To correct for this, the electric field strengths of S- and P-polarized light measured in the reference system of the Wollaston prism ($E_{S, \text{meas}}$ and $E_{P, \text{meas}}$) have been projected on the axes perpendicular (S-polarization in geometry of Fig. 2.2) and parallel (P-polarization in geometry of Fig. 2.2) to the optical table.

Data Correction Considering the Fresnel equations of refraction [2], one can see that the reflectivity of the fused silica plate in front of camera 1 which is used as a beam splitter (sketched as a slightly transparent, blue bar in Fig. 3.1) has the strongest influence on the measured polarization. The refractive index of fused silica is $n_{\text{FS}}(515 \text{ nm}) \approx 1.46$ [175–177]. Hence, the reflected intensity is roughly a factor of 12 larger for S-polarized light incident at 45° on the quartz plate as compared to P-polarized light. To compensate this difference in

reflectivity, the measured intensity of S and P polarized light has been divided by the respective reflectivity of the fused silica plate. Additionally, the images of S- and P-polarized COR have been corrected for the polarization dependent transmission of the fused silica wedge which was located between the two periscopes in Fig. 3.1.

Furthermore, the polarization information acquired with the Wollaston prism was used for the relative intensity calibration of camera 2 and 3 without a Wollaston prism placed in front of them (see Fig. 3.1). To do so, camera 2 is corrected for the transmission of the first fused silica plate and for the reflectivity of the second fused silica plate in the beam path. Camera 3, on the other hand, is corrected for the transmission of the first and second fused silica plate in the beam path and for the reflectivity of the third fused silica plate. The transmission and reflectivity are calculated as a sum of the transmission and reflectivity of S- and P-polarized light, weighted by the relative amount of S- and P-polarized COR measured with camera 1 for every laser shot. The transmission and reflectivity is evaluated at the wavelength according to the spectral regime investigated by this camera, as discussed in the paragraph Relative Intensity Calibration on page 36. This calibration procedure, however, assumes that the polarization is similar in the different spectral regimes investigated with the cameras (see Fig. 3.1). Admittedly, the COR in the different spectral regimes is expected to be caused by electrons with a different temporal structure. On one hand, the COR at the laser frequency (investigated by camera 2) is predominantly caused by hot electrons which are accelerated at the laser frequency ω_L at the target front side. On the other hand, COR at the second harmonic (investigated by camera 1) and in between (investigated by camera 3 (900–1000 nm)) is caused by two hot electron populations, namely hot electrons accelerated at ω_L and at $2\omega_L$. However, for a first approximation it is reasonable to assume that the momentum distribution of the hot electron population, which mainly determines the polarization of COR, is similar for these two electron currents. Hence, it can be assumed that the polarization is similar in the different spectral regimes investigated by the cameras. This assumption may introduce a certain error. However, neglecting completely the transmission and reflectivity of the fused silica plates for camera 2 and 3 is expected to introduce an even larger systematic error.

4. Experimental Investigation of Optical Rear Surface Radiation

A better understanding of the transport of large electron currents through an overdense plasma may lead to further progress and improvements in Fast Ignition (FI) in Inertial Confinement Fusion (ICF) and laser-driven ion acceleration (e.g. via Target-Normal-Sheath-Acceleration (TNSA)). To study such electron transport, the POLARIS laser was focused onto thin Al target foils as sketched in Fig. 3.1. In such a situation, the target is ionized by the laser and a certain fraction of the laser pulse energy is absorbed to accelerate electrons towards the target rear surface as described in section 2.1 and 2.3. The optical rear surface radiation emitted by these fast electrons is studied and characterized systematically in this chapter using the experimental setup displayed in Fig. 3.1. The presented studies allow some general conclusions on the parameters and the transport of the fast electrons which emitted the measured radiation.

The rear surface emission region was imaged onto three cameras equipped with different spectral filters. In that way, the rear surface radiation was measured spatially resolved at the second harmonic (515 nm), the central laser frequency (1030 nm), and in an intermediate region (900 nm to 1000 nm). Moreover, a Wollaston prism was placed in front of camera 1 to additionally measure the polarization characteristics of the radiation at 515 nm spatially resolved. With these diagnostics at hand, the COR emitted from Al targets of varying thickness (0.4–8 μm) was investigated for incident laser intensities ranging from $3 \times 10^{18} \text{ W/cm}^2$ to $3 \times 10^{19} \text{ W/cm}^2$.

This chapter is structured as follows: First, exemplary camera images are presented for different target thicknesses to qualitatively analyze the spatial intensity distribution of the imaged COR emission spot. Next, the experimental results of the scaling of the total emitted COR with laser intensity and target thickness are presented and compared to calculations and results from literature. This allows to draw some conclusions on the laser absorption at the target front side and the characteristic energy of the hot electron distribution. The last section is dedicated to a systematic analysis of the polarization characteristics of the emitted COR radiation.

Important Note Due to the comparably long exposure time of the cameras, the time-integrated spatial intensity distribution, i.e. the fluence, of COR has been measured. However, the term intensity is often used throughout this chapter instead of the physically precise term fluence. Hence, one should always keep in mind that without further specification it is always referred to the time-integrated intensity and time-integrated electric field strength of

the measured COR in this chapter.

4.1. Exemplary Camera Images of Coherent Optical Radiation (COR)

Hundreds of images have been acquired of COR emitted from thin Al foil rear surfaces. Therefore, some exemplary images have been chosen to give a first qualitative impression of the COR images which form the basis of the more quantitative analysis in the following sections. The selected images are representative of the general spatial structure of the imaged rear surface COR emission spot for the different target thicknesses and experiment days. However, the COR images vary slightly from laser pulse to laser pulse for the same target (as shown in Fig. E.2). This might be due to fluctuations in the POLARIS laser (e.g. fluctuations in intensity and pulse duration or spatial, angular and spectral fluctuations in the pulse front). Also fluctuations or unknown underlying correlations in the hot electron generation, acceleration and propagation, which influence the emission of COR, may cause the shot-to-shot differences in the measured COR.

The exemplary COR images are plotted in Fig. 4.1 for different target thicknesses as specified in the subfigure headings. Fig. 4.1a to 4.1c show data from experiment day #1, whereas the exemplary COR images from experiment day #2 are shown in Fig. 4.1d to 4.1f. The characteristics of the laser pulse, which induced the emission of the measured COR, are specified in the heading of each subfigure. Moreover, the horizontal angle $\varphi_{\text{parabola}}$ of the parabola which focuses the laser pulse on the target is stated in the subfigure heading. The horizontal parabola angle $\varphi_{\text{parabola}}$ influences the position of the laser focal spot at the target front surface and therefore also the position of the imaged COR emission spot at the target rear surface. Each subfigure contains four color plots which show the intensity and polarization distribution of the rear surface COR emission spot imaged with the three cameras (see Fig. 3.1 for the experimental setup). The camera is specified in the heading of each color plot according to the spectral range which is investigated by this camera.

The imaged rear surface COR emission spot is oriented as if one would look directly at the target rear side with the coordinate system specified in Fig. 2.2. Whereas the scaling of the x- and y-axes has been calibrated to investigate the COR's source size at the target rear surface, the offset of the x- and y-axes has not been calibrated. Therefore, a white line is plotted which acts as a y-axis-reference to compare the position of COR at the target rear between the different cameras. This white line refers to a fixed position at the target rear surface. Moreover, the axes of the four plots within one subfigure span the same range.

The first, third, and fourth plot of every subfigure show the spatially resolved COR intensity in different spectral regions. The latter two plots, however, could not be precisely corrected for the polarization dependent transmission and reflectivity of the fused silica wedge and plate in the beam path as no Wollaston prism was placed in front of those cameras to measure the polarization. The second plot of each subfigure shows the polarization characteristics by plotting the ratio $|E_S|/|E_P|$ of the absolute electric field strength at (520 ± 20) nm for

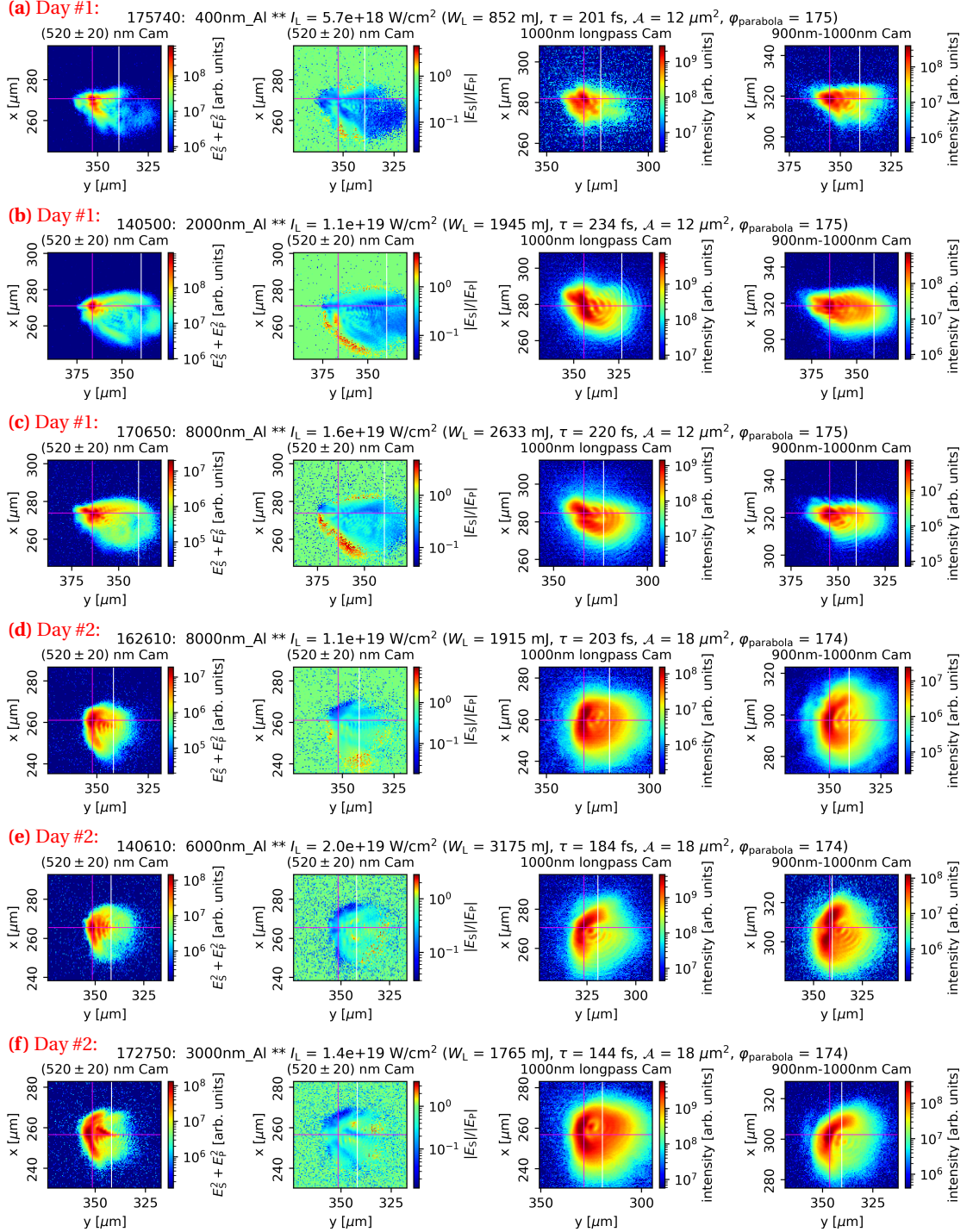


Figure 4.1.: Plots of the (time-integrated) intensity I and polarization characteristics of the COR measured on two days in different spectral ranges. The AI target thickness is specified together with the laser parameters and the horizontal angle of the focusing parabola (in arbitrary units) in the heading of each subfigure, which consists of four color plots. The underlying camera is specified in the plot heading. A magenta crosshair marks the center of mass (c.o.m.) of the region where the measured intensity I fulfills $I > I_{\text{max}}/2$. The x- and y-axes are not offset calibrated. Therefore, the white line acts as a y-axis-reference because it refers to a fixed position at the target rear surface.

the two measured polarization directions (horizontal (E_P) and vertical (E_S) to the optical table or to the y-axis according to Fig. 3.1). In that way, spatial variations in the polarization of the imaged COR emission spot can be seen. The ratio $|E_S|/|E_P|$ has first been initialized as an array of ones. To avoid numerical complications, the ratio $|E_S|/|E_P|$ has only been calculated at positions where both, numerator and denominator are not zero. The intensity plots in Fig. 4.1 have a logarithmic color scale to make structures at low intensity visible. Additionally, the data of Fig. 4.1 are plotted in Fig. E.1 with a linear color scale.

4.1.1. Shape and Position of the COR Intensity Distribution

If one looks at the intensity plots in Fig. 4.1 (and Fig. E.2), a few general things can be observed: First of all, the COR shows one (or more) small maxima next to the center of mass (c.o.m.) which are surrounded by a large region of low-intensity COR. The large region of low-intensity COR might be due to recirculating electrons as suggested in [75]. Moreover, the COR intensity distribution is asymmetric. As one can see by comparing the distance between c.o.m. (magenta crosshair) and y-axis-reference (white line) for shots with the same horizontal parabola angle $\varphi_{\text{parabola}}$, the COR emission spot moves by several micrometers for consecutive shots. Hence, the COR will often lie outside of the sharp focal region. Because of imaging at an angle of $\theta = 37^\circ$ instead of $\theta = 0^\circ$, the focal region of the microscope objective spans roughly $20\mu\text{m}$ in y-direction. Due to the high experimental complexity, only a coarse alignment of the position of the focal region of the microscope objective with respect to the COR emission spot position was done. Hence, the COR emission spot was maybe located systematically outside of the focal region of the microscope objective.

4.1.1.1. Approaches to Explain Asymmetry in COR Images

Coma As discussed in section 3.3.1, the imaging setup was probably misaligned during the experiment and the imaging aberration coma was present. Coma makes symmetric objects appear as asymmetric images on the camera. This could be seen for small dust particles on a test target in Fig. 3.3a and 3.3b. Therefore, coma is among the more likely explanations for the asymmetry in the COR Images in Fig. 4.1, E.1, and E.2.

Laser Focal Intensity Distribution In comparison, the laser focal spot on the target front surface is more symmetric than the COR images, as one can see in Fig. 4.2. However, the focus is already at low laser pulse energy slightly asymmetric. As the laser focal spot cannot be measured at full laser energy [169], it remains unclear how the laser intensity distribution on the target front surface looked like during the experiment. One would at least expect that the laser focal spot (Fig. 4.2) becomes rather more asymmetric than more symmetric if the laser energy is increased [169, 178]. Moreover, it is also unclear what spatial phase was imprinted on the laser pulse by the plasma mirror (PM) [169] as the laser focal spot in Fig. 4.2 was measured using the silver edge of the PM. Depending on the time between ionization of the PM surface and reflection of the main laser pulse, the plasma surface of the PM expands and parts of the main laser pulse might be reflected from a curved PM surface. The phase

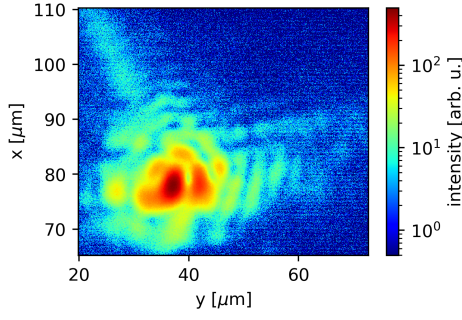


Figure 4.2.: Time-integrated intensity (i.e. fluence) distribution of the focal spot of the POLARIS laser at low energy and in logarithmic scale. The focal spot area is $\mathcal{A}_{\text{FWHM}} \approx 11.1 \mu\text{m}$ and the q-factor is $q_{\text{FWHM}} = 0.12$ (as defined in Eq. 3.2 and 3.3). The focal spot was measured at experiment day #1 using the focus (microscope) objective (as schematically shown in Fig. 3.2 in [103]). The scaling of the x- and y-axis has been extracted from the focus imaging program. Furthermore, the plotted intensity distribution has been noise-corrected.

imprinted by a curved PM surface varies across the focal spot and therefore additionally influences the intensity distribution of the laser focus on the target surface. However, the phase imprinted by the PM on the laser pulse is expected to be negligible in the presented experiments due to the sufficient low pulse duration and fluence (on the PM) of the POLARIS laser [179]. Additionally, the plasma at the target surface was probably already expanded to a certain extent at the arrival of the main laser pulse due to the rather flat rising edge of the POLARIS laser pulse [169]. Hence, the laser intensity distribution on the plasma surface probably deviated from the measured focal spot in Fig. 4.2 as the laser pulse was probably reflected by the plasma before reaching the focal spot position.

A Diverging Electron Beam Imaged at 37° A different explanation for the asymmetric COR images is a diverging electron beam. As COR is emitted inside a cone which points in the electron propagation direction, more radiation is collected by the microscope objective from those electrons who fly towards to microscope objective ($\theta = 37^\circ$). To illustrate this idea, a diverging electron beam is assumed which center is directed normal to the target rear surface. Electrons which fly towards the microscope objective hit the target rear surface left of the center of the electron beam. Hence, the COR intensity distribution imaged at an oblique angle of 37° with the microscope objective is expected to be asymmetric for a diverging electron beam. However, calculations indicate that the asymmetry introduced by such imaging at oblique angle is not large enough to explain the asymmetry in the imaged rear surface COR emission spots shown in Fig. 4.1.

Chromatic Transmission of Fused Silica Wedge Due to Snell's law of refraction and the wavelength dependent refractive index of fused silica [175–177], the transmitted light at the fused silica wedge is spatially and angularly separated in its different wavelength components. Hence, the images should appear smeared out on the camera chip. However, the angular separation for radiation at the second harmonic, assuming a FWHM of 10 nm^1 , is only 0.002° [180]. This angular chromaticity, introduced by the wedge, results in a separation of roughly 5 pixels on the camera between radiation at 510 nm and radiation at 520 nm. There-

¹This is on average the FWHM of the spectral peak observed with the imaging spectrometer.

fore, angular chromaticity, introduced by the wedge, is not sufficient to explain the asymmetry in the COR images. Moreover, already the calibration images in Fig. 3.3a and 3.3b, taken with a narrowband cw laser, show asymmetry. Nevertheless, the fused silica wedge and also the plates in front of the cameras slightly smear out the COR images along the horizontal axis.

Conclusion on Asymmetry The observed asymmetry of the COR images cannot be explained by simple geometric considerations (including the asymmetric imaging geometry) or when taking into account the asymmetry of the focal spot. However, the total pixel count of a camera image is unaffected by the asymmetry and by systematic imaging errors. The sections 4.2 to 4.4 therefore focus on the total pixel count, corresponding to the energy of the emitted COR in different spectral regimes.

4.1.2. COR Spatial Intensity Distribution for Different Target Thicknesses and Spectral Regions

If one compares the COR plots (in Fig. 4.1) taken with the same camera and at the same experiment day but for different target thicknesses, the general structure of the spatial COR intensity distribution remains the same whereas the intense region of COR ($I > I_{\max}/2$) around the c.o.m. varies (see Fig. 4.1a to 4.1c and Fig. 4.1d to 4.1f). However, these differences in the intense region of COR are also present for successive images when the target thickness remains unchanged (see Fig. E.2). Therefore, these shot-to-shot fluctuations in COR are probably due to fluctuations in the POLARIS laser and/or in the hot electron generation, acceleration, and propagation, as mentioned in the beginning of this section, which strongly depend on the exact laser parameters on a specific laser shot. Moreover, the COR images look systematically different for the two experiment days from which the data is presented in Fig. 4.1. Most likely, undesired changes in the POLARIS laser (e.g. changes in the temporal pulse structure or spatial, angular, and spectral changes in the pulse front) are responsible for the general difference between the COR images from two experiment days. Hence, the data from different experiment days can only be compared to a certain extent. The rest of this thesis therefore focuses almost entirely on the data from experiment day #1 where a larger range of target thicknesses was investigated.

Comparing the COR intensity distribution acquired with the different cameras in different spectral regimes is also very insightful. In general, the COR at 1030 nm (1000 nm longpass camera) is roughly an order of magnitude more intense than the COR radiation at the second harmonic ((520 ± 20) nm camera) and in the regime between (900–1000 nm camera). This is investigated in more detail in section 4.3. Moreover, the COR intensity distributions (for the same laser shot) in Fig. 4.1 vary in shape and relative position (distance between c.o.m. and y-axis-reference line) for the different investigated spectral regimes. The most likely explanation is that these differences are linked to differences in the hot electron current which emitted the COR at the target rear side. The COR at the laser frequency (1000 nm longpass camera) is predominantly caused by hot electron bunches which are generated at

the laser frequency ω_L (see Fig. C.1) at the target front side and then accelerated into the target. On the other hand, COR at the second harmonic ((520 ± 20) nm camera) and in between (900–1000 nm) is caused by hot electron bunches generated at ω_L and bunches produced at $2\omega_L$. Due to the differences in the acceleration at the target front side between hot electron bunches produced at ω_L and bunches generated at $2\omega_L$, it is very likely that one can expect also spatial differences in the COR emitted by these hot electrons at the target rear side. However, a quantitative analysis, where the COR emission spot position on the three cameras was compared, showed no correlation with target thickness or laser intensity.

4.1.2.1. Source Size of COR, Pinching, Filamentation and Divergence

All the images in Fig. 4.1 show the clear tendency that the intense region of COR ($I > I_{\max}/2$) is larger at longer radiation wavelengths. To investigate this observation, a quantitative analysis is carried out in this subsection. Due to fluctuations in the COR emission spot position and imaging at $\theta = 37^\circ$, the COR emission spot was rarely in the focal plane of the microscope objective, as discussed before. Hence, the absolute size of the COR image is systematically too large if the COR emission at the target rear surface is not in the focal plane of the microscope objective. Therefore, the COR's source size is relatively compared between camera 1 ((520 ± 20) nm) and camera 3 (900–1000 nm). In the spectral regions investigated by these cameras, both types of hot electrons, electron bunches generated at ω_L and electron bunches generated at $2\omega_L$, are expected to contribute significantly to the total measured COR. In comparison, camera 2 (1000 nm longpass) measures mainly COR emitted by hot electron bunches produced at ω_L , because the COR spectrum of hot electron bunches generated at $2\omega_L$ has no maximum at ω_L (see Eq. 2.42 and Fig. C.1).

From Fig. 4.3 it can be seen that the COR exhibits a systematically smaller area at 515 nm than in the range from 900 nm to 1000 nm. However, the variance of the data points in Fig. 4.3 is very large. As the COR at 515 nm and in the range from 900 nm to 1000 nm is expected to be caused by the same electrons, it is surprising that the COR's source size is smaller at 515 nm. However, a possible explanation could be the size of the hot electron beam which caused the COR. If the size of the electron beam is below the resolution limit of the microscope objective in the range from 900 nm to 1000 nm, the image of the COR caused by this electron beam is smaller on the (520 ± 20) nm camera than on the 900–1000 nm camera. The resolution limit of a microscope objective is given as $d_{\lim} = 0.61\lambda/\text{NA}$, where λ is the wavelength of the light and NA is the numerical aperture of the microscope objective [1]. For light with a wavelength of 515 nm, the theoretical resolution limit of the used imaging setup (see Fig. 3.1) is $d_{\lim} \approx 1.2\mu\text{m}$, whereas $d_{\lim}(\lambda = 1000\text{ nm}) \approx 2.3\mu\text{m}$. Hence, the area ratio plotted in Fig. 4.3 provides information on the COR's actual source size. An area ratio $\mathcal{A}_{\text{FWHM}}((520 \pm 20)\text{ nm})/\mathcal{A}_{\text{FWHM}}(900\text{--}1000\text{ nm})$ of unity corresponds to source size of COR which is equal to or larger than the resolution limit of the 900–1000 nm camera ($d_{\lim} \approx 2.3\mu\text{m}$). The closer $\mathcal{A}_{\text{FWHM}}((520 \pm 20)\text{ nm})/\mathcal{A}_{\text{FWHM}}(900\text{--}1000\text{ nm})$ is to the value 0.27, the closer the COR's source size is to the resolution limit of the (520 ± 20) nm camera ($d_{\lim} \approx 1.2\mu\text{m}$). Hence, in the range from 0.27 to 1, the area ratio is expected to be propor-

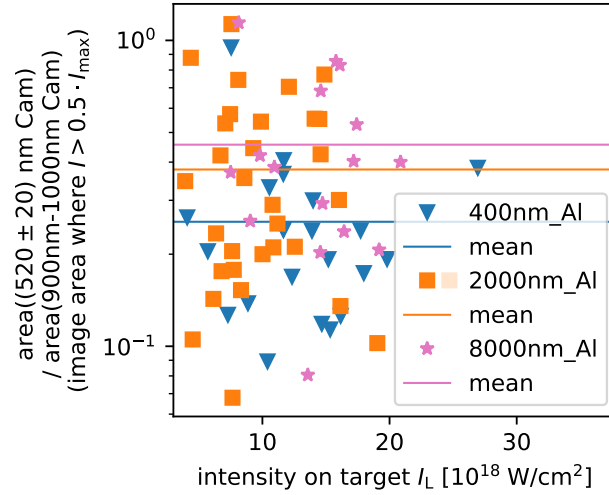


Figure 4.3.: The COR area $\mathcal{A}_{\text{FWHM}}$ extracted from the (520 ± 20) nm camera divided by the COR area $\mathcal{A}_{\text{FWHM}}$ extracted from the 900–1000 nm camera. The area ratio is plotted for different target thicknesses (specified in the legend) as a function of the laser intensity. Every data point has been extracted from the COR images acquired for this particular laser shot. The area has been determined by multiplying the calibrated area of a single pixel with the number of pixels where $I > I_{\text{max}}/2$ is fulfilled. Moreover, the mean value of all the data points of the corresponding target thickness is displayed as a line.

tional to the actual area of the COR emission spot. Therefore, it can be concluded that for most laser shots the COR's source size (FWHM diameter) ranged between $1.2 \mu\text{m}$ and $2.3 \mu\text{m}$ (i.e. the resolution limits of the (520 ± 20) nm camera and the 900–1000 nm camera). Moreover, the mean value of the area ratio decreases with decreasing target thickness. This is an indication for a diverging hot electron beam which is larger at the target rear surface for thicker targets.

Due to the large variation of the data points in Fig. 4.3, however, it cannot be excluded that the electron beam size is even below the resolution limit of the (520 ± 20) nm camera ($d_{\text{lim}}(\lambda = 515 \text{ nm}) \approx 1.2 \mu\text{m}$). Such small electron beam diameters would also explain the diffraction rings visible in Fig. 4.1, Fig. E.1, and Fig. E.2.

Already electron beam sizes below the resolution limit of the 900–1000 nm camera are roughly a factor of two smaller in diameter than the laser focal spot. It might be that only the very central and intense part of the spatial intensity distribution in the focus accelerates electrons coherently towards the target rear surface. However, also electron beam pinching (see section 2.4.1) or filamentation (see section 2.4.2) could explain the reduction of the hot electron beam diameter. Filamentation could also explain why the COR images have more than one local maximum for some laser shots (see e.g. Fig. E.2g or Fig. E.2c). So far, however, filamentation has been usually observed in experiments and simulations with thicker targets [69, 71, 73, 181–183] and only recently in a sub-micron liquid target [184].

4.1.2.2. Diffraction pattern in COR Spatial Intensity Distribution

Finally, one should point out that some COR intensity distributions in Fig. 4.1 show a circular diffraction pattern. However, the origin of this diffraction pattern is unclear. If the limited size of the imaging optics (microscope objective, mirrors, lens) acted as an aperture, one would expect a consistently pronounced diffraction pattern throughout all COR images. A second possible explanation could be that the COR emission spot is actually smaller than the resolution limit of the imaging system at the investigated wavelength, as discussed above. The image of such a small radiation source is expected to look like the diffraction pattern of a point source (like e.g. in the case of the dust particles in Fig. 3.3). The asymmetry of the diffraction pattern in the COR images in Fig. 4.1 is then probably due to coma, as discussed in section 4.1.1.1.

4.1.3. Space-Resolved Polarization of COR

The polarization of COR was measured to learn more about the main emission mechanism (SR or TR) and about the electron current which gave rise to this COR emission. However, systematic imaging errors, i.e. the limited size of the focal region and coma, inhibit a detailed analysis of the spatial polarization ratio $|E_S|/|E_P|$ plotted in Fig. 4.1. Still, some general observations can be made: The fluctuations in the COR intensity distribution for consecutive laser shots also influence the polarization ratio as it can be seen in Fig. E.2. Moreover, the general spatial structure of the polarization ratio is significantly different for the two experiment days as it can be seen in Fig. 4.1. For day #1, the COR is dominantly S-polarized (i.e. polarized along the x-axis) at the upper and lower edge of the COR intensity distribution. Consequently, the rest of the COR (i.e. the central, left, and right region) emission spot is mainly P-polarized (i.e. polarized along the y-axis). On day #2, on the contrary, the measured COR is mainly P-polarized in the left, the upper, and the central part of the COR emission spot with a faint "background" of COR in the right and lower part of the COR spot. In general, the COR polarization ratio changes strongly across the COR emission region. This observation suggests that CSR is the main emission process responsible for the observed COR [75]. In case of CSR, the polarization differences across the COR emission spot are due to differences in the direction in which the electrons travel before hitting the target rear surface again (see section 2.5.1). To resolve the question if rather SR or TR is the main emission process responsible for the observed COR, a more quantitative analysis together with some assisting calculations is given in section 4.3 (and appendix D).

4.2. Scaling of COR Energy with Laser Intensity

The total emitted COR energy W_{COR} per laser shot, in the spectral range investigated by the respective camera, is a relatively robust measure of COR. The total COR energy is unaffected by imaging errors and position and shape variations of the imaged rear surface COR emission spot. W_{COR} is proportional to the total pixel count of the COR camera image, which has been calibrated according to the procedures described in section 3.3. The W_{COR} measured with

the three different cameras on experiment day #1 is plotted in Fig. 4.4 for the different target thicknesses as a function of laser intensity I_L . Moreover, the function $W_{\text{fit}}(I_L) = G \cdot I_L^{\Xi}$ with the variable parameters G and Ξ has been fitted to the measured $W_{\text{COR}}(I_L)$ to quantify and compare the intensity scaling of COR.

The total emitted COR energy W_{COR} increases strongly with an increasing laser intensity I_L on the target. The fitted functions indicate that W_{COR} is proportional to I_L^{Ξ} , with the laser intensity I_L on target and the exponent Ξ ranging from 2 to 4. The fitted exponent Ξ in Fig. 4.4 increases with target thickness. Hence, W_{COR} scales stronger with I_L for thicker targets as discussed below. Moreover, the fitted exponents Ξ are comparable between the (520 ± 20) nm camera and the 1000 nm longpass camera. The intensity scaling of the 900–1000 nm camera differs from the other two investigated spectral regimes for the $2\mu\text{m}$ and $8\mu\text{m}$ thick target. However, the variance of the data points in Fig. 4.4 is very high and therefore the quality and the representativity of the fits in Fig. 4.4 are limited. Furthermore, the number of data points is roughly a factor of two higher for the $2\mu\text{m}$ thick target as compared to the other investigated target thicknesses. Hence, the experimental data in Fig. 4.4 is more conclusive for the $2\mu\text{m}$ thick target. Consequently, more data points would be beneficial to counteract the strong variance of the measured W_{COR} in Fig. 4.4. However, the number of data points is limited by the available number of laser shots before the target chamber needs to be vented to equip the target holder with new Al foils and to replace the plasma mirror. Hence, the size of the target holder and the plasma mirror limit the number of data points which can be acquired on one experiment day.

To the best of the author's knowledge, there is only one similar work by J. ZHENG *et al.* [68] where the optical rear surface emission from a $50\mu\text{m}$ thick Al foil, irradiated by an high-intensity, ultrashort laser pulse, was investigated as a function of the laser intensity. However, J. ZHENG *et al.* investigated W_{COR} at $\theta = 0^\circ$ by integrating the measured spectrum around the central laser frequency. The laser ($\lambda_L = 1053\text{nm}$, $W_L = 20\text{J}$, $\tau = 600\text{fs}$) was incident at 20° to the target front surface normal and J. ZHENG *et al.* [68] determined an energy scaling of $W_{\text{COR}} \propto I_L^{(3.5 \pm 1.0)}$. This result can, however, not be compared to the results of this thesis due to the difference in target thickness as discussed below.

As discussed in [68] and in section 2.5.3, the two main quantities which are related to the nonlinear increase of COR energy W_{COR} with laser intensity are the temperature T_h and the total number N of hot electrons. In general, the energy of the radiation emitted by a single hot electron (valid for TR and SR) increases with increasing hot electron temperature T_h , and T_h increases with laser intensity I_L as described in section 2.3.2. The increase in W_{COR} with T_h , and hence I_h , due to an increase in the energy radiated by every single hot electron influences the whole COR spectrum.

Furthermore, the coherence of the radiation emitted by the hot electron bunches influences the intensity scaling of W_{COR} in the different investigated spectral ranges. The electrons are assumed to follow a relativistic Maxwellian (Jüttner) momentum distribution ([153] and references therein). An increase in T_h (due to an increase in I_L) causes a relative increase in the number of electrons with velocities close to c . Consequently, the velocity dispersion (i.e. the longitudinal dephasing of an electron bunch due to the different electron velocities

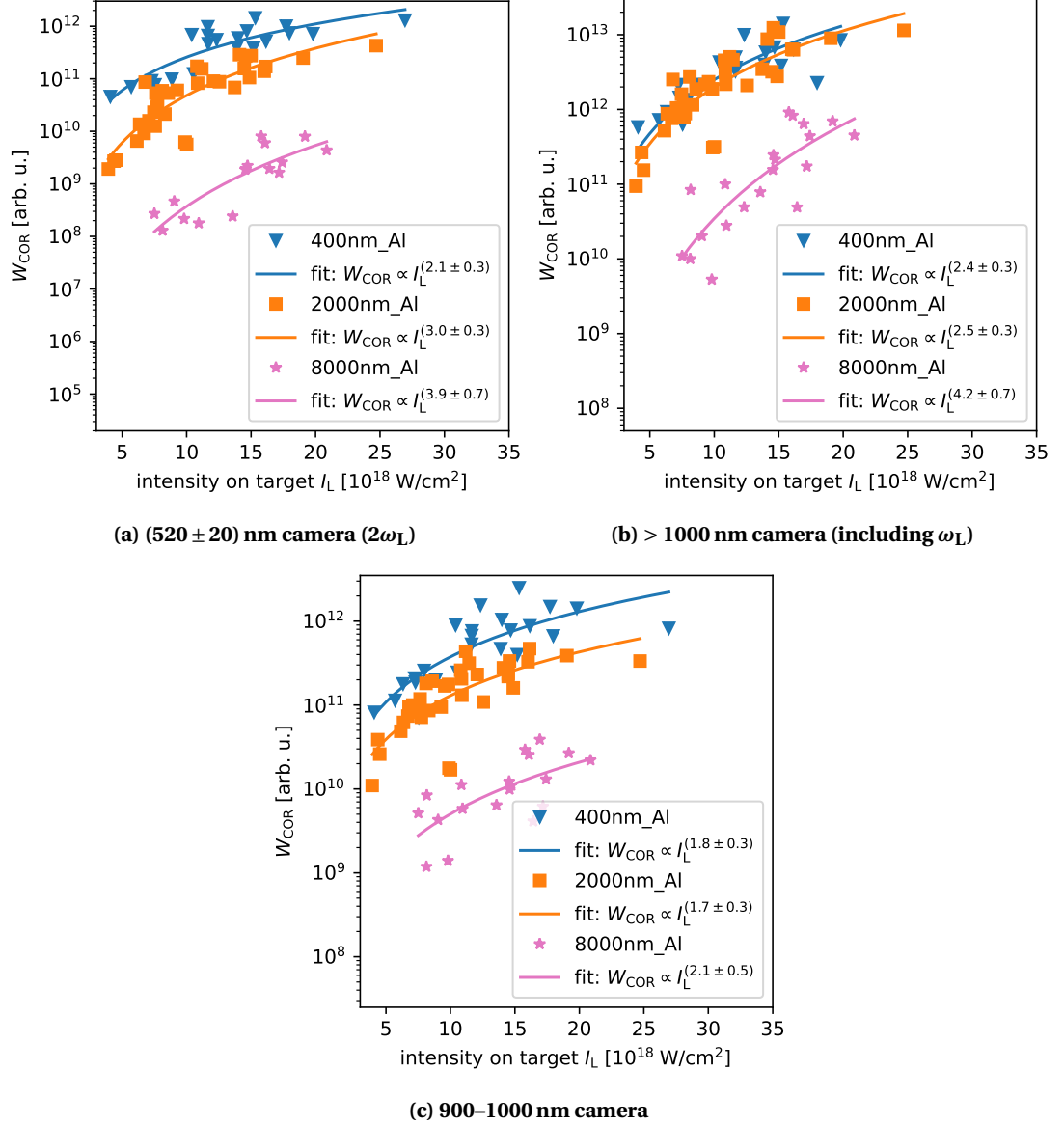


Figure 4.4.: The total COR energy W_{COR} emitted per laser shot in different spectral ranges (i.e. the total pixel count of the calibrated camera) as a function of the intensity on the target front surface. The spectral range is specified in the subfigure heading. Every data point has been extracted from the COR images acquired for this particular laser shot on experiment day #1. The COR energy W_{COR} is plotted for the different investigated target thicknesses. Moreover, the function $W_{\text{fit}} = G \cdot I_L^\Xi$, with the variable parameters G and Ξ , has been fitted to the measured $W_{\text{COR}}(I_L)$ as specified in the legend.

in the bunch) is reduced for higher T_h and thinner targets. The coherence of the emitted radiation by the hot electron bunches increases therefore with an increase in T_h and a decrease in target thickness. A higher coherence of the emitted radiation results in a higher COR intensity at harmonics of the laser frequency (e.g. at ω_L and at $2\omega_L$). Moreover, the increase in coherence with I_L is more pronounced at thicker targets. Here, the coherence of the emitted radiation is stronger reduced by velocity dispersion due to the longer propagation length of the hot electron bunches between acceleration at the target front side and emission of COR at the target rear side. Hence, the experimentally observed stronger intensity scaling of W_{COR} for thicker targets (see fitted exponent Ξ in Fig. 4.4) can be explained by the stronger coherence increase of the emitted radiation with T_h for thicker targets. In contrast, the COR energy in the spectral range between harmonics of the laser frequency decreases (with respect to W_{COR} at ω_L and $2\omega_L$) with increasing coherence. Hence, the lower scaling of W_{COR} with I_L observed with the 900–1000 nm camera, as compared to W_{COR} at harmonics of the laser frequency, is in accordance with the theoretical expectations.

Moreover, the total number of hot electrons is estimated as

$$N = \frac{\Pi_{L \rightarrow e} W_L}{k_B T_h}, \quad (4.1)$$

with the laser pulse energy W_L and the conversion efficiency $\Pi_{L \rightarrow e}$ of laser energy to hot electron energy [81]. Published investigations on quantifying $\Pi_{L \rightarrow e}$ state values between 0.1 and 0.4 [59, 185–187] and therefore $\Pi_{L \rightarrow e} = 0.25$ is chosen as an approximation throughout this thesis. As the increase in T_h with W_L lies below a linear scaling, the hot electron number N is expected to increase with laser pulse energy W_L and hence with laser intensity I_L , because $W_L \propto I_L$.

Whereas the coherence increase with laser intensity I_L is expected to saturate at a certain point, the increase in N , and hence W_{COR} , with I_L is expected to continue even at higher laser intensities. Therefore, the exponent Ξ of the function fitted to W_{COR} in Fig. 4.4 may change with laser intensity I_L . The simple function $W_{\text{fit}} = G \cdot I_L^\Xi$ with a constant exponent Ξ would then no longer be an adequate fit function for the scaling of W_{COR} with I_L . Due to the limited number of data points, their large variance and the limited laser intensity range investigated, such an intensity dependence of the exponent Ξ could not be observed in the experiments of this thesis. It was found that - within the investigated parameter range - this exponent remained constant for a fixed target thickness. In conclusion, it has been shown that the experimentally observed scaling of the total COR energy W_{COR} with laser intensity I_L can be understood qualitatively very well by considering an intensity dependent hot electron number N and temperature T_h .

4.2.1. Intensity Scaling of COR Energy: CTR Model

As discussed above, it is expected that the scaling of the total emitted COR energy W_{COR} with laser intensity depends mainly on the temperature T_h and total number N of hot electrons. To test this dependence, the CTR model which has been introduced in section 2.5.3.1 is used. The total radiated energy by a single electron scales similar for SR and TR with laser inten-

sity. Hence, the results obtained with the CTR model are expected to hold approximately also true for CSR. Nevertheless, it would be better to have a CSR model with a reasonable computational time. However, this is beyond the scope of this work (see section 2.5.3.2 and D.1). Due to limited computational resources, any divergence and space-dependent temperature of the hot electrons is neglected. Hence, the total emitted COR energy (per $d\omega$ and $d\Omega$) W_{COR} has been calculated from Eq. 2.41 after integrating over \vec{r}_\perp to compare it to Fig. 4.4.

Model Parameters The following model parameters are introduced and defined in section 2.5.3.1 and illustrated in Fig. 2.5. The electron beam is expected to be directed normal ($\psi = 0$) to the target rear surface. In accordance with the experimental setup, $\theta = 37^\circ$ has been chosen (see coordinate system defined in Fig. 2.2). Moreover, $\sigma_t = \mathcal{T}_L / (10 \cdot \sqrt{2}) = 0.243$ fs (as proposed in [70] based on PIC results and fits to experimental data) and a number of n_b electron bunches produced at ω_L and $2n_b$ electron bunches generated at $2\omega_L$ (see Eq. 2.43) have been assumed. The scaling of W_{COR} (at 515 nm and 1030 nm) in the presented CTR model does not depend on n_b and a^1 . Based on the results of section 4.3, $P_1/P_2 = 1.41$ has been chosen for the electron bunch charge ratio between hot electrons accelerated at ω_L and hot electrons accelerated at $2\omega_L$ (see Eq. 2.43 and Fig. 2.5). The total hot electron number has been calculated from Eq. 4.1 assuming a constant conversion efficiency $\Pi_{L \rightarrow e}$. Furthermore, the hot electron temperature has been determined from Eq. 2.13. For these parameters, the calculated total emitted COR energy W_{COR} is plotted as a function of intensity and for different target thicknesses and emission wavelengths in Fig. 4.5.

Discussion of Calculation Results The calculated COR energy W_{COR} in Fig. 4.5 shows a similar increase with laser intensity I_L as already observed in the experimental data in Fig. 4.4. In comparison to the experimental data (Fig. 4.4), the calculations have zero variance (no randomness in the simulation model). Therefore, clear differences can be seen between the scaling of W_{COR} with intensity for different target thicknesses and COR wavelengths. The thicker the target and the shorter the COR wavelength, the stronger is the increase of W_{COR} with I_L in the experimentally investigated intensity range. Due to velocity dispersion², the electron bunches are more expanded in propagation direction for thicker targets and the coherence of the radiation, emitted by those bunches, is reduced. The loss of coherence due to longitudinally expanded electron bunches is even greater for shorter wavelengths.

Already the limited region of fitted data points in Fig. 4.5 shows that the function $W_{\text{fit}} = G \cdot I_L^\Xi$ with a fixed exponent Ξ is not an accurate function to describe the scaling of W_{COR} with laser intensity, because W_{COR} decreases strongly with decreasing intensity below 10^{19} W/cm². However, for the comparison to the experimental data the fit function W_{fit} is sufficient. To

¹ It has been decided to use some reasonable values for the laser parameters in the experiment, namely $n_b = 20$ and $a = 1/4v_L$ (based on [70]). However, one should note that the COR intensity ratio between COR at harmonics of the laser frequency (e.g. 515 nm or 1030 nm) and COR in the spectral range between those harmonics depends on n_b and a . It is desirable to limit the number of free parameters of a model for which one has to make an assumption. Therefore, the COR model is evaluated only at 515 nm and 1030 nm in the following.

² Velocity dispersion refers to the expansion of an electron bunch in propagation direction for a non-monoenergetic electron bunch due to the different velocities of the electrons in the bunch.

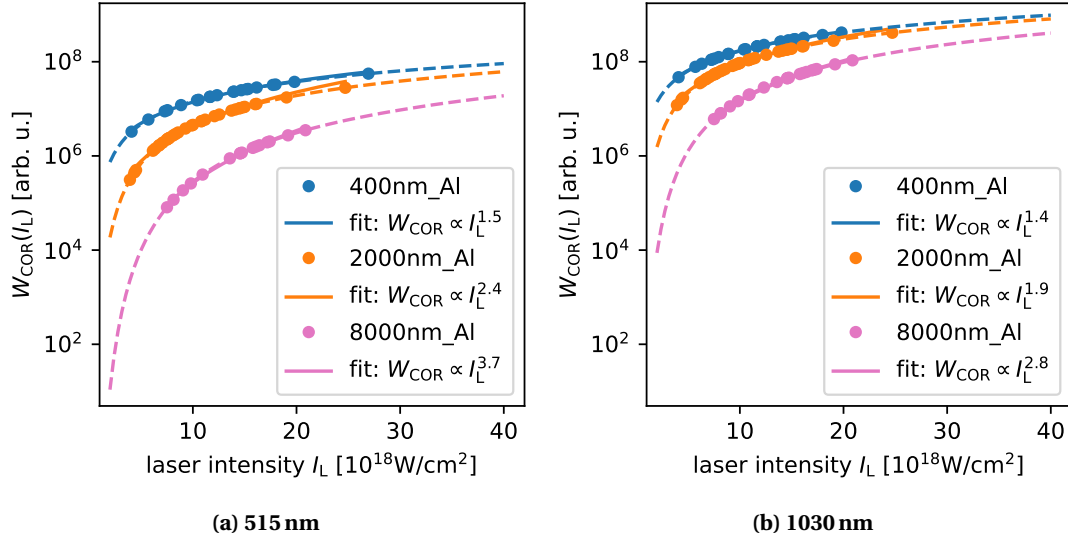


Figure 4.5.: The calculated COR energy W_{COR} as a function of laser intensity for different target thicknesses and two different radiation wavelengths (as specified in the heading of each subfigure). Details about the CTR model which has been used for this calculation are given in the text (paragraph Model Parameters on page 53). W_{COR} has been calculated for the single intensity values of the measured laser shots (see Fig. 4.4) and plotted as dots. In analogy to Fig. 4.4, the function $W_{\text{fit}} = G \cdot I_L^{\Xi}$ with the parameters G and Ξ has been fitted to the calculated $W_{\text{COR}}(I_L)$ data points as specified in the legend. Moreover, W_{COR} has also been calculated for a larger intensity range (dashed lines).

make the fits to the experimental and the calculated data comparable, the fitted W_{COR} data points have been calculated for the exact same laser intensities for which the emitted COR was measured in the experiment. A comparison of the exponent Ξ of the function $W_{\text{fit}} = G \cdot I_L^{\Xi}$ fitted to the experimental data in Fig. 4.4 and to the calculated data in Fig. 4.5 can be seen in table 4.1. Table 4.1 illustrates that the experimental data (Exp.) scale significantly stronger with laser intensity I_L (i.e. a larger exponent Ξ) than the calculated COR (Sim.). There might be several possible reasons to explain this systematic difference between experiment and calculation. It is, for instance, quite likely that the simplified CTR model is not a sufficient accurate description of the physical processes which took place in the experiment. Another plausible explanation is that the calculated intensity on target has been probably overestimated in the experiment. To illustrate this, W_{COR} has been calculated from the CTR model for intensity values which have been reduced by 40 % as compared to the laser intensity calculated in the experiment. Polynomials with a variable exponent Ξ are fitted to these data points similar to what was done in Fig. 4.5 but now with a 40 % lower laser intensity ($0.6 \cdot I_L$). The exponents Ξ of the converged fits are given in table 4.1 and show a much better overlap with the exponents of the fits to the experimental data (Exp.) if the laser intensity has been reduced by 40 % in the calculations.

d_0	fit to $W_{\text{COR}}(\omega_L)$			fit to $W_{\text{COR}}(2\omega_L)$		
	$\Xi(\text{Exp.})$	$\Xi(\text{Sim.})$	Ξ (Sim. for $0.6 \cdot I_L$)	$\Xi(\text{Exp.})$	$\Xi(\text{Sim.})$	Ξ (Sim. for $0.6 \cdot I_L$)
400 nm	2.4 ± 0.3	1.4	1.5	2.1 ± 0.3	1.5	1.7
2 μm	2.5 ± 0.3	1.9	2.3	3.0 ± 0.3	2.4	3.0
8 μm	4.2 ± 0.7	2.8	3.5	3.9 ± 0.7	3.7	4.7

Table 4.1.: Exponent Ξ of the function $W_{\text{fit}} = G \cdot I_L^\Xi$ which has been fitted to the scaling of the COR energy W_{COR} with laser intensity I_L at ω_L and $2\omega_L$ for different target thicknesses d_0 . The exponent Ξ has been obtained from the fits to the experimental data in Fig. 4.4 (Exp.), from fits to the calculated data in Fig. 4.5 (Sim.) and from CTR calculations and fits where the laser intensity I_L of the considered data points was reduced by 40 % as compared to Fig. 4.5 (Sim. for $0.6 \cdot I_L$).

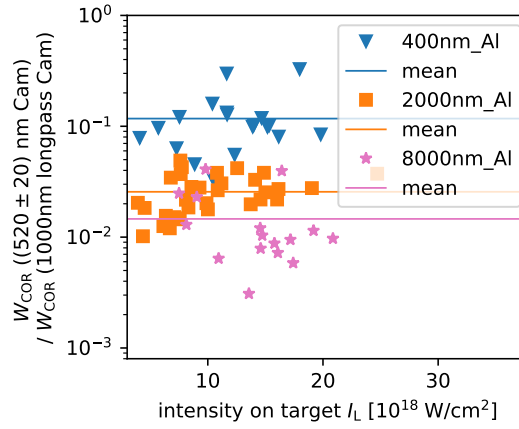


Figure 4.6.: The ratio of total COR energy W_{COR} emitted per laser shot for radiation measured around 515 nm (by (520 ± 20) nm camera) and radiation measured around 1030 nm (by 1000 nm longpass camera). Every data point has been calculated from the total pixel count, which is proportional to W_{COR} , of the COR images acquired for this particular laser shot on experiment day #1. The COR energy W_{COR} is plotted for the different investigated target thicknesses and the mean energy ratio is plotted as a line for every target thickness.

4.2.2. Energy Ratio of COR Emitted at 515 nm to COR Emitted at 1030 nm

Until now, the scaling of COR energy W_{COR} has been investigated separately for COR at 515 nm and at 1030 nm. Therefore, the ratio $W_{\text{COR}}(515 \text{ nm})/W_{\text{COR}}(1030 \text{ nm})$ of COR energy at different wavelengths is investigated in the following. This energy ratio has been calculated for every laser shot and is plotted in Fig. 4.6 as a function of laser intensity. Except for a few outliers, the energy ratio $W_{\text{COR}}((520 \pm 20) \text{ nm Cam})/W_{\text{COR}}(1000 \text{ nm longpass Cam})$ differs significantly for the different target thicknesses as shown in Fig. 4.6. For the investigated target thicknesses, there is no reason to assume that the electron heating differs with target thickness as long as the laser parameters are similar. Hence, Fig. 4.6 confirms the trend seen in the calculations of the last subsection. The thicker the target, the more expanded are the electron bunches in the propagation direction due to the velocity dispersion. Accordingly, the coherence of the radiation emitted by those electron bunches is reduced. Moreover, the coherence reduction has a stronger influence on radiation at 515 nm than on radiation at

1030 nm. Therefore, the energy ratio $W_{\text{COR}}(515\text{ nm})/W_{\text{COR}}(1030\text{ nm})$ is reduced for thicker targets as confirmed by Fig. 4.6.

4.3. Scaling of COR Energy with Target Thickness

So far, the data for different target thicknesses is plotted as different batches in Fig. 4.3 to Fig. 4.6. However, it is also quite instructive to use the target thickness as the horizontal plot axis. This, however, requires to evaluate the COR energy W_{COR} at a fixed laser intensity. To do so, the functions fitted in Fig. 4.4 (and Fig. E.3) have been evaluated at $I_L = 10^{19} \text{ W/cm}^2$. The consequent scaling of the COR energy W_{COR} with target thickness d_0 is plotted in Fig. 4.7. Evaluating the dependence of the COR energy W_{COR} on the target thickness d_0 , as depicted in Fig. 4.7, allows to illustrate the decrease of W_{COR} with increasing d_0 , due to coherence reduction caused by velocity dispersion. Moreover, it can be seen in Fig. 4.7 that the decrease of W_{COR} with d_0 is stronger for shorter radiation wavelengths, as discussed in detail in section 4.2.

The enhanced ion energies for thin targets in laser-driven ion acceleration [115] and the large CTR emission region [75] has been explained by recirculating electrons. Hence, the recirculation of hot electrons might also influence the scaling of W_{COR} with target thickness d_0 . For a conclusive discussion, the recirculation of hot electrons should therefore be taken into account in a model of the COR emission by hot electron bunches. For simplicity, however, recirculating hot electrons are neglected in the following.

Inspired by [67, 68, 70], the CTR model has been used to fit the scaling of the CTR energy W_{COR} , measured at the laser frequency and at the second harmonic, with target thickness. In contrast to [67, 68, 70], the COR energy was measured simultaneously at the laser frequency and the second harmonic in the experiments of this thesis. In that way, not only the hot electron temperature T_h but also the ratio P_1/P_2 of the charge per bunch of electrons accelerated at ω_L and at $2\omega_L$ can be obtained from the CTR model fit.

CTR Model Details The same CTR model (introduced in section 2.5.3.1) as applied in section 4.2.1 has been used to approximate the COR energy $W_{\text{COR}}(d_0)$ scaling with target thickness d_0 . To do so, the experimental data points in Fig. 4.7 have been fitted by Eq. 2.41 after integrating Eq. 2.41 over \vec{r}_\perp . The CTR model parameters, as specified in the following, are introduced and defined in section 2.5.3.1 and illustrated in Fig. 2.5. In accordance with the experimental setup (see Fig. 3.1 and Fig. 2.2), $\theta = 37^\circ$ has been chosen and the radiating hot electron current has been assumed to be directed normal ($\psi = 0$) to the target rear surface. To simultaneously fit $W_{\text{COR}}(d_0)$ in Fig. 4.7 for the two considered wavelengths 515 nm and 1030 nm, the parameter P_1/P_2 (see Eq. 2.43) and T_h of the CTR model have been employed as fit parameters. Moreover, $\sigma_t = \mathcal{T}_L/(10 \cdot \sqrt{2}) = 0.243 \text{ fs}$ (as proposed in [70] based on PIC results and fits to experimental data) and $a = 1/4 v_L$ (based on results in [70]) have been assumed to limit the number of fit parameters. As $W_{\text{COR}}(d_0)$ does not depend on the number of electron bunches n_b for a fixed laser intensity, $n_b = 20$ has been used.

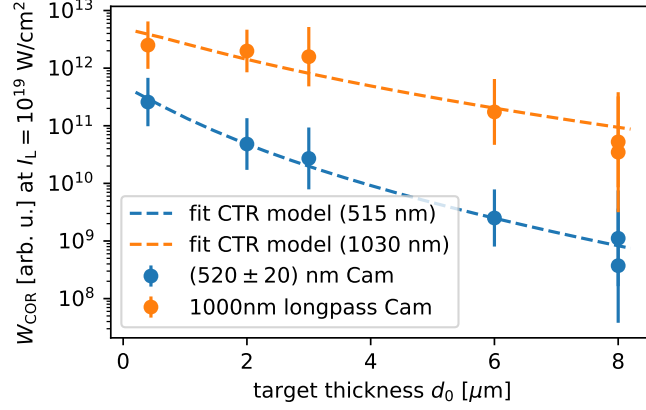


Figure 4.7.: The COR energy W_{COR} emitted at the laser intensity $I_L = 10^{19} \text{ W/cm}^2$ as a function of target thickness for COR at 515 nm and at 1030 nm. The data points have been obtained from evaluating the functions fitted in Fig. 4.4 (and Fig. E.3) at the intensity $I_L = 10^{19} \text{ W/cm}^2$. The errorbars have been calculated from the variance of the fit parameters in Fig. 4.4 (and Fig. E.3) using propagation of error. In that way, the variation of the experimental data is taken into account. For a meaningful plot, more data points are desirable. Therefore, the data from experiment day #1 and #2 is shown in this plot. Moreover, the CTR model, as introduced in section 2.5.3.1, has been fitted (least squares fit) to $\log_{10}(W_{\text{COR}}(d_0))$ simultaneously for the data points from the $(520 \pm 20) \text{ nm}$ camera and the 1000 nm longpass camera. The fit converged for $P_1/P_2 \approx 1.41 \pm 0.06$ and $T_h \approx (292 \pm 22) \text{ keV}$. The COR energy has been calculated for the converged fit parameters and is plotted as two dashed lines. Details on the fit and the model parameters can be found in paragraph CTR Model Details on page 56.

4.3.1. Results of the CTR Model Fit

The fit presented in Fig. 4.7 converged for $P_1/P_2 \approx 1.41 \pm 0.06$ and $T_h \approx (292 \pm 22) \text{ keV}$. If not stated differently, all errors reported throughout this thesis correspond to one standard deviation (here obtained from the least squared fit). The fit in Fig. 4.7 is in good accordance with the experimental data. This might be a little bit surprising as data from two experiment days, which are only to a certain degree comparable, are plotted and fitted in Fig. 4.7. Using only the data from experiment day #1, to fit the CTR model to, results in similar parameters ($P_1/P_2 \approx 1.41 \pm 0.09$ and $T_h \approx (279 \pm 41) \text{ keV}$). Hence, W_{COR} (i.e. the total pixel count of a calibrated COR image) is a robust measure which is unaffected by spatial changes in the COR images as discussed in section 4.1.2. Furthermore, it can be assumed that these general parameters (i.e. P_1/P_2 and T_h) of the target heating at the front surface remain the same, despite the day-to-day laser pulse differences in the POLARIS laser system. The fit result $T_h \approx (292 \pm 22) \text{ keV}$ lies systematically below the hot electron temperature of 400 keV which has been estimated from Eq. 2.13 for a laser intensity of 10^{19} W/cm^2 . This systematic difference might be due to an energy loss of the hot electrons in the target (e.g. bremsstrahlung) or to deceleration in the electric sheath field at the target rear surface. Another explanation is provided by the discussion in section 4.2.1: The comparison between the measured (see Fig. 4.4) and calculated (see Fig. 4.5) scaling of the COR energy W_{COR} with laser intensity indicates that the actual laser intensity in the experiment was roughly 40 % smaller than the calculated laser intensity I_L . Applying this finding to the current discussion, the hot electron temperature estimated from Eq. 2.13 for $I_L = 6 \times 10^{18} \text{ W/cm}^2$ is 314 keV. Hence, the hot

electron temperature determined from Fig. 4.7 would be in good agreement with the hot electron temperature estimated from the Kluge scaling (Eq. 2.13) if the actual laser intensity in the experiment was 40 % smaller than the calculated laser intensity.

In [67, 70], a similar experimental setup was used where the high-intensity laser was focused at normal incidence on the Al foil target. In contrast to this thesis, the COR was collected by an off-axis parabola and coupled into a spectrometer to measure W_{COR} via integration of the spectrum. Despite the similar laser intensity in [67, 70], they obtained a hot electron temperature of 2 MeV for $I_L = 2 \times 10^{19} \text{ W/cm}^2$ [70] and $I_L = 3 \times 10^{19} \text{ W/cm}^2$ [67]. There are several reasons which might explain the difference between the hot electron temperature determined in [67, 70] and the result of this thesis ($T_h \approx (292 \pm 22) \text{ keV}$): The much larger T_h in [67, 70] could be due to differences in the target heating at the front surface of the Al foil. Moreover, also differences in the propagation of the hot electrons through the target might explain the lower T_h in this thesis as compared to [67, 70]. In [67, 70], much thicker Al targets (between 20 μm and 900 μm thick) have been investigated. Therefore, the experiments of this thesis should be extended to much thicker targets for a better comparability to [67, 70].

The second fit parameter P_1/P_2 provides an estimation of the temporal composition of the hot electron current. Namely, $P_1/P_2 \approx 1.41 \pm 0.06$ corresponds to an electron current where $(41 \pm 1) \%$ of the hot electrons have been accelerated at ω_L ¹ and $(59 \pm 1) \%$ of the hot electrons have been accelerated at $2\omega_L$ ². This is in very good agreement with the experimental results of H. POPESCU *et al.* [70]. In [70], the intensity of the second harmonic is compared to the fourth harmonic in the COR spectrum to determine P_1/P_2 . In the present situation of normal laser incidence, one would expect relativistic $\vec{j} \times \vec{B}$ heating (see page 9) to dominate the laser absorption. Hence, one would expect mainly hot electron bunches produced at $2\omega_L$. However, because $(41 \pm 1) \%$ of the hot electrons were accelerated at ω_L in our experiment, it can be concluded that hole boring [99] played a significant role in the presented experiments and therefore also resonance absorption (or vacuum heating) contributed to the electron heating at the target front surface significantly.

4.3.1.1. Influence of the CTR Model Parameter on the Fit

To validate the CTR model fit results presented above, the influence of the fit parameters is briefly discussed. P_1/P_2 , namely the ratio of electrons per bunch accelerated at ω_L and $2\omega_L$, mainly influences the difference in W_{COR} between COR at 515 nm and at 1030 nm. The hot electron temperature T_h mainly governs the decrease in W_{COR} with increasing target thickness d_0 . For the fit in Fig. 4.7, the temporal width σ_t of the electron bunches as well as the temporal shift a between electron bunches produced at ω_L and electron bunches produced at $2\omega_L$ have been kept constant (paragraph CTR Model Details on page 56) to reduced the

¹Hot electrons accelerated at ω_L correspond to hot electron bunches which are separated by one optical laser cycle $\mathcal{T}_L = 2\pi/\omega_L$ in time.

²Hot electrons accelerated at $2\omega_L$ corresponds to hot electron bunches which are separated by half an optical laser cycle $\mathcal{T}_L/2 = 2\pi/2\omega_L$ in time.

number of fit parameter based on the results in [70]. As the justification of this decision might seem questionable, it is discussed in closer detail in the following.

The parameter a influences the energy ratio $W_{\text{COR}}(515\text{nm})/W_{\text{COR}}(1030\text{nm})$ ¹. For instance, for $a \sim 0$ and $a \sim 1/2v_L = \mathcal{T}_L/2$, the energy $W_{\text{COR}}(515\text{nm})$ is enhanced with respect to COR at the central laser frequency. As discussed in section 2.5.3.1, the temporal width σ_t of the electron bunches determines (together with T_h) the decrease in $W_{\text{COR}}(\lambda)$ with decreasing wavelength λ . Hence, σ_t also influences the energy ratio $W_{\text{COR}}(515\text{nm})/W_{\text{COR}}(1030\text{nm})$. To discuss the influence of the (currently fixed) parameters a and σ_t on the CTR model fit results, a parameter scan has been performed for a and σ_t . For each parameter combination of a and σ_t , the CTR model (details in paragraph CTR Model Details on page 56) has been fitted to the experimental data points in Fig. 4.7. The fit parameter P_1/P_2 and T_h of the converged fits are shown in Fig. 4.8.

Looking at Fig. 4.8a, it becomes clear that only a temporal shift a between $0.15\mathcal{T}_L$ and $0.35\mathcal{T}_L$ results in reasonable values for P_1/P_2 . At normal incidence it is expected that $\vec{j} \times \vec{B}$ heating dominates the laser absorption at the target front surface. Therefore, P_1 is assumed to be relatively small. This is the case for $a = 0.25\mathcal{T}_L$ where P_1/P_2 is minimal in Fig. 4.8a. Furthermore, the fit parameter T_h approaches a maximum in Fig. 4.8b for $a \rightarrow 0.25\mathcal{T}_L$ which is an indication for a well converging fit.

In comparison, the influence of σ_t on the converged fit parameters T_h and P_1/P_2 is relatively weak. For $a/\mathcal{T}_L = 0.25$ (which is a reasonable choice as discussed in the last paragraph), the fit parameter T_h does not change with σ_t and the fitted P_1/P_2 decreases only by 16 % from $\sigma_t = 220$ as to $\sigma_t = 390$ as. Hence, as long as the temporal shift a is kept inside of reasonable limits (i.e. between $0.15\mathcal{T}_L$ and $0.35\mathcal{T}_L$), the influence of the bunch duration σ_t on the converged fit parameters is relatively low, as seen in Fig. 4.8. Nevertheless, Fig. 4.8 shows that the parameters a and σ_t influence the result of the CTR model fit in Fig. 4.7. In a new fit procedure, the COR model with P_1/P_2 , T_h , a and σ_t as fit parameters has been fitted to the experimental data in Fig. 4.7. Using these four fit parameters, the fit converged to $P_1/P_2 \approx 1.34$, $T_h \approx 292\text{keV}$, $a/\mathcal{T}_L \approx 0.25 \pm 0.06$ and $\sigma_t \approx (301 \pm 76)$ as. The obtained fit parameters for the converged fit are in good agreement with the fit where only P_1/P_2 and T_h have been used as fit parameters (see Fig. 4.7). The converged fit parameters $a/\mathcal{T}_L \approx 0.25 \pm 0.06$ and $\sigma_t \approx (301 \pm 76)$ as are also in very good agreement with the results of H. POPESCU *et al.* [70]. Moreover, the minimized difference between the fit function and the logarithmized experimental data ($\log_{10}(W_{\text{COR}}(d_0, \lambda))$) is the same in both cases, no matter if a and σ_t have been used as additional fit parameters or not. Hence, it can be concluded that the assumption of $\sigma_t = \mathcal{T}_L/(10 \cdot \sqrt{2}) = 243$ as (as proposed in [70] based on PIC results and fits to experimental data) and $a = \mathcal{T}_L/4$ (based on results in [70]) for the fit in Fig. 4.7 was reasonable.

¹Moreover, the parameter a also influences the envelope of the CTR spectrum between the harmonics (of the central laser frequency). However, this is not of particular interest to the current discussion.

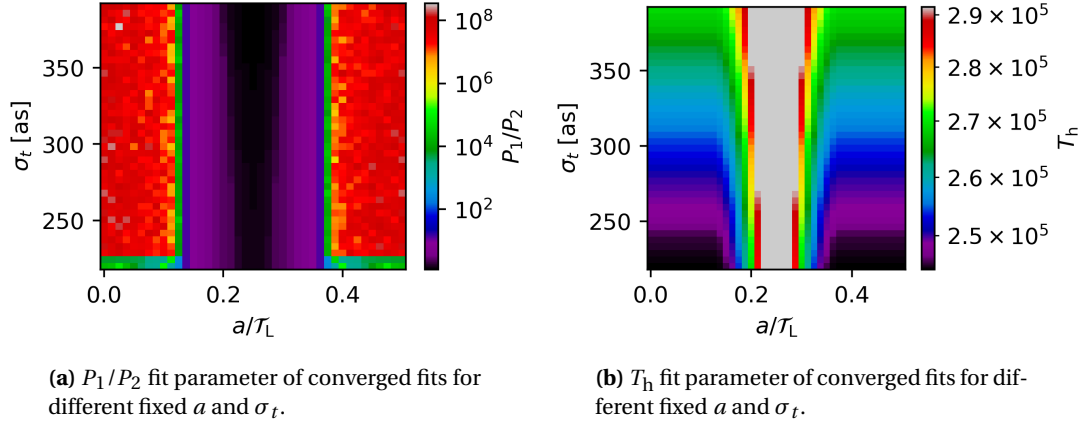


Figure 4.8.: Parameter scan of the CTR model parameters a and σ_t . Shown are the converged fit parameters P_1/P_2 (subplot (a)) and T_h (subplot (b)) for different parameter combinations of a and σ_t . Every grid point corresponds to a fit of the CTR model to the experimental data in Fig. 4.7. The parameters a and σ_t have been chosen according to the current grid position and have been kept fixed during the fit. The range of considered values for σ_t (i.e. the y-axis limits in the plots) has been chosen according to typical values obtained in PIC simulations [70].

4.3.2. Variations of the Hot Electron Temperature and the Laser Absorption with Laser Intensity

So far in this section, the COR energy $W_{\text{COR}}(d_0)$ has only been evaluated as a function of target thickness d_0 at a fixed intensity of $I_L = 10^{19} \text{ W/cm}^2$ to determine the hot electron temperature T_h and the relative amount of electrons accelerated at ω_L and at $2\omega_L$. Now, the fit procedure which has been applied to obtain Fig. 4.7 is repeatedly applied for different laser intensities to investigate the scaling of the fit parameters T_h and P_1/P_2 with laser intensity. Therefore, the fitted functions in Fig. 4.4 and Fig. E.3 have been evaluated at different laser intensities I_L to obtain $W_{\text{COR}}(d_0, \lambda, I_L)$. For every considered laser intensity value I_L in the experimentally investigated range, the COR model has been fitted to $W_{\text{COR}}(d_0, \lambda)$ as described on page 56. The converged fit parameters are plotted in Fig. 4.9 as a function of I_L .

Fig. 4.9a shows that the hot electron temperature T_h , obtained from fits of the CTR model to the experimental data, significantly increases towards higher laser intensities I_L . However, the T_h obtained from fits to the measured W_{COR} exhibits a lower scaling than the one predicted by the model of T. KLUGE *et al.* [113] which is valid for normal laser incidence as present in the experimental setup of this thesis (see Fig. 3.1). There are several reasons which might explain the difference between theory and experiment. The plasma heating at the target front surface was, for instance, maybe less effective than expected. It could also be that the electrons were slowed down in the target by self-generated electric fields or scattering. However, another possibility is that the CTR model, which is used to fit the experimental data and determine T_h , does not provide an accurate description of the COR observed in the experiment. The assumption of a relativistic Maxwellian (Jüttner) momentum distribution ([153] and references therein) might not fit to the actual momentum distribution of the hot electrons accelerated by the laser in the experiment. To examine this hypothesis, PIC simulations should be used.

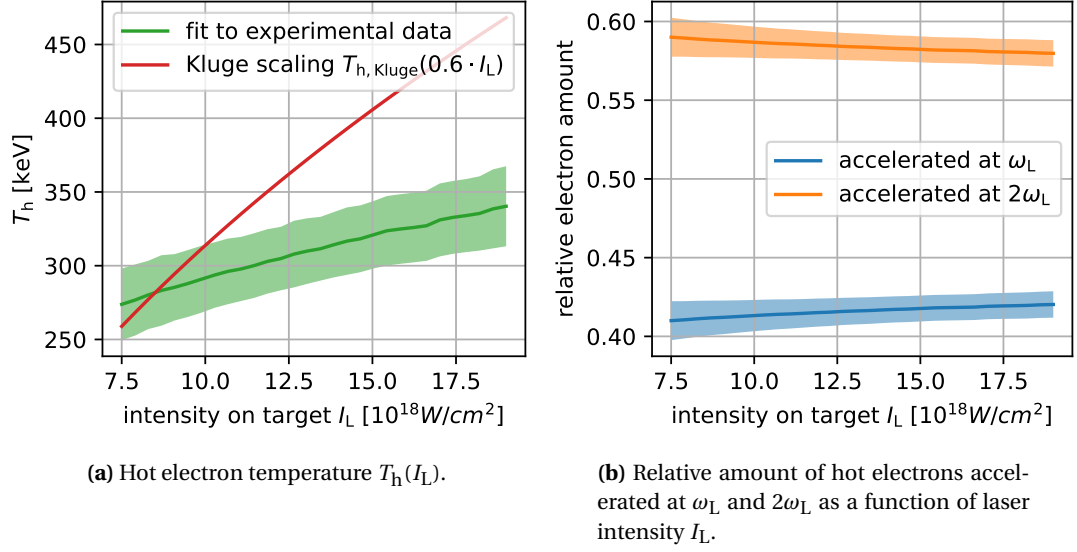


Figure 4.9.: The hot electron temperature T_h (a) and the relative amount of hot electrons accelerated at ω_L and $2\omega_L$ (b) as a function of laser intensity I_L . As done for Fig. 4.7, the CTR model (introduced in section 2.5.3.1) has been fitted to $\log_{10}(W_{\text{COR}}(d_0))$ simultaneously for the data points from the (520 ± 20) nm camera and the 1000 nm longpass camera. However, now this fit has been performed for different laser intensities I_L by evaluating the fitted functions in Fig. 4.4 and Fig. E.3 at different I_L . The converged fit parameters from these fits are plotted in (a) and (b). The standard deviation (i.e. the error) of the fit parameters is used to obtain the error of the plotted electron temperature T_h and the plotted relative amount of hot electrons accelerated at ω_L and $2\omega_L$. This error is depicted as a half-transparent region around the data points in (a) and (b). For comparison, the scaling of hot electron temperature with laser intensity as estimated from the Kluge model [113] (Eq. 2.13) is plotted as a red line alongside the experimentally determined hot electron temperature scaling (green line) in (a). As discussed in section 4.2.1 and section 4.3.1, the actual laser intensity on target was probably 40 % lower than the calculated laser intensity I_L . Therefore, the theoretical hot electron temperature was calculated with the Kluge model for a 40 % lower laser intensity.

In Fig. 4.9b, the scaling of the relative amount of hot electrons accelerated at ω_L and at $2\omega_L$ with I_L is plotted. Whereas the relative amount of electrons accelerated at ω_L ($2\omega_L$) slightly increases (decreases) with laser intensity, this change is not significant because the change is smaller than the error of the relative electron amount (plotted as a half-transparent region). Hence, the comparable amount of electrons accelerated at ω_L and at $2\omega_L$ indicates that the influence of the different absorption processes ($\vec{j} \times \vec{B}$ heating and resonance absorption) is expected to be the same and their interplay is kept constant over the investigated intensity range.

To investigate the scaling of laser absorption at the target front side with I_L in closer detail, more experimental data points would be beneficial to counteract the large variance of the experimental data in Fig. 4.4 and Fig. E.3. Furthermore, a larger range of investigated laser intensities I_L would be desirable to explore in future experiments.

4.4. Polarization Characteristics of COR

The last two sections dealt with changes in the measured COR due to effects related to the coherence of the hot electron current which depends on its temporal structure and its energy. Hence, the type of radiation, namely TR or SR, was less important in the last two sections and the coherence effects have been approximately described by the CTR model (see section 2.5.3.1) which qualitatively also models the coherence effects in SR. Nevertheless, for an exhaustive picture of rear surface COR in high-intensity laser-solid experiments it is desired to resolve if rather SR or TR was the dominating emission process in the experiment. Inspired by C. BELLEI *et al.* [75], the polarization of the COR radiation at the second harmonic (515 nm) was therefore measured. In comparison with calculations, such a polarization resolved measurement can be used to distinguish between TR and SR. Furthermore, the influence of the laser intensity and the COR's source size on the polarization of the measured COR is investigated in the following.

4.4.1. Experimental Results

As described in section 3.3.2, a Wollaston prism was used to split the COR according to its polarization into two images on camera 1 (see Fig. 3.1). One image corresponds to the COR polarized parallel (P-polarization) to the radiation plane whereas the other image contains the COR which is polarized perpendicular (S-polarization) to the radiation plane. The radiation plane is formed by the direction of observation ($\theta = 37^\circ$ and $\alpha = 90^\circ$ as defined in Fig. 2.2) and the target rear surface normal. In the present situation, the radiation plane is parallel to the optical table. The two COR images, one for each polarization axis, have been overlapped to show spatial changes in the polarization of the imaged rear surface COR emission spot, as depicted in Fig. 4.1.

In the last sections, the total energy W_{COR} of the emitted COR in a specific spectral range has proven to be a robust measure of COR. The spatial cameras were used to measure W_{COR} in the spectral regime determined by the spectral filters in front of the cameras as W_{COR} is proportional to the total pixel count of the camera. To illustrate the polarization characteristics of the emitted COR, the ratio of S-polarized (perpendicular to optical table) COR radiation energy to P-polarized (parallel to optical table) COR energy at the second harmonic is plotted as a function of intensity in Fig. 4.10a for different target thicknesses. This energy ratio (i.e. $W_{\text{COR}}(|E_S|^2)/W_{\text{COR}}(|E_P|^2)$) is called polarization ratio in the following. Furthermore, the polarization ratio is plotted as a function of the area ratio, namely the COR area $\mathcal{A}_{\text{FWHM}}$ extracted from the (520 ± 20) nm camera divided by the COR area $\mathcal{A}_{\text{FWHM}}$ extracted from the 900–1000 nm camera, in Fig. 4.10b.

Due to the large variance of the data points plotted in Fig. 4.10, it is difficult to draw a conclusion about the scaling of the polarization ratio with laser intensity I_L or area fraction $\mathcal{A}_{\text{FWHM}}((520 \pm 20) \text{ nm})/\mathcal{A}_{\text{FWHM}}(900\text{--}1000 \text{ nm})$. As before, a higher number of data points would be beneficial in this situation. However, for the 400 nm and the 2 μm thick target, a slight increase in the polarization ratio with laser intensity is visible in Fig. 4.10a. Furthermore, the polarization ratio differs significantly for the different target thicknesses. Whereas

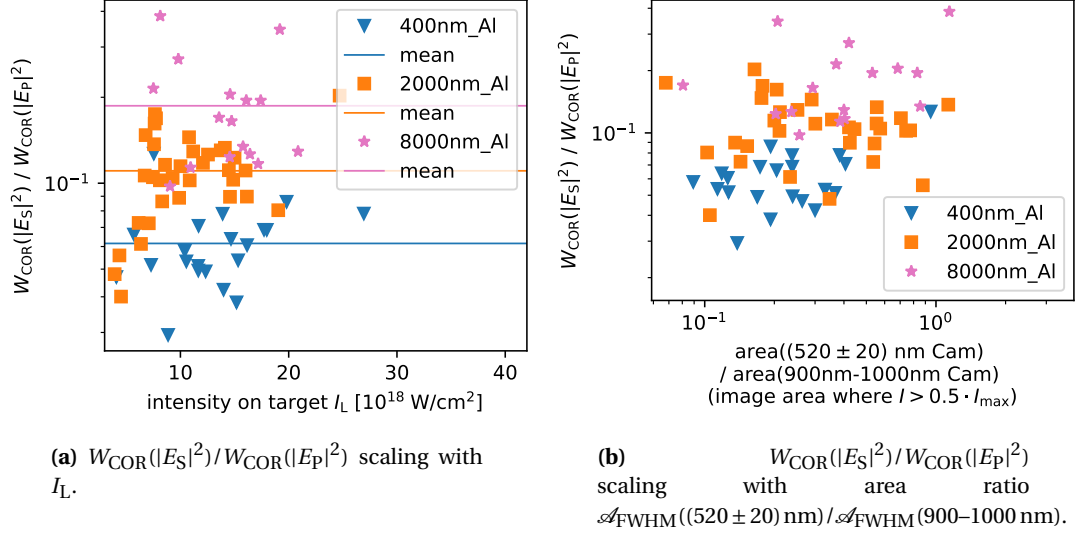


Figure 4.10.: Ratio of S-polarized (perpendicular to optical table) COR radiation energy at $(520 \pm 20) \text{ nm}$ to P-polarized (parallel to optical table) COR radiation energy at $(520 \pm 20) \text{ nm}$ as a function of laser intensity I_L (a) and as a function of the area ratio $\mathcal{A}_{\text{FWHM}}((520 \pm 20) \text{ nm})/\mathcal{A}_{\text{FWHM}}(900-1000 \text{ nm})$ (b). The optical table is parallel to the yz-plane in Fig. 2.2. The polarization ratio $W_{\text{COR}}(|E_S|^2)/W_{\text{COR}}(|E_P|^2)$ is plotted for different target thicknesses. Every data point has been calculated from the total pixel count, which is proportional to W_{COR} , of the polarization resolved COR images acquired with the $(520 \pm 20) \text{ nm}$ camera for this particular laser shot on experiment day #1. Additionally, the mean value of the polarization ratio is plotted as a horizontal line in (a). The COR's emission spot area on the $(520 \pm 20) \text{ nm}$ and the 900–1000 nm camera has been determined by multiplying the calibrated area of a single pixel with the number of pixels where $I > I_{\text{max}}/2$ is fulfilled for every laser shot.

the imaged COR emission spot is mainly P-polarized, the relative amount of S-polarized COR increases with increasing target thickness. This is additionally illustrated by the mean values of the polarization ratio which are plotted for each investigated target thickness as a horizontal line in Fig. 4.10a.

In section 4.1.2.1, the area $\mathcal{A}_{\text{FWHM}}$ of the COR emission spot imaged onto the $(520 \pm 20) \text{ nm}$ camera was compared to the area $\mathcal{A}_{\text{FWHM}}$ of the COR emission spot imaged onto the 900–1000 nm camera. In the range from 0.27 to 1, this area ratio is expected to be proportional to the actual area of the COR emission spot, as described in section 4.1.2.1. Looking at Fig. 4.10b, it can therefore be concluded that the polarization ratio of COR increases with increasing size of the COR emission spot which is closely related to the diameter of the hot electron beam at the target rear surface.

The polarization of the imaged rear surface COR emission spot is influenced by the spatial and angular distribution as well as the energy of the hot electron current as calculations indicate (see appendix D). Hence, there is no straightforward explanation for the change in COR polarization with target thickness, laser intensity and the COR's source size. Instead, detailed simulations with an accurate COR model are needed to understand the measured COR polarization depicted in Fig. 4.10. To demonstrate this, a simple model of the COR emitted by a diverging hot electron current is proposed in section D.1, based on the model introduced in section 2.5. Calculations using this simple model (see section D.2) indicate,

for example, that TR is a less likely explanation of the experimentally observed COR polarization characteristics and therefore SR was most likely the dominating emission process in the experiments of this thesis. Moreover, the simple COR model shows a similar change in the polarization ratio with laser intensity and target thickness. The results of the simple COR model are discussed in more detail in section D.2. A more accurate and detailed COR model would be beneficial for a conclusive discussion. However, the simplified model is already very valuable as it not only demonstrates the opportunities and capabilities that COR simulations provide to interpret the experimental results but also reproduces the general trends observed in the experiments.

5. Conclusion

Energetic electrons, accelerated in the focus of a high-intensity laser at the surface of a solid, are of primary importance to applications like laser-driven ion acceleration [14–18] and Fast Ignition (FI) in Inertial Confinement Fusion (ICF) [49–51]. Here, the hot electrons either set up the electric field for ion acceleration or transport energy to provide the "spark" which ignites fusion. The success of these applications requires a better understanding of hot electron transport through dense matter.

In the present thesis, such hot electron transport has been studied by focusing an ultra-short, high-intensity laser pulse onto thin aluminum foil targets (between $0.4\text{ }\mu\text{m}$ and $8\text{ }\mu\text{m}$ thick) at normal incidence where intensities up to $3 \times 10^{19}\text{ W/cm}^2$ have been reached. The hot electrons emit COR (probably transition radiation or synchrotron radiation) at the target rear surface. The rear surface COR emission spot has been imaged at an angle of 37° onto three cameras. Spectral filters were placed in front of the cameras to investigate COR at the central laser frequency ($\lambda = 1030\text{ nm}$), the second harmonic ($\lambda = 515\text{ nm}$) and in between ($\lambda = 900\text{--}1000\text{ nm}$). Additionally, a Wollaston prism was used to measure the polarization of the COR at the second harmonic.

First, the spatial intensity distribution of COR has been analyzed for a selection of exemplary COR camera images. The COR's source size mostly ranged between $1.2\text{ }\mu\text{m}$ and $2.3\text{ }\mu\text{m}$ in the experiments and increased with increasing target thickness. The determined COR's source sizes are less than half the size of the laser focal spot which suggests that pinching and filamentation have influenced the hot electron beam during its propagation. The increase in COR emission spot size with target thickness is an indication of a diverging hot electron current. Further experiments might profit from imaging at shorter wavelengths to improve the spatial resolution. Additionally, investigating thicker targets is needed to acquire a broader picture of hot electron current pinching, filamentation and divergence.

The total emitted COR energy in the different spectral regions has been used as a robust measure to investigate changes in the emitted COR with target thickness and laser intensity. The total emitted COR energy increases strongly with increasing laser intensity and is proportional to I_L^Ξ , with the laser intensity I_L on target and the exponent Ξ ranging from 2 to 4. In particular for thicker targets, the COR energy shows a stronger scaling with laser intensity. For a better understanding, a simple coherent transition radiation (CTR) model, inspired by [70, 144], has been considered. Using this model, the CTR emitted by a laminar beam of periodically spaced bunches of hot electrons with a relativistic Maxwellian (Jüttner) momentum distribution has been calculated. These CTR calculations hold qualitatively also true for coherent synchrotron radiation (CSR). Considering a hot electron number and temperature increase with laser intensity, the CTR model calculations explain the experimental

observations. Moreover, the CTR calculations suggest that the actual laser intensity on target was probably 40 % lower than the value calculated from the measured laser parameters (pulse energy, pulse duration and focal spot size). In the investigated intensity regime, the measured COR energy is mainly influenced by the coherence of the radiation emitted by a hot electron bunch. The longer the electron bunch with respect to the COR wavelength, the lower is the coherence of the radiation emitted by this bunch. In fact, due to the energy distribution in an electron bunch, the longitudinal length of the bunch increases with propagation distance.

The above mentioned CTR model has been used to fit the experimentally measured COR energy at the central laser frequency (1030 nm) and the second harmonic (515 nm) as a function of target thickness. From such fits, the hot electron temperature T_h and the relative number of electrons accelerated at the laser frequency ω_L and at $2\omega_L$ could be determined as a function of laser intensity I_L . As expected, the hot electron temperature T_h increases with I_L . However, the temperature increase was lower than the scaling suggested by the model of T. KLUGE *et al.* [113]. The relative number of hot electrons accelerated at ω_L and at $2\omega_L$ contains information on the present electron heating mechanisms at the target front surface and their relative influence. At a laser intensity of 10^{19} W/cm², the CTR model fits indicate that (41 ± 1) % of the hot electrons have been accelerated at ω_L and (59 ± 1) % at $2\omega_L$, which is in very good agreement with previous experiments [70]. For our experimental conditions, with a laser incidence angle of 90° (i.e. normal incidence), a substantial amount of hole boring must therefore have been present at the target front surface to result in hot electron bunches being produced at ω_L . However, the experiments show no significant change of the relative amount of electrons accelerated at ω_L and at $2\omega_L$ with laser intensity. To the best of the author's knowledge, there is no other study which uses CTR model fits to investigate the scaling of T_h and of the relative amount of electrons accelerated at ω_L and $2\omega_L$ with laser intensity.

The general spatial structure of the COR polarization at the second harmonic exhibits strong changes across the COR emission region which suggest that CSR was the dominating COR emission process. Calculations with a simple COR model also point towards CSR to explain the measured COR polarization. In a more systematic investigation of COR at the second harmonic, an increase in the relative amount of S-polarized¹ COR with laser intensity (and hence hot electron temperature), target thickness and the COR's source size at the target rear surface has been detected.

In conclusion, the source size, the energy and the polarization of rear surface COR have been experimentally investigated as a function of laser intensity I_L and target thickness d_0 to study hot electron generation and transport in high-intensity laser-solid interaction. Future experiments should profit from acquiring more data for a larger range of I_L and d_0 . Moreover, rear surface COR could be used in future experiments to study the influence of target material and laser incidence angle on hot electron generation and transport.

¹S-polarized refers to radiation polarized perpendicular to the optical table. The optical table is parallel to the plane formed by the target rear surface normal and the observation direction (optical axis of microscope objective used for imaging).

Bibliography

- [1] Wolfgang ZINTH and Ursula ZINTH. *Optik*. 5th ed. De Gruyter, 2018.
- [2] Max BORN and Emil WOLF. *Principles of Optics*. 7th ed. Cambridge University Press, 2019.
- [3] Albert EINSTEIN. “Strahlungs-emission und -absorption nach der Quantentheorie”. In: *Verh. Deutsch. Phys. Gesell.* 18 (1916), pp. 318–323.
- [4] Albert EINSTEIN. “Quantentheorie der Strahlung”. In: *Mitt. Phys. Ges., Zürich* 16 (1916), p. 47.
- [5] Albert EINSTEIN. “Zur Quantentheorie der Strahlung”. In: *Phys. Z.* 18 (1917), p. 121.
- [6] Jeff HECHT. “A short history of laser development”. In: *Appl. Opt.* 49.25 (2010), F99–F122.
- [7] Arthur L. SCHAWLOW and Charles H. TOWNES. “Infrared and optical masers”. In: *Phys. Rev.* 112.6 (1958), p. 1940.
- [8] Theodore H. MAIMAN et al. “Stimulated optical radiation in ruby”. In: *Nature* 187 (1960), p. 493.
- [9] Ali JAVAN, William R. BENNETT JR, and Donald R. HERRIOTT. “Population inversion and continuous optical maser oscillation in a gas discharge containing a He-Ne mixture”. In: *Phys. Rev. Lett.* 6.3 (1961), p. 106.
- [10] Frank TRÄGER. *Springer handbook of lasers and optics*. Springer New York, 2007.
- [11] Donna STRICKLAND and Gerard MOUROU. “Compression of amplified chirped optical pulses”. In: *Opt. Commun.* 55.6 (1985), pp. 447–449.
- [12] Stuart P. D. MANGLES et al. “Monoenergetic beams of relativistic electrons from intense laser-plasma interactions”. In: *Nature* 431.7008 (2004), pp. 535–538.
- [13] Hui CHEN et al. “Making relativistic positrons using ultraintense short pulse lasers”. In: *Phys. Plasmas* 16.12 (2009), p. 105001.
- [14] E. L. CLARK et al. “Energetic heavy-ion and proton generation from ultraintense laser-plasma interactions with solids”. In: *Phys. Rev. Lett.* 85.8 (2000), p. 1654.
- [15] Anatoly MAKSIMCHUK, Shaoting GU, Kirk FLIPPO, Donald UMSTADTER, and V. Yu. BYCHENKOV. “Forward ion acceleration in thin films driven by a high-intensity laser”. In: *Phys. Rev. Lett.* 84.18 (2000), p. 4108.
- [16] Stephen P. HATCHETT et al. “Electron, photon, and ion beams from the relativistic interaction of Petawatt laser pulses with solid targets”. In: *Phys. Plasmas* 7.5 (2000), pp. 2076–2082.

- [17] R. A. SNAVELY et al. “Intense high-energy proton beams from petawatt-laser irradiation of solids”. In: *Phys. Rev. Lett.* 85.14 (2000), p. 2945.
- [18] Yoshihiro MURAKAMI et al. “Observation of proton rear emission and possible gigagauss scale magnetic fields from ultra-intense laser illuminated plastic target”. In: *Phys. Plasmas* 8.9 (2001), pp. 4138–4143.
- [19] S. BASTIANI et al. “Experimental study of the interaction of subpicosecond laser pulses with solid targets of varying initial scale lengths”. In: *Phys. Rev. E* 56.6 (1997), p. 7179.
- [20] Y. SENTOKU, K. MIMA, T. TAGUCHI, S. MIYAMOTO, and Y. KISHIMOTO. “Particle simulation on x-ray emissions from ultra-intense laser produced plasmas”. In: *Phys. Plasmas* 5.12 (1998), pp. 4366–4372.
- [21] K. B. WHARTON et al. “Experimental measurements of hot electrons generated by ultraintense ($> 10^{19}$ W/cm²) laser-plasma interactions on solid-density targets”. In: *Phys. Rev. Lett.* 81.4 (1998), p. 822.
- [22] M. D. PERRY et al. “Hard x-ray production from high intensity laser solid interactions”. In: *Rev. Sci. Instrum.* 70.1 (1999), pp. 265–269.
- [23] P. A. NORREYS et al. “Observation of a highly directional γ -ray beam from ultrashort, ultraintense laser pulse interactions with solids”. In: *Phys. Plasmas* 6.5 (1999), pp. 2150–2156.
- [24] Heinrich SCHWOERER et al. “MeV X rays and photoneutrons from femtosecond laser-produced plasmas”. In: *Phys. Rev. Lett.* 86.11 (2001), p. 2317.
- [25] K. W. D. LEDINGHAM et al. “Photonuclear physics when a multiterawatt laser pulse interacts with solid targets”. In: *Phys. Rev. Lett.* 84.5 (2000), p. 899.
- [26] S. V. BULANOV and V. S. KHOROSHKOV. “Feasibility of using laser ion accelerators in proton therapy”. In: *Plasma Phys. Rep.* 28.5 (2002), pp. 453–456.
- [27] Victor MALKA et al. “Practicability of protontherapy using compact laser systems”. In: *Med. Phys.* 31.6 (2004), pp. 1587–1592.
- [28] P. K. PATEL et al. “Isochoric heating of solid-density matter with an ultrafast proton beam”. In: *Phys. Rev. Lett.* 91.12 (2003), p. 125004.
- [29] A. J. MACKINNON et al. “Proton radiography as an electromagnetic field and density perturbation diagnostic”. In: *Rev. Sci. Instrum.* 75.10 (2004), pp. 3531–3536.
- [30] K. L. LANCASTER et al. “Characterization of $^7\text{Li}(p,n)^7\text{Be}$ neutron yields from laser produced ion beams for fast neutron radiography”. In: *Phys. Plasmas* 11.7 (2004), pp. 3404–3408.
- [31] Satyabrata KAR et al. “Beamed neutron emission driven by laser accelerated light ions”. In: *New J. Phys.* 18.5 (2016), p. 053002.
- [32] Marianna BARBERIO, S. VELTRI, M. SCISCIO, and P. ANTICI. “Laser-accelerated proton beams as diagnostics for cultural heritage”. In: *Sci. Rep.* 7.1 (2017), pp. 1–8.

-
- [33] M. BARBERIO et al. “Laser-generated proton beams for high-precision ultra-fast crystal synthesis”. In: *Sci. Rep.* 7.1 (2017), pp. 1–9.
- [34] A. MCKELVEY et al. “Thermal conductivity measurements of proton-heated warm dense aluminum”. In: *Sci. Rep.* 7.7015 (2017), pp. 1–10.
- [35] M. BARBERIO et al. “Laser-accelerated particle beams for stress testing of materials”. In: *Nat. Commun.* 9.1 (2018), pp. 1–7.
- [36] Lorenzo ROMAGNANI et al. “Dynamics of the electromagnetic fields induced by fast electron propagation in near-solid-density media”. In: *Phys. Rev. Lett.* 122.2 (2019), p. 025001.
- [37] T. M. OSTERMAYR et al. “Laser-driven x-ray and proton micro-source and application to simultaneous single-shot bi-modal radiographic imaging”. In: *Nat. Commun.* 11.1 (2020), pp. 1–9.
- [38] M. BORGHESI et al. “Multi-MeV Proton Source Investigations in Ultraintense Laser-Foil Interactions”. In: *Phys. Rev. Lett.* 92 (5 2004), p. 055003.
- [39] T. E. COWAN et al. “Ultralow Emittance, Multi-MeV Proton Beams from a Laser Virtual-Cathode Plasma Accelerator”. In: *Phys. Rev. Lett.* 92 (20 2004), p. 204801.
- [40] H. RUHL, T. COWAN, and J. FUCHS. “The generation of micro-fiducials in laser-accelerated proton flows, their imaging property of surface structures and application for the characterization of the flow”. In: *Phys. Plasmas* 11.5 (2004), pp. L17–L20.
- [41] Jörg SCHREIBER et al. “Source-size measurements and charge distributions of ions accelerated from thin foils irradiated by high-intensity laser pulses”. In: *Appl. Phys. B* 79.8 (2004), pp. 1041–1045.
- [42] M. ROTH et al. “Laser accelerated ions in ICF research prospects and experiments”. In: *Plasma Phys. Control Fusion* 47.12B (2005), B841.
- [43] M. ROTH et al. “Laser accelerated heavy particles – Tailoring of ion beams on a nano-scale”. In: *Opt. Commun.* 264.2 (2006). Quantum Control of Light and Matter, pp. 519–524.
- [44] M. NISHIUCHI et al. “Repetitive highly collimated intense proton beam with sub-MeV energy range driven by a compact few terawatt femtosecond laser”. In: *Appl. Phys. B* 87.4 (2007), pp. 615–621.
- [45] M. NISHIUCHI et al. “Efficient production of a collimated MeV proton beam from a polyimide target driven by an intense femtosecond laser pulse”. In: *Phys. Plasmas* 15.5 (2008), p. 053104.
- [46] F. NÜRNBERG et al. “Radiochromic film imaging spectroscopy of laser-accelerated proton beams”. In: *Rev. Sci. Instrum.* 80.3 (2009), p. 033301.
- [47] Brendan DROMEY et al. “Picosecond metrology of laser-driven proton bursts”. In: *Nature communications* 7.1 (2016), pp. 1–6.

- [48] Hiroyuki DAIDO, Mamiko NISHIUCHI, and Alexander S PIROZHKOV. “Review of laser-driven ion sources and their applications”. In: *Rep. Prog. Phys.* 75.5 (2012), p. 056401.
- [49] Max TABAK et al. “Ignition and high gain with ultrapowerful lasers”. In: *Phys. Plasmas* 1.5 (1994), pp. 1626–1634.
- [50] J. MEYER-TER VEHN. “Fast ignition of ICF targets: an overview”. In: *Plasma Phys. Control. Fusion* 43.12A (2001), A113.
- [51] Michael H. KEY. “Status of and prospects for the fast ignition inertial fusion concept”. In: *Phys. Plasmas* 14.5 (2007), p. 055502.
- [52] M. TATARAKIS et al. “Plasma formation on the front and rear of plastic targets due to high-intensity laser-generated fast electrons”. In: *Phys. Rev. Lett.* 81.5 (1998), p. 999.
- [53] M. BORGHESI et al. “Observations of Collimated Ionization Channels in Aluminum-Coated Glass Targets Irradiated by Ultraintense Laser Pulses”. In: *Phys. Rev. Lett.* 83 (21 1999), pp. 4309–4312.
- [54] L. GREMILLET et al. “Time-Resolved Observation of Ultrahigh Intensity Laser-Produced Electron Jets Propagating through Transparent Solid Targets”. In: *Phys. Rev. Lett.* 83 (24 1999), pp. 5015–5018.
- [55] J. S. GREEN et al. “Time-resolved measurements of fast electron recirculation for relativistically intense femtosecond scale laser-plasma interactions”. In: *Sci. Rep.* 8.1 (2018), pp. 1–9.
- [56] R. B. STEPHENS et al. “ K_α fluorescence measurement of relativistic electron transport in the context of fast ignition”. In: *Phys. Rev. E* 69.6 (2004), p. 066414.
- [57] W. THEOBALD et al. “Hot surface ionic line emission and cold K-inner shell emission from petawatt-laser-irradiated Cu foil targets”. In: *Phys. Plasmas* 13.4 (2006), p. 043102.
- [58] K. L. LANCASTER et al. “Measurements of energy transport patterns in solid density laser plasma interactions at intensities of $5 \times 10^{20} \text{ W cm}^{-2}$ ”. In: *Phys. Rev. Lett.* 98.12 (2007), p. 125002.
- [59] J. MYATT et al. “High-intensity laser interactions with mass-limited solid targets and implications for fast-ignition experiments on OMEGA EP”. In: *Phys. Plasmas* 14.5 (2007), p. 056301.
- [60] P. M. NILSON et al. “High-intensity laser-plasma interactions in the refluxing limit”. In: *Phys. Plasmas* 15.5 (2008), p. 056308.
- [61] P. NEUMAYER et al. “The role of hot electron refluxing in laser-generated K -alpha sources”. In: *Phys. Plasmas* 17.10 (2010), p. 103103.
- [62] U. TEUBNER et al. “Harmonic Emission from the Rear Side of Thin Overdense Foils Irradiated with Intense Ultrashort Laser Pulses”. In: *Phys. Rev. Lett.* 92 (18 2004), p. 185001.
- [63] F. QUÉRÉ et al. “Coherent Wake Emission of High-Order Harmonics from Overdense Plasmas”. In: *Phys. Rev. Lett.* 96 (12 2006), p. 125004.

-
- [64] B. DROMEY et al. “Coherent synchrotron emission from electron nanobunches formed in relativistic laser–plasma interactions”. In: *Nature Physics* 8.11 (2012), pp. 804–808.
 - [65] M. YEUNG et al. “Dependence of Laser-Driven Coherent Synchrotron Emission Efficiency on Pulse Ellipticity and Implications for Polarization Gating”. In: *Phys. Rev. Lett.* 112 (12 2014), p. 123902.
 - [66] J. J. SANTOS et al. “Fast Electron Transport in Ultraintense Laser Pulse Interaction with Solid Targets by Rear-Side Self-Radiation Diagnostics”. In: *Phys. Rev. Lett.* 89 (2 2002), p. 025001.
 - [67] S. D. BATON et al. “Evidence of Ultrashort Electron Bunches in Laser-Plasma Interactions at Relativistic Intensities”. In: *Phys. Rev. Lett.* 91 (10 2003), p. 105001.
 - [68] Jian ZHENG et al. “Study of Hot Electrons by Measurement of Optical Emission from the Rear Surface of a Metallic Foil Irradiated with Ultraintense Laser Pulse”. In: *Phys. Rev. Lett.* 92 (16 2004), p. 165001.
 - [69] R. JUNG et al. “Study of Electron-Beam Propagation through Preionized Dense Foam Plasmas”. In: *Phys. Rev. Lett.* 94 (19 2005), p. 195001.
 - [70] H. POPESCU et al. “Subfemtosecond, coherent, relativistic, and ballistic electron bunches generated at ω_0 and $2\omega_0$ in high intensity laser-matter interaction”. In: *Phys. Plasmas* 12.6 (2005), p. 063106.
 - [71] M. MANCLOSSI et al. “Study of Ultraintense Laser-Produced Fast-Electron Propagation and Filamentation in Insulator and Metal Foil Targets by Optical Emission Diagnostics”. In: *Phys. Rev. Lett.* 96 (12 2006), p. 125002.
 - [72] J. J. SANTOS et al. “Fast-electron transport and induced heating in aluminum foils”. In: *Phys. Plasmas* 14.10 (2007), p. 103107.
 - [73] M. STORM et al. “High-Current, Relativistic Electron-Beam Transport in Metals and the Role of Magnetic Collimation”. In: *Phys. Rev. Lett.* 102 (23 2009), p. 235004.
 - [74] B. I. CHO et al. “Characterization of two distinct, simultaneous hot electron beams in intense laser-solid interactions”. In: *Phys. Rev. E* 80 (5 2009), p. 055402.
 - [75] C. BELLEI et al. “Micron-scale fast electron filaments and recirculation determined from rear-side optical emission in high-intensity laser–solid interactions”. In: *New J. Phys.* 12.7 (2010), p. 073016.
 - [76] J. KERN et al. “Simultaneous imaging of K- α radiation and coherent transition radiation from relativistic-intensity laser-irradiated solid target plasmas”. In: *High Energy Density Phys.* 8.1 (2012), pp. 60–65.
 - [77] J. BLAKENEY, H. QUEVEDO, G. M. DYER, and T. DITMIRE. “Characterization of laser produced hot electron propagation via coherent transition radiation in cold and warm dense aluminum”. In: *Phys. Plasmas* 27.12 (2020), p. 123105.
 - [78] Jin Woo YOON et al. “Achieving the laser intensity of 5.5×10^{22} W/cm² with a wavefront-corrected multi-PW laser”. In: *Opt. Express* 27.15 (2019), pp. 20412–20420.

- [79] Colin N. DANSON et al. “Petawatt and exawatt class lasers worldwide”. In: *High Power Laser Sci. Eng.* 7 (2019).
- [80] Paul GIBBON. *Short pulse laser interactions with matter: An introduction*. London: Imperial College Press, 2007.
- [81] Paul MCKENNA and Mark N. QUINN. “Energetic Electron Generation and Transport in Intense Laser-Solid Interactions”. In: *Laser-Plasma Interactions and Applications*. Ed. by Paul MCKENNA, David NEELY, Robert BINGHAM, and Dino A. JAROSZYNSKI. Springer, 2013. Chap. 5, pp. 91–112.
- [82] Klaus EIDMANN et al. “Fundamental and harmonic emission from the rear side of a thin overdense foil irradiated by an intense ultrashort laser pulse”. In: *Phys. Rev. E* 72.3 (2005), p. 036413.
- [83] H. GEORGE, F. QUÉRÉ, Cédric THAURY, G. BONNAUD, and Ph. MARTIN. “Mechanisms of forward laser harmonic emission from thin overdense plasmas”. In: *New J. Phys.* 11.11 (2009), p. 113028.
- [84] Wolfgang DEMTRÖDER. *Experimentalphysik 3: Atome, Moleküle und Festkörper*. Springer-Verlag, 2016.
- [85] José A. BITTENCOURT. *Fundamentals of plasma physics*. 3rd ed. Springer Science & Business Media, 2004.
- [86] Albert EINSTEIN. “Zur Theorie der Lichterzeugung und Lichtabsorption”. In: *Ann. Phys.* 325.6 (1906), pp. 199–206.
- [87] J. R. RUMBLE. *CRC Handbook of Chemistry and Physics, 100th edn., 2019–2020*. 2019.
- [88] Scott C. WILKS and William L. KRUER. “Absorption of ultrashort, ultra-intense laser light by solids and overdense plasmas”. In: *IEEE J. Quantum Electron.* 33.11 (1997), pp. 1954–1968.
- [89] Leonid V. KELDYSH. “Ionization in the field of a strong electromagnetic wave”. In: *Sov. Phys. JETP* 20.5 (1965), pp. 1307–1314.
- [90] Malte C. KALUZA. *High-Intensity/Relativistic Optics*. lecture notes. 2020.
- [91] Gerhard G. PAULUS and Matthias KÜBEL. *Strong Field Laser Physics*. lecture notes. July 2020.
- [92] Steeve AUGST, David D MEYERHOFER, Donna STRICKLAND, and See-Leang CHIN. “Laser ionization of noble gases by Coulomb-barrier suppression”. In: *JOSA B* 8.4 (1991), pp. 858–867.
- [93] Francis F. CHEN. *Introduction to Plasma Physics and Controlled Fusion*. 3rd ed. Cham ; Heidelberg ; New York ; Dordrecht ; London : Springer, 2016.
- [94] Peter MULSER and Dieter BAUER. *High Power Laser–Matter Interaction*. Springer Tracts in Modern Physics 238. Berlin Heidelberg: Springer, 2010.

-
- [95] V. A. VSHIVKOV, N. M. NAUMOVA, F. PEGORARO, and S. V. BULANOV. “Nonlinear electrodynamics of the interaction of ultra-intense laser pulses with a thin foil”. In: *Phys. Plasmas* 5.7 (1998), pp. 2727–2741.
 - [96] V. I. EREMIN, A. V. KORZHIMANOV, and A. V. KIM. “Relativistic self-induced transparency effect during ultraintense laser interaction with overdense plasmas: Why it occurs and its use for ultrashort electron bunch generation”. In: *Phys. Plasmas* 17.4 (2010), p. 043102.
 - [97] Max BORN and Emil WOLF. *Principles of Optics*. 6th ed. Oxford: Pergamon Press, 1980.
 - [98] William L. KRUER. *The physics of laser plasma interaction*. Addison-Wesley, New York, 1988.
 - [99] S. C. WILKS, W. L. KRUER, M. TABAK, and A. B. LANGDON. “Absorption of ultra-intense laser pulses”. In: *Phys. Rev. Lett.* 69.9 (1992), p. 1383.
 - [100] F. BRUNEL. “Not-so-resonant, resonant absorption”. In: *Phys. Rev. Lett.* 59.1 (1987), p. 52.
 - [101] W. L. KRUER and K. ESTABROOK. “J×B heating by very intense laser light”. In: *The Physics of fluids* 28.1 (1985), pp. 430–432.
 - [102] Ferencz JÜTTNER. “Das Maxwellsche Gesetz der Geschwindigkeitsverteilung in der Relativtheorie”. In: *Ann. Phys.* 339.5 (1911), pp. 856–882.
 - [103] Georg Alexander BECKER. “Characterization of laser-driven proton acceleration with contrast-enhanced laser pulses”. PhD thesis. Friedrich-Schiller Universität Jena, 2021.
 - [104] Andrea MACCHI, Marco BORGHESI, and Matteo PASSONI. “Ion acceleration by super-intense laser-plasma interaction”. In: *Rev. Mod. Phys.* 85.2 (2013), p. 751.
 - [105] D. BAUER, P. MULSER, and W.-H. STEEB. “Relativistic ponderomotive force, uphill acceleration, and transition to chaos”. In: *Phys. Rev. Lett.* 75.25 (1995), p. 4622.
 - [106] G. MALKA and J. L. MIQUEL. “Experimental confirmation of ponderomotive-force electrons produced by an ultrarelativistic laser pulse on a solid target”. In: *Phys. Rev. Lett.* 77.1 (1996), p. 75.
 - [107] P. M. NILSON et al. “Time-resolved measurements of hot-electron equilibration dynamics in high-intensity laser interactions with thin-foil solid targets”. In: *Phys. Rev. Lett.* 108.8 (2012), p. 085002.
 - [108] F. N. BEG et al. “A study of picosecond laser–solid interactions up to 10^{19} W cm^{−2}”. In: *Phys. Plasmas* 4.2 (1997), pp. 447–457.
 - [109] Hui CHEN, Scott C. WILKS, William L. KRUER, P. K. PATEL, and R. SHEPHERD. “Hot electron energy distributions from ultraintense laser solid interactions”. In: *Phys. Plasmas* 16.2 (2009), p. 020705.
 - [110] Tsuyoshi TANIMOTO et al. “Measurements of fast electron scaling generated by petawatt laser systems”. In: *Phys. Plasmas* 16.6 (2009), p. 062703.

- [111] A. J. KEMP, Yasuhiko SENTOKU, and Max TABAK. “Hot-electron energy coupling in ultraintense laser-matter interaction”. In: *Phys. Rev. Lett.* 101.7 (2008), p. 075004.
- [112] M. G. HAINES, M. S. WEI, F. N. BEG, and R. B. STEPHENS. “Hot-electron temperature and laser-light absorption in fast ignition”. In: *Phys. Rev. Lett.* 102.4 (2009), p. 045008.
- [113] T. KLUGE et al. “Electron temperature scaling in laser interaction with solids”. In: *Phys. Rev. Lett.* 107.20 (2011), p. 205003.
- [114] Hannes ALFVÉN. “On the motion of cosmic rays in interstellar space”. In: *Phys. Rev.* 55.5 (1939), p. 425.
- [115] A. J. MACKINNON et al. “Enhancement of proton acceleration by hot-electron recirculation in thin foils irradiated by ultraintense laser pulses”. In: *Phys. Rev. Lett.* 88.21 (2002), p. 215006.
- [116] John David JACKSON. *Klassische Elektrodynamik*. Ed. by Kurt MÜLLER, Christopher WITTE, Martin DIESTELHORST, and John David JACKSON. 5th ed. Berlin: de Gruyter, 2014.
- [117] Francis A. JENKINS and Harvey E. WHITE. *Fundamentals of Optics*. 3rd ed. New York, Toronto, London: McGraw-Hill Book Company, 1957.
- [118] Kurt LECHNER. *Classical Electrodynamics*. Springer International Publishing AG, 2018.
- [119] P. A. ČERENKOV. In: *C. R. Acad. Sci. USSR* 8 (1934), p. 451.
- [120] P. A. ČERENKOV. In: *C. R. Acad. Sci. USSR* 12.3 (1936), p. 413.
- [121] P. A. ČERENKOV. In: *C. R. Acad. Sci. USSR* 14 (1937), p. 102.
- [122] P. A. ČERENKOV. In: *C. R. Acad. Sci. USSR* 14 (1937), p. 105.
- [123] P. A. ČERENKOV. “Visible radiation produced by electrons moving in a medium with velocities exceeding that of light”. In: *Phys. Rev.* 52.4 (1937), p. 378.
- [124] I. FRANK and Ig. TAMM. In: *C. R. Acad. Sci. USSR* 14.3 (1937), p. 109.
- [125] Boris M. BOLOTOVSKII. “Vavilov–Cherenkov radiation: its discovery and application”. In: *Phys.-Uspekhi* 52.11 (2009), p. 1099.
- [126] Matthias BARTELMANN et al. “Theoretische Physik”. In: Berlin; Heidelberg: Springer Spektrum, 2015. Chap. Relativistische Mechanik, p. 367.
- [127] Michael VOLLMER. “Cherenkov radiation: why is it perceived as blue?” In: *Eur. J. Phys.* 41.6 (2020), p. 065304.
- [128] Markus ROTH and Marius SCHOLLMEIER. “Ion Acceleration: TNSA”. In: *Laser-Plasma Interactions and Applications*. Ed. by Paul MCKENNA, David NEELY, Robert BINGHAM, and Dino A. JAROSZYNSKI. Springer, 2013. Chap. 12, pp. 303–350.
- [129] B. DROMEY et al. “Coherent synchrotron emission in transmission from ultrathin relativistic laser plasmas”. In: *New J. Phys.* 15.1 (2013), p. 015025.
- [130] S. COUSENS, B. REVILLE, B. DROMEY, and M. ZEPF. “Temporal structure of attosecond pulses from laser-driven coherent synchrotron emission”. In: *Phys. Rev. Lett.* 116.8 (2016), p. 083901.

-
- [131] S. COUSENS, M. YEUNG, M. ZEPF, and B. DROMEY. “Electron trajectories associated with laser-driven coherent synchrotron emission at the front surface of overdense plasmas”. In: *Phys. Rev. E* 101.5 (2020), p. 053210.
- [132] Bertrand MARTINEZ, Emmanuel D’HUMIÈRES, and Laurent GREMILLET. “Synchrotron radiation from ultrahigh-intensity laser-plasma interactions and competition with Bremsstrahlung in thin foil targets”. In: *Phys. Rev. Res.* 2.4 (2020), p. 043341.
- [133] Sébastien CORDE et al. “Femtosecond x rays from laser-plasma accelerators”. In: *Rev. Mod. Phys.* 85.1 (2013), p. 1.
- [134] Jon M. WALLACE. “Nonlocal Energy Deposition in High-Intensity Laser-Plasma Interactions”. In: *Phys. Rev. Lett.* 55 (7 1985), pp. 707–710.
- [135] Paul KOLODNER and Eli YABLONOVITCH. “Two-dimensional distribution of self-generated magnetic fields near the laser-plasma resonant-interaction region”. In: *Phys. Rev. Lett.* 43.19 (1979), p. 1402.
- [136] D. R. RUSBY et al. “Effect of rear surface fields on hot, refluxing and escaping electron populations via numerical simulations”. In: *High Power Laser Sci. Eng.* 7 (2019).
- [137] Frank HINTERBERGER. *Physik der Teilchenbeschleuniger und Ionenoptik*. 2nd ed. Berlin, Heidelberg: Springer, 2008.
- [138] Julian SCHWINGER. “On the classical radiation of accelerated electrons”. In: *Phys. Rev.* 75.12 (1949), p. 1912.
- [139] V. L. GINZBURG and I. M. FRANK. “Radiation from a uniformly moving electron passing from one medium to another”. In: *Journ. of Experimental and Theoretical Physics (JETP)* V 16 (1946), pp. 15–26.
- [140] Mikhail Leonovich TER-MIKAELIAN. *High energy electromagnetic processes in condensed media*. Wiley-Interscience, 1972.
- [141] Luke C. L. YUAN, C. L. WANG, H. UTO, and S. PRÜNSTER. “Formation-Zone Effect in Transition Radiation Due to Ultrarelativistic Particles”. In: *Phys. Rev. Lett.* 25 (21 1970), pp. 1513–1515.
- [142] Claudio BELLEI. “Measurements of Optical Radiation from High-Intensity Laser-Plasma Interactions”. PhD thesis. Imperial College London, 2009.
- [143] Harald IBACH and Hans LÜTH. *Festkörperphysik: Einführung in die Grundlagen*. 7th ed. Springer-Verlag, 2009.
- [144] C. BELLEI, J. R. DAVIES, P. K. CHAUHAN, and Z. NAJMUDIN. “Coherent transition radiation in relativistic laser–solid interactions”. In: *Plasma Phys. Control. Fusion* 54.3 (2012), p. 035011.
- [145] Duncan J. WINGHAM. “Electron synchrotron radiation in the far infrared”. In: *Phys. Rev. D* 35.8 (1987), p. 2584.
- [146] K. ISHI et al. “Spectrum of coherent synchrotron radiation in the far-infrared region”. In: *Phys. Rev. A* 43.10 (1991), p. 5597.

- [147] Roberto ALOISIO and Pasquale BLASI. “Theory of synchrotron radiation: I. Coherent emission from ensembles of particles”. In: *Astropart. Phys.* 18.2 (2002), pp. 183–193.
- [148] Daniel AN DER BRÜGGE and Alexander PUKHOV. “Theory of Attosecond Pulses from Relativistic Surface Plasmas”. In: *arXiv preprint arXiv:1111.4133* (2011).
- [149] J. M. MIKHAILOVA et al. “Isolated attosecond pulses from laser-driven synchrotron radiation”. In: *Phys. Rev. Lett.* 109.24 (2012), p. 245005.
- [150] Jian ZHENG et al. “Spectrum of transition radiation from hot electrons generated in ultra-intense laser plasma interaction”. In: *Phys. Plasmas* 9.8 (2002), pp. 3610–3616.
- [151] Jian ZHENG et al. “Theoretical study of transition radiation from hot electrons generated in the laser–solid interaction”. In: *Phys. Plasmas* 10.7 (2003), pp. 2994–3003.
- [152] Carl B. SCHROEDER, Eric ESAREY, Jeroen VAN TILBORG, and Wim P. LEEMANS. “Theory of coherent transition radiation generated at a plasma-vacuum interface”. In: *Phys. Rev. E* 69.1 (2004), p. 016501.
- [153] Jörn DUNKEL, Peter TALKNER, and Peter HÄNGGI. “Relative entropy, Haar measures and relativistic canonical velocity distributions”. In: *New J. Phys.* 9.5 (2007), p. 144.
- [154] PYTHON SOFTWARE FOUNDATION. *Python Language Reference*. version 3.8. <https://www.python.org>, 2019.
- [155] J. D. HUNTER. “Matplotlib: A 2D graphics environment”. In: *Comput. Sci. Eng.* 9.3 (2007), pp. 90–95.
- [156] Pauli VIRTANEN et al. “SciPy 1.0: Fundamental Algorithms for Scientific Computing in Python”. In: *Nat. Methods* 17 (2020), pp. 261–272.
- [157] Charles R. HARRIS et al. “Array programming with NumPy”. In: *Nature* 585.7825 (2020), pp. 357–362.
- [158] NATIONAL INSTRUMENTS CORP. *LabVIEW*. <https://www.ni.com/en-us/shop/labview.html>. 2014.
- [159] *POLARIS Laser System*. https://www.hi-jena.de/en/helmholtz_institute_jena/about-the-helmholtz-institute-jena/experimental_facilities/local/polaris/.
- [160] Marco HORNUNG et al. “54 J pulses with 18 nm bandwidth from a diode-pumped chirped-pulse amplification laser system”. In: *Opt. Lett.* 41.22 (2016), pp. 5413–5416.
- [161] *Mitutoyo Apochromatic NIR Objective*. https://www.thorlabs.com/newgrouppage9.cfm?objectgroup_id=9922. Item # MY10X-823.
- [162] S. I. BAJLEKOV et al. “Longitudinal electron bunch profile reconstruction by performing phase retrieval on coherent transition radiation spectra”. In: *Phys. Rev. Accel. Beams* 16.4 (2013), p. 040701.
- [163] Matthias HEIGOLDT et al. “Temporal evolution of longitudinal bunch profile in a laser wakefield accelerator”. In: *Phys. Rev. Accel. Beams* 18.12 (2015), p. 121302.

-
- [164] Q. Q. SU et al. “Temporal diagnostics of femtosecond electron bunches with complex structures using sparsity-based algorithm”. In: *Phys. Rev. Accel. Beams* 21.11 (2018), p. 112801.
 - [165] Omid ZARINI et al. “Advanced methods for temporal reconstruction of modulated electron bunches”. In: *2018 IEEE Advanced Accelerator Concepts Workshop (AAC)*. IEEE. 2018, pp. 1–5.
 - [166] Omid ZARINI. “Measuring Sub-Femtosecond Temporal Structures in Multi-Ten Kilo-ampere Electron Beams”. PhD thesis. Universität Dresden, 2019.
 - [167] Marco HORNING. “Mosaik-Gitter-Kompressor für Femtosekunden-Laserimpulse hoher Energie”. PhD thesis. Friedrich-Schiller Universität Jena, 2010.
 - [168] Issa TAMER. “Petawatt-Class Laser Optimization and Ultrashort Probe Pulse Generation for Relativistic Laser-Plasma Interactions”. PhD thesis. Friedrich-Schiller-Universität Jena, 2020.
 - [169] Georg Alexander BECKER. *Private Communication*. georg.becker@uni-jena.de. 2020.
 - [170] *Positive 1951 USAF test target*. https://www.thorlabs.com/newgrouppage9.cfm?objectgroup_id=4338. Item # R1DS1P.
 - [171] Joachim HEIN. *Private Communication*. joachim.hein@uni-jena.de. 2021.
 - [172] Hermann SLEVOGT. *Technische Optik*. Berlin: de Gruyter, 1974.
 - [173] *Absorptive ND Filter Kit*. https://www.thorlabs.com/newgrouppage9.cfm?objectgroup_id=689.
 - [174] *Wollaston Prism*. https://www.thorlabs.com/newgrouppage9.cfm?objectgroup_id=917. Item # WPQ10.
 - [175] https://refractiveindex.info/?shelf=glass&book=fused_silica&page=Malitson.
 - [176] Ian H. MALITSON. “Interspecimen comparison of the refractive index of fused silica”. In: *Josa* 55.10 (1965), pp. 1205–1209.
 - [177] C. Z. TAN. “Determination of refractive index of silica glass for infrared wavelengths by IR spectroscopy”. In: *J. Non-Cryst. Solids* 223.1-2 (1998), pp. 158–163.
 - [178] Marco HORNING. *Private Communication*. marco.horning@uni-jena.de. 2021.
 - [179] G. DOUMY et al. “Complete characterization of a plasma mirror for the production of high-contrast ultraintense laser pulses”. In: *Phys. Rev. E* 69 (2 2004), p. 026402.
 - [180] Matthew SCHWAB. *Private Communication*. matthew.schwab@uni-jena.de. 2021.
 - [181] Laurent GREMILLET, Guy BONNAUD, and François AMIRANOFF. “Filamented transport of laser-generated relativistic electrons penetrating a solid target”. In: *Phys. Plasmas* 9.3 (2002), pp. 941–948.
 - [182] M. S. WEI et al. “Observations of the filamentation of high-intensity laser-produced electron beams”. In: *Phys. Rev. E* 70.5 (2004), p. 056412.

- [183] M. N. QUINN et al. “On the investigation of fast electron beam filamentation in laser-irradiated solid targets using multi-MeV proton emission”. In: *Plasma Phys. Control. Fusion* 53.12 (2011), p. 124012.
- [184] Gregory K. NGIRMANG et al. “Evidence of radial Weibel instability in relativistic intensity laser-plasma interactions inside a sub-micron thick liquid target”. In: *Sci. Rep.* 10.1 (2020), pp. 1–10.
- [185] J. R. DAVIES. “Laser absorption by overdense plasmas in the relativistic regime”. In: *Plasma Phys. Control. Fusion* 51.1 (2008), p. 014006.
- [186] P. M. NILSON et al. “Bulk heating of solid-density plasmas during high-intensity-laser plasma interactions”. In: *Phys. Rev. E* 79.1 (2009), p. 016406.
- [187] C. D. CHEN et al. “Bremsstrahlung and $K\alpha$ fluorescence measurements for inferring conversion efficiencies into fast ignition relevant hot electrons”. In: *Phys. Plasmas* 16.8 (2009), p. 082705.
- [188] Hartmut LIEBETRAU et al. “Intracavity stretcher for chirped-pulse amplification in high-power laser systems”. In: *Opt. Lett.* 42.2 (2017), pp. 326–329.
- [189] Sebastian KEPPLER. “Räumlich-zeitliche Optimierung der Laserimpulse Yb³⁺-basierter Hochleistungs-Lasersysteme”. PhD thesis. Friedrich-Schiller Universität Jena, 2017.
- [190] Max MÄUSEZAHN. “Untersuchung lasergetriebener Protonenbeschleunigung bezüglich Vorplasmaerzeugung und räumlicher Protonendetektion”. MA thesis. Friedrich-Schiller-University Jena, 2019.
- [191] Cédric THAURY and F. QUÉRÉ. “High-order harmonic and attosecond pulse generation on plasma mirrors: basic mechanisms”. In: *J. Phys. B: At. Mol. Opt. Phys.* 43.21 (2010), p. 213001.
- [192] A. MALVACHE, A. BOROT, F. QUÉRÉ, and R. LOPEZ-MARTENS. “Coherent wake emission spectroscopy as a probe of steep plasma density profiles”. In: *Phys. Rev. E* 87.3 (2013), p. 035101.
- [193] Mathis NOLTE. *Charakterisierung expandierter ultradünner DLC-Folien für die Laser-Protonenbeschleunigung*. bachelor thesis. 2020.
- [194] Philipp O. J. SCHERER. *Computational Physics - Simulations of Classical and Quantum Systems*. 3rd ed. Springer, 2017.
- [195] J. S. GREEN et al. “Effect of laser intensity on fast-electron-beam divergence in solid-density plasmas”. In: *Phys. Rev. Lett.* 100.1 (2008), p. 015003.
- [196] K. U. AKLI et al. “Time dependence of fast electron beam divergence in ultraintense laser-plasma interactions”. In: *Phys. Rev. E* 86.2 (2012), p. 026404.
- [197] N. P. DOVER et al. “Effect of small focus on electron heating and proton acceleration in ultrarelativistic laser-solid interactions”. In: *Phys. Rev. Lett.* 124.8 (2020), p. 084802.

-
- [198] Guoqian LIAO et al. “Multimillijoule coherent terahertz bursts from picosecond laser-irradiated metal foils”. In: *Proceedings of the National Academy of Sciences* 116.10 (2019), pp. 3994–3999.

Acronyms

AC	autocorrelation.
Al	aluminum.
arb. u.	arbitrary units (sometimes also abbreviated as arb. units).
ASE	Amplified Spontaneous Emission.
c.o.m.	center of mass.
CCD	Charge-Coupled Device.
COR	coherent optical radiation.
CPA	Chirped Pulse Amplification.
CSR	coherent synchrotron radiation.
CTR	coherent transition radiation.
cw	continuous-wave.
CWE	coherent wake emission.
e.o.m.	equation of motion.
EM	electromagnetic.
Eq.	equation.
FI	Fast Ignition.
Fig.	figure.
FROG	Frequency-Resolved Optical Gating.
FWHM	Full Width at Half Maximum.
HWHM	Half Width at Half Maximum.
ICF	Inertial Confinement Fusion.
IR	infrared.
ITR	incoherent transition radiation.
laser	Light Amplification by Stimulated Emission of Radiation.

MPI	Multi-Photon Ionization.
ND	neutral density.
NIR	near-infrared.
NOPA	nonlinear optical parametric amplification.
OTBI	Over-The-Barrier Ionization.
PIC	particle-in-cell.
PM	plasma mirror.
POLARIS	Petawatt Optical Laser Amplifier for Radiation Intensive Experiments.
RHS	right-hand side.
SPIDER	Spectral Phase Interferometry for Direct Electric Field Reconstruction.
SR	synchrotron radiation.
TI	Tunnel Ionization.
TIC	temporal intensity contrast.
TNSA	Target-Normal-Sheath-Acceleration.
TR	transition radiation.
WKB	Wentzel, Kramers and Brillouin approximation.
XUV	extreme ultraviolet.

Mathematical Notation

This section provides a reference describing the notation of the most common variables, constants, functions and conventions that have been used throughout this thesis.

Special Functions and Other Conventions

$[a, b)$ Intervals are indicated by round and square brackets. Square brackets mark an closed interval (i.e. the interval boundary values are included) and round brackets mark open intervals (i.e. the interval boundary values are not included). The given example of $[a, b)$ denotes an interval from a (included) to b (excluded).

$\delta(x)$ Dirac delta function

$\mathcal{K}(x)$ Complete elliptical integral of first kind $\mathcal{K}(x) = \int_0^{\pi/2} [1 - x \sin^2(t)]^{-1/2} dt$

$\{a, b, c\}$ Sets are indicated by curly brackets. For the given example of $\{a, b, c\}$, the set contains the values a , b , and c .

i Imaginary unit $i = \sqrt{-1}$

$K_\alpha(x)$ Modified Bessel function of second kind of order α

Physics Constants

ϵ_0 Vacuum permittivity

μ_0 Vacuum permeability

c Speed of light (in vacuum)

e Absolute electric charge of an electron

h Planck constant ($\hbar = h/2\pi$)

k_B Boltzmann constant

m_e Electron rest mass

m_i Ion rest mass

Variables in the Context of TR and SR

Δ_ψ Divergence half angle of a hot electron current

t_l	Time of "creation" (i.e. acceleration) of the l^{th} hot electron bunch at the target front surface
ρ	Radius of the momentary circular trajectory in the electric sheath field at the rear surface of a target which has been illuminated by a relativistic laser pulse
σ_r	Initial width of hot electron bunch in xy-plane (see Fig. 2.2)
σ_t	Initial temporal duration of hot electron bunch
a	The temporal delay between the hot electron population 1 (accelerated at ω_L) and the hot electron population 2 (accelerated at $2\omega_L$)
$d(\omega)$	Formation length of transition radiation at frequency ω
d_0	Thickness of target which is illuminated by a relativistic laser pulse
N	Total number of electrons in hot electron current
n_b	Number of hot electron bunches
P_1	Relative number of electrons per bunch produced at ω_L
P_2	Relative number of electrons per bunch produced at $2\omega_L$
W_e	Relativistic electron energy $W_e = \gamma_e m_e c^2$
W_T	Normalized thermal energy $W_T = k_B T_h / m_e c^2$

Variables

χ_e	Resistivity
$\Delta\lambda$	Laser spectral width (FWHM)
Δt	Laser pulse duration (FWHM)
ϵ	Dielectric constant
η	Refractive index
γ	Relativistic factor $\gamma = (1 - \beta^2)^{-1/2}$
λ	Wavelength
λ_D	Debye length
λ_L	Central laser wavelength (in vacuum)
λ_μ	Laser wavelength in μm
\mathcal{A}	Area of a spatial intensity distribution (usually of the laser focal spot if not stated differently)

$\mathcal{A}_{\text{FWHM}}$	Area of the spatial intensity region where the intensity (usually the laser intensity or the COR intensity) $I(x, y)$ fulfills $I(x, y) \geq \max[I(x, y)]/2$
\mathcal{T}	optical period $\mathcal{T} = \nu^{-1}$
\mathcal{T}_{L}	optical laser period $\mathcal{T}_{\text{L}} = \nu_{\text{L}}^{-1}$
ν	Frequency
ν_{ei}	Electron-ion collision frequency
ν_{L}	Central laser frequency
Ω	Solid Angle $\Omega = (\alpha, \theta)$ (see Fig. 2.2)
ω	angular frequency $\omega = 2\pi\nu$
ω_{L}	Central laser angular frequency
ω_{p}	Angular plasma frequency
Π	Efficiency
$\Pi_{\text{L} \rightarrow \text{e}}$	Conversion efficiency of laser energy to hot electron energy
σ_{e}	Conductivity $\sigma_{\text{e}} = \chi_{\text{e}}^{-1}$
σ_{j}	Cross-section of the j-photon ionization
τ	FWHM pulse duration of the laser pulse and sometimes used instead of τ_{FWHM}
τ_{ei}	Electron-ion relaxation time (i.e. the lifetime of a plasma)
τ_{FWHM}	FWHM pulse duration of the laser pulse
τ_{ξ}	Keldysh time $\tau_{\xi} = \xi/\omega_{\text{L}}$
Γ_{tunnel}	Ionization rate of tunnel ionization
Γ_{j}	Ionization rate for the j-photon ionization
$\varphi_{\text{parabola}}$	Horizontal angle of the parabola which focuses the laser pulse on the target
$\vec{\beta}$	Normalized velocity \vec{v}/c
\vec{A}	Vector potential of an electromagnetic field
\vec{B}	Magnetic flux density
\vec{D}	Electric flux density
\vec{E}	Electric field
\vec{E}_{S}	Temporally averaged electric field of the laser

\vec{F}_p	Ponderomotive force $\vec{F}_p = -\vec{\nabla} U_p$
\vec{H}	Magnetic field
\vec{j}	Current density
\vec{k}	Wave vector $\vec{k} = \omega/c(\sin\theta \cos\alpha, \sin\theta \sin\alpha, \cos\theta)$ (see Fig. 2.2)
\vec{k}_\perp	Wave vector $\vec{k}_\perp = (k_x, k_y)^T$ perpendicular to z-axis
\vec{M}	Magnetic polarization
\vec{P}	Dielectric polarization
\vec{p}	Momentum $\vec{p} = p(\sin\psi \cos\phi, \sin\psi \sin\phi, \cos\psi)^T$ (see Fig. 2.2)
\vec{r}	Spatial coordinate $\vec{r} = (x, y, z)^T$
\vec{r}_\perp	Spatial coordinate perpendicular to z-axis $\vec{r}_\perp = (x, y)^T$
\vec{S}	Poynting vector
\vec{u}	Normalized momentum $\vec{u} = \gamma\beta\vec{p}/p$
\vec{v}	Velocity perpendicular to z-axis $\vec{v}_\perp = (v_x, v_y)^T$
\vec{v}_e	Electron velocity
ξ	Keldysh parameter
c_s	Speed of sound
$d_{\text{lim}}(\lambda)$	Resolution limit of an imaging system for radiation at the wavelength λ
I	Intensity (usually of light)
I_L	Laser Intensity
I_{18}	Laser intensity in units of 10^{18} W/cm^2
J	Current
k	wavenumber $k = 2\pi/\lambda$
L	Plasma scale length
l_s	Skin depth to which the laser tunnels into the overcritical plasma
n	Particle density
n_{cr}	Critical density above which the laser is reflected by the plasma
$n_{e,0}$	Equilibrium electron density

n_e	Electron density
n_f	Fast electron density
n_i	Ion density
q	Electric charge
q_{FWHM}	Quality factor of the laser focal shot. q_{FWHM} corresponds to the percentage of laser energy contained in $\mathcal{A}_{\text{FWHM}}$.
T	Temperature
t	time
T_e	Bulk temperature of electrons in a plasma
T_h	Temperature of hot electrons (also called fast electrons) in a plasma and $T_h \gg T_e$
T_i	Bulk temperature of ions in a plasma
U	Potential Energy
U_{ion}	Ionization potential
U_P	Ponderomotive potential (corresponds to the averaged kinetic energy of an electron in the laser field)
V	Volume
v_{th}	Thermal electron velocity
W	Energy
W_{kin}	Kinetic energy
W_L	Laser pulse energy
W_{ph}	Photon energy $W_{\text{ph}} = h\nu$
Z	Ion charge in units of e
Z^*	Effective ion charge in units of e

A. Light and Lasers

Light is the fundamental ingredient which allows us to interact with our environment and to acquire knowledge and understanding of our surrounding. Mostly, we do not care about its physical nature in our everyday life. However, focusing high-intensity lasers to reach light intensities which are otherwise not present on our planet is far from an ordinary event and requires knowledge of the physical description of light. Therefore, this chapter aims to provide an overview over the physical framework of light and lasers.

Light is an electromagnetic wave and classically well described by the four Maxwell's equations

$$\begin{aligned}\vec{\nabla} \cdot \vec{D}(\vec{r}, t) &= \rho(\vec{r}, t), \quad \vec{\nabla} \cdot \vec{B}(\vec{r}, t) = 0, \\ \vec{\nabla} \times \vec{E}(\vec{r}, t) &= -\frac{\partial \vec{B}(\vec{r}, t)}{\partial t}, \quad \vec{\nabla} \times \vec{H}(\vec{r}, t) = \frac{\partial \vec{D}(\vec{r}, t)}{\partial t} + \vec{j}(\vec{r}, t),\end{aligned}\tag{A.1}$$

with the electric field vector $\vec{E} = (\vec{D} - \vec{P})/\epsilon_0$, the magnetic field vector $\vec{H} = (\vec{B} - \vec{M})/\mu_0$, the charge density ρ and the current density \vec{j} . Here, the electric displacement \vec{D} , the magnetic induction \vec{B} , the electric polarization \vec{P} , and the magnetization \vec{M} have been used whereas the latter two are zero in vacuum and in plasma. Moreover, the constants ϵ_0 (vacuum permittivity) and μ_0 (vacuum permeability) have been introduced. For the description of electromagnetic waves, it is often convenient to write the electric field and the magnetic induction as a function of the vector potential \vec{A} . Hence $\vec{B} = \vec{\nabla} \times \vec{A}$ and $\vec{E} + \frac{\partial \vec{A}}{\partial t} = -\vec{\nabla}\phi$, where the potential ϕ has been introduced since the magnetic induction \vec{B} is not changed by adding the gradient of a scalar function [10]. To describe an electron in an electromagnetic wave, ϕ is set to zero and the vector potential can be normalized to be $\vec{a} = e\vec{A}/\epsilon c^2$ [80]. However, some phenomena require a full quantum-mechanical description of light, where the electromagnetic field is quantized into modes which are associated with oscillators of fixed frequency [10]. Luckily, a semiclassical model of light is sufficient for this work. Thus, light is treated as an electromagnetic wave and only the interaction of light with matter is described in a quantum-mechanical manner by emission and absorption of quanta of energy and momentum.

An electromagnetic wave, like light, is characterized by three fundamental physical properties, namely the wavelength λ , the frequency ν , and the polarization state. These fundamental properties result in certain measurable physical properties, like intensity, energy, velocity of propagation, power, polarization, and momentum transport of light [10]. For this thesis, however, intensity and polarization are of special interest and will be considered in more detail.

The polarization is a property of the wave character of light and specifies the direction of

the electric field vector. While this direction varies during propagation for elliptically polarized light, the direction of the electric field vector remains constant for linear polarized light [10].

The Intensity I of a light wave is given by the absolute temporal average over a single optical period $\mathcal{T} = 2\pi/\omega$ of the Poynting vector $\vec{S} = \vec{E} \times \vec{H}$. In a homogeneous dielectric medium, the Poynting vector can be interpreted as the vector of energy transport as \vec{S} is the product of the energy density of an electromagnetic wave and the phase velocity of light in a homogeneous dielectric medium. The intensity I of light can also be seen as the energy dW , concentrated in the time interval dt and incident on an area A [10]:

$$\langle |\vec{S}| \rangle_t = I = \frac{dW}{A dt}. \quad (\text{A.2})$$

Consequently, the extreme intensities necessary for laser-plasma physics are reached if a large amount of energy is concentrated in a small time interval and area. A thermal radiator like a light bulb, however, is limited by the temperature T the emitter material can withstand as the intensity of a black-body radiator is given by $I \propto T^4$. Thus, it requires a laser (Light Amplification by Stimulated Emission of Radiation) to reach such high light intensities that a plasma is created from a solid. In comparison to the unpolarized and incoherent nature of thermal radiation, a laser is based on stimulated emission and therefore produces highly directional, coherent and polarized light. Such coherent light is defined by temporally constant phase differences between different points on the wavefront. During the process of stimulated emission, an atom or molecule in a higher energy state is stimulated by an incident photon to decay to the lower energy level by emitting a photon with the same properties as the incident photon, namely propagation direction, polarization, phase, and frequency. This amplification process takes place in the active medium which is located inside the optical resonator (two flat or spherical mirrors in front of each other) of the laser. Light amplification in a laser requires a pump to create a population inversion in the active medium, such that the population of the upper energy level is larger than that of the lower energy level [10].

A.1. Spatial Characteristics of High-Intensity Laser Pulses

To achieve the very high laser intensities that are needed for several interesting applications, like laser-based particle acceleration, light needs to be focused to a small area, as indicated by equation (Eq.) A.2. The spatial characteristics of a laser are governed by the geometry of the optical resonator and therefore the electric field of a laser beam is confined in two spatial dimensions. In most cases, a Gaussian beam is a good approximation of the spatial field distribution of a laser beam. For a cylinder-symmetric laser resonator, the intensity I of a monochromatic light wave leaving the resonator and propagating along the z -direction is given by

$$I(r, z) = I_0 \frac{w_0^2}{w^2(z)} \exp\left(-\frac{2r^2}{w^2(z)}\right), \quad \text{with } w^2(z) = w_0^2 \left[1 + \left(\frac{z}{z_R}\right)^2\right] \text{ and } z_R = \frac{\pi w_0^2}{\lambda}. \quad (\text{A.3})$$

Thus, the laser intensity falls off exponentially in radial direction with a rate of intensity drop which is determined by the beam radius $w(z)$. The smallest beam radius (i.e. the beam waist) w_0 lies at $z = 0$ inside the laser resonator and the beam divergence (increase of beam diameter) is characterized by the Rayleigh length z_R . Consequently, a reduced beam waist w_0 results in a strongly diverging beam as the Rayleigh length z_R becomes smaller and vice versa [10].

A lens or a curved mirror (with focal length f) does not modify the general spatial structure of a Gaussian laser beam (Eq. A.3) but rather the position z_0 and value of the beam waist $w_0 = w(z_0)$. Therefore, focusing the laser beam increases the peak intensity $I_0 = 2P_0/\pi w_0^2$ in the focal spot because w_0 is decreased by the focusing optics, whereas the total laser power P_0 remains unchanged. For now, it is sufficient to note that a small beam waist w_0 is related to a large divergence angle $\theta = w_0/z_R$ and therefore a large laser beam diameter on a sufficient large focusing optics is needed for reaching very small focal spot sizes. To circumvent imaging aberrations, parabolic mirrors are used to focus the laser beam to high intensities. Due to diffraction, an airy-pattern will be present in the focal plane instead of a Gaussian intensity distribution if the parabolic mirror is not sufficiently larger than the near field size of the laser beam. However, such a situation is usually avoided in practice and the laser field distribution in the focus is only influenced by spatial amplitude and phase front variations of the laser near field and misalignment of the parabolic mirror [10].

A.2. Temporal Characteristics of High-Intensity Laser Pulses

Simply confining the laser energy in two spatial dimension is not enough for achieving very high laser intensities. Instead, additionally confining the laser energy in time is necessary, as Eq. A.2 indicates. Consequently, a high-intensity laser should rather produce very short and intense laser pulses instead of operating in the continuous-wave (cw) regime. One distinguishes basically two types of techniques for generating short laser pulses: The technique of Q-switching produces short pulses by varying the losses in the laser resonator. First, a large inversion builds up due to high losses in the resonator. Then, the losses in the resonator are abruptly reduced to a low level and a short and intense laser pulse with a duration of a few nanoseconds forms. However, the mode-locking technique is needed to achieve laser pulses which are shorter than the cavity round-trip time. To do so, many longitudinal cavity modes of different wavelength are forced to oscillate with a certain phase relation. These modes coherently add up to a few-femtosecond pulse which consequently has a certain spectral width. Technically, mode-locking is achieved by actively or passively increasing the losses for long pulses whereas short pulses experience much lower losses and therefore are amplified. These short pulses then travel back and forth in the cavity while a small amount of laser light is coupled out at the less reflective mirror to produce a train of very short laser pulses [10].

For the mathematical description of the temporal characteristics of a laser pulse, one may imagine the situation of a small detector, fixed in space. Assuming a linearly polarized light wave, the electric field strength $E(t)$ can then be written as the product of a harmonic wave

and a amplitude envelope function $E_{\text{env.}}(t)$

$$E(t) = E_{\text{env.}}(t) \cos(\phi(t)) = E_{\text{env.}}(t) \cos(\omega_0 t + \phi_0 + \phi_a(t)) \quad (\text{A.4})$$

with an absolute phase ϕ_0 , the carrier angular frequency ω_0 , and the consequent laser frequency $\nu_0 = \frac{\omega_0}{2\pi}$. The additional time dependent phase $\phi_a(t)$ in Eq. A.4 accounts for variations of the laser frequency in time which are unavoidable in reality. Often, a Gaussian temporal envelope

$$E_{\text{env.}}(t) = E_0 \exp\left(-2 \ln 2 \left(\frac{t}{\Delta t}\right)^2\right), \quad (\text{A.5})$$

with amplitude E_0 and the temporal FWHM Δt of the corresponding intensity distribution $I(t) = \frac{\epsilon_0 c \eta}{2} E_{\text{env.}}^2(t)$, is assumed to approximate the temporal pulse shape of the laser. Here, η is the refractive index of the medium in which the laser pulse propagates. Further information on the spectral characteristics of the laser pulse can be acquired by applying the inverse Fourier transformation to $E(t)$

$$\tilde{E}(\omega) = \int_{-\infty}^{\infty} E(t) e^{-i\omega t} dt. \quad (\text{A.6})$$

As $E(t)$ is real, the frequency spectrum fulfills $\tilde{E}(\omega) = \tilde{E}^*(-\omega)$ where $*$ marks the complex conjugate. Hence, it is sufficient to consider the positive part $\tilde{E}^+(\omega)$ of the frequency spectrum only, which can be written as the product of an amplitude $|\tilde{E}(\omega)|$ and a spectral phase $\varphi(\omega)$

$$\tilde{E}^+(\omega) = |\tilde{E}^+(\omega)| e^{-i\varphi(\omega)}. \quad (\text{A.7})$$

Connected through the Fourier transform, the spectral and temporal laser pulse characteristics influence each other and the frequency spectrum of the laser pulse directly influences its temporal pulse shape and width. A simple measure of this mutual influence is the time-bandwidth product $\Delta t \Delta \nu$, namely the product of the FWHM of the temporal and the spectral intensity profile. For a Gaussian temporal envelope (Eq. A.5) for instance, the smallest possible time-bandwidth product is $\Delta t \Delta \nu = 0.441$. This limit makes directly clear that short laser pulses have a large spectral width $\Delta \nu$. Such a bandwidth-limited pulse can only be reached if $\phi(t)$ and $\varphi(\omega)$ are strictly linear functions of their argument. Mode locking, as described before, enforces such a fixed phase relation between the different frequency components of the laser pulse. As the spectrum is usually centered around the carrier frequency ω_0 , the spectral phase $\varphi(\omega)$ is expanded into a Taylor series to better understand the influence of the spectral phase on the temporal laser pulse shape:

$$\varphi(\omega) = \varphi(\omega_0) + \left. \frac{\partial \varphi(\omega)}{\partial \omega} \right|_{\omega_0} (\omega - \omega_0) + \frac{1}{2} \left. \frac{\partial^2 \varphi(\omega)}{\partial \omega^2} \right|_{\omega_0} (\omega - \omega_0)^2 + \frac{1}{6} \left. \frac{\partial^3 \varphi(\omega)}{\partial \omega^3} \right|_{\omega_0} (\omega - \omega_0)^3 + \dots \quad (\text{A.8})$$

The zeroth order in this Taylor expansion corresponds to the absolute phase ϕ_0 in time domain. Whereas the first-order term in Eq. A.8 leads only to a temporal shift of the pulse, the second-order term symmetrically broadens the laser pulse $E(t)$. Last but not least, the third-order term in the Taylor expansion of the spectral phase results in side-pulses on one side of

the main laser pulse in the temporal domain [10].

Real laser pulses deviate from the ideal Gaussian pulse shape given in Eq. A.5. In fact, the rising edge of the laser pulse on a picosecond timescale requires particular attention. The high intensities of $> 10^{18} \text{ W/cm}^2$ in the experiment are orders of magnitude above the onset of atom ionization and nonlinear effects. Thus, the rising pulse edge already ionizes the target. Consequently the rising pulse edge strongly determines the plasma configuration which the main pulse experiences. The pre-pulse pedestal contains contributions of amplified spontaneous emission (ASE), amplified leaking pulses and uncompensated spectral phase modulations. Several methods are nowadays established to increase the temporal intensity contrast (TIC), i.e., the intensity ratio of the main pulse to the pre-pulse pedestal, to prevent the destruction of the target before the arrival of the main laser pulse. However, to create a plasma and reach such high intensities of $> 10^{18} \text{ W/cm}^2$ in the experiment, the femtosecond laser pulses from the laser oscillator need to be amplified. A short description of the successive laser pulse amplification is given in the next section [10].

A.3. Chirped Pulse Amplification

Equipped with femtosecond pulses from a laser oscillator, it is still necessary to amplify these pulses further to increase the pulse energy for reaching the intensities needed for particle acceleration. However, laser damage, nonlinear effects and efficient amplification limited the achievable peak power for a long time [10]. Only the invention of chirped pulse amplification (CPA) technique [11] allowed to reach relativistic intensities of $\geq 10^{18} \text{ W/cm}^2$. The basic principle of CPA consists of three steps: First, the ultrashort laser pulse is stretched by adding second-order phase shift to $\varphi(\omega)$ (see Eq. A.8). This is usually done via reflective gratings and different path lengths for the different frequency components of the laser pulse spectrum. In the second step, the temporally broadened laser pulse is successively amplified. Last, the phase shift from step one is added to the amplified pulse but now with the opposite sign. In such a way, the chirp from the first step is compensated. Hence, a compressed and amplified laser pulse of short duration and high intensity is achieved [10]. As an example of a CPA laser system, the POLARIS laser¹, where all experiments of this thesis have been carried out, is schematically drawn in figure A.1.

¹https://www.hi-jena.de/de/helmholtz_institute_jena/ueber-das-helmholtz-institut-jena/experimental_facilities/local/polaris/

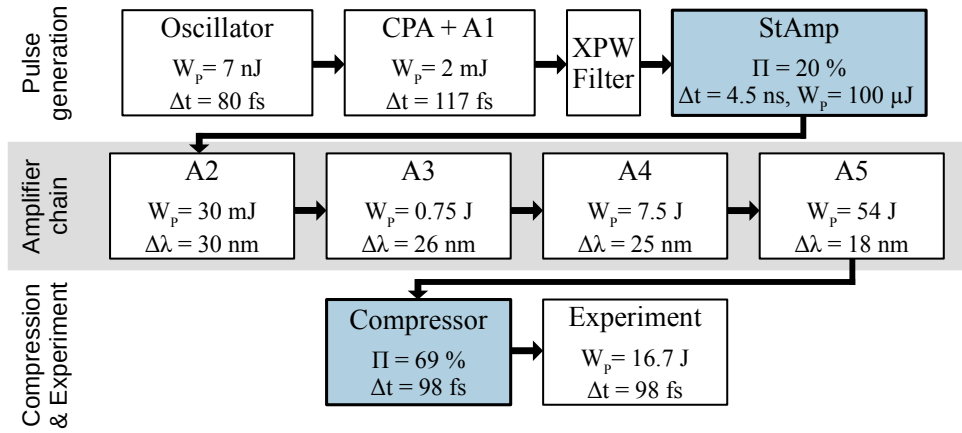


Figure A.1.: Schematic drawing of the POLARIS laser beam line. First, the ultrashort laser pulses are created in a Ti:Sa oscillator (active medium is a titanium-sapphire crystal). Next, the pulses are stretched, amplified in the first amplifier (A1) and compressed again to be passed to a XPW (non-linear) filter for increasing the temporal intensity contrast. After pulse cleaning, the pulses are stretched and amplified in the StAmp [188]. The stretched pulses are then successively amplified in the amplifiers A2, A3, A4, and A5. Finally, the laser pulses are compressed again and passed to the experiment chamber. For the different modules, the output pulse energy is specified as W_p , the pulse duration (FWHM) as Δt , the spectral width (FWHM) as $\Delta\lambda$ and the efficiency as Π . The specified W_p and Δt correspond to the best achieved performance with POLARIS so far [160] which is slightly better than what is achieved on a daily basis. Figure taken in a modified form from [189, 190].

B. A Brief Description of Coherent Wake Emission

When a bunch of fast electrons traverses the plasma-vacuum boundary at the target rear side, it creates an electric field which accelerates thermal plasma electrons at the target rear side inwards towards the increasing plasma density. Those inward accelerated thermal electrons excite electron plasma oscillations at the local plasma frequency $\omega_p(x)$ along their way through the target rear side plasma density gradient [83]. Those initially longitudinal plasma oscillations acquire a transverse oscillation component as their wavefronts curve in time due to the plasma density gradient. This newly acquired transverse plasma oscillation component allows the radiation of electromagnetic waves [191]. Hence, the radiation with frequency $\omega_p(x)$ from plasma oscillations at different positions x in the wake of the inward accelerated thermal electrons add up to result in an attosecond pulse. This light emission mechanism is called coherent wake emission (CWE) [62, 82, 83, 191]. The fast electrons may set up the accelerating electric field, but the CWE is caused by the inward accelerated thermal electrons due to phase-matching reasons [83]. As usually not only one but several electron bunches, periodically spaced in time, traverse the plasma-vacuum boundary at the target rear side, each bunch produces CWE and the radiation of this attosecond pulse train interferes. The resulting spectrum $E(\omega) = \sum_n a(n) A(\omega) \exp(i\omega t_{em}(n))$ depends on the amplitude $a(n)$ and the emission time $t_{em}(n)$ of the attosecond pulse from the n th laser cycle, as well as the spectral amplitude $A(\omega)$ of an individual attosecond pulse [192].

CWE is emitted along the same direction and with the same polarization as the incident laser light [62, 82]. Moreover, it is important to note that CWE is more efficient at gentle plasma density gradients, in contrast to CTR which is more efficient for a step-like plasma-vacuum interface [83]. Due to limited speed of heat transfer from the target front to the rear side, thicker targets (several hundreds of nm and more as present in this thesis) are expected to have a steeper plasma density gradient at the target rear side [193]. The velocity of the fast electrons plays only a minor role in CWE whereas CTR becomes increasingly efficient at relativistic velocities [83]. All together, this makes CWE a less probable explanation for the COR observed in the experiments of this thesis.

C. Exemplary Calculated CTR Spectra

If a relativistic laser pulse is focused on a thin foil, hot (i.e. energetic) electrons are periodically accelerated in the laser field at the foil front side and emit coherent optical radiation (CTR or CSR) at the foil rear side. In section 2.5.3.1, a CTR model has been introduced to study the influence of the energy and temporal distribution of the hot electron current on the emitted radiation. Due to the similarity of CSR and CTR, it can be safely expected that the influences of the hot electron distribution on the CTR spectrum hold also approximately true for CSR.

Using the CTR model described in section 2.5.3.1, an exemplary CTR spectrum has been plotted in Fig. 2.6 for typical parameters of the experiments presented in this thesis. Due to the presence of different laser absorption mechanisms (see section 2.3), the hot electron current is composed of a series of periodically spaced bunches where n_b electron bunches have been accelerated at ω_L and $2n_b$ electron bunches have been accelerated at $2\omega_L$. In Fig. 2.6, the calculated CTR spectrum is plotted for an exemplary value of $n_b = 20$. To illustrate the contribution of the two different electron populations, namely hot electrons accelerated at ω_L and hot electrons accelerated at $2\omega_L$, the spectra of the CTR emitted by these two different electron populations are plotted separately in Fig. C.1. The temporal hot electron distribution at the target front side and target rear side and the corresponding CTR spectrum is shown for $n_n = 20$ hot electron bunches accelerated at ω_L in Fig. C.1a and for $n_n = 40$ hot electron bunches accelerated at $2\omega_L$ in Fig. C.1b.

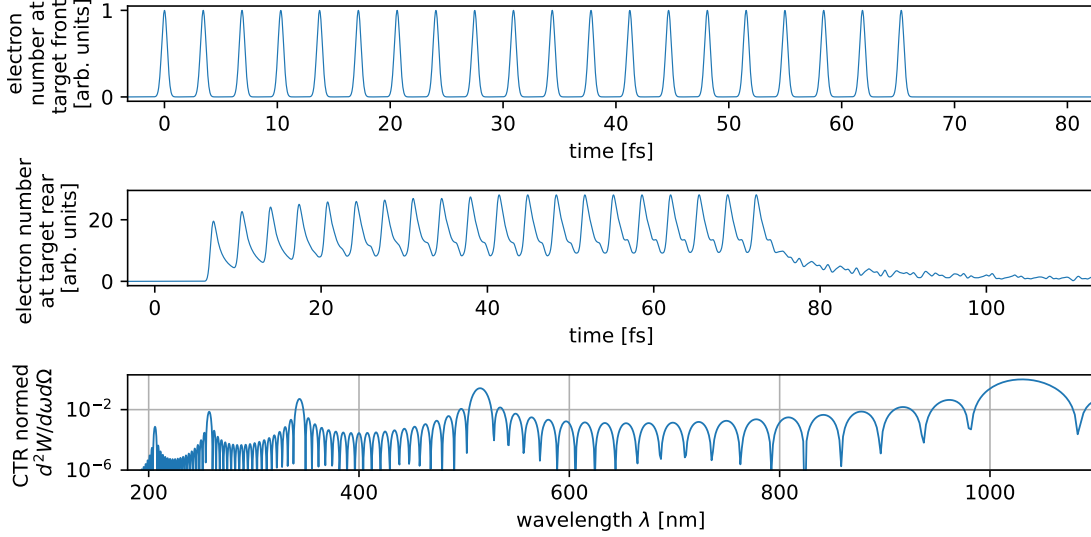
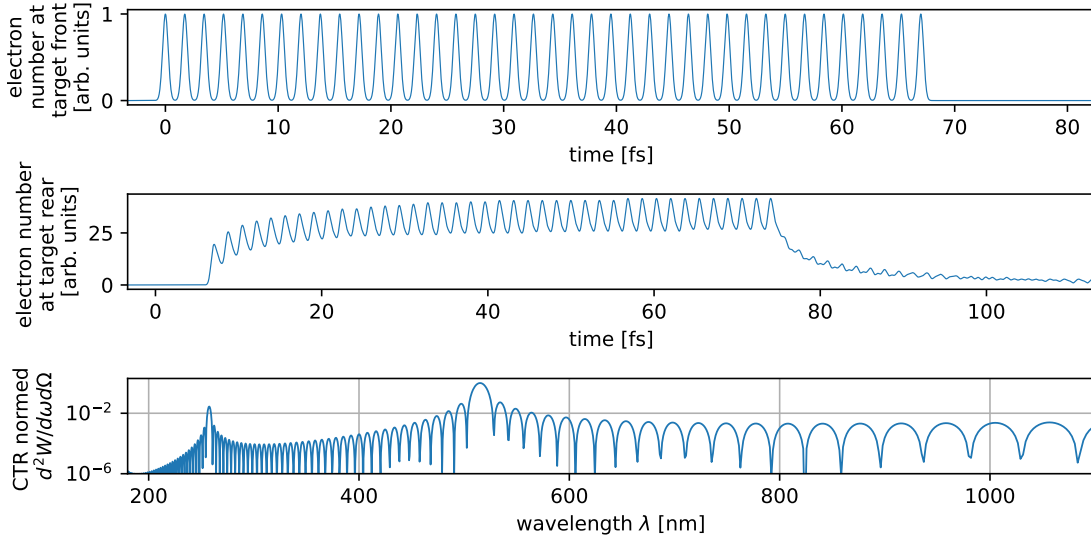

 (a) 20 hot electron bunches spaced at \mathcal{T}_L ($P_1 = 1$ and $P_2 = 0$).

 (b) 40 hot electron bunches spaced at $\mathcal{T}_L/2$ ($P_1 = 0$ and $P_2 = 1$).

Figure C.1.: Plots, based on the CTR model presented in section 2.5.3.1, which depict the temporal hot electron distribution at the target front side and target rear side together with the corresponding CTR spectrum for an exemplary hot electron distribution. The hot electron distribution at the target front side (upper subplot) as a function of time is acquired from $h(\vec{r}_\perp, t, \vec{u})$ by neglecting all terms depending on \vec{r}_\perp and \vec{u} and setting $d_0 = 0$. The hot electron distribution at the target rear side (middle subplot) is calculated by numerically evaluating the integral $\int d^3 \vec{u} h(\vec{r}_\perp, t, \vec{u})$. The normalized differential CTR energy (lower subplot) is calculated from Eq. 2.41 with the substitution from Eq. 2.43 for typical experimental parameters of this thesis, namely $T_h = 0.4 \text{ MeV}$, $d_0 = 2 \mu\text{m}$ and $\sigma_t = \mathcal{T}_L / (10 \cdot \sqrt{2}) = 0.243 \text{ fs}$ (as proposed in [70] based on PIC results and fits to experimental data). In the two subfigures, different temporal hot electron distributions are considered as specified in the subfigure headings. For simplification, only one spatial dimension is considered by setting $\vec{r}_\perp = 0$. Analogous to the geometry in the experiments of this thesis, the CTR is calculated for $\theta = 37^\circ$ and $\alpha = 90^\circ$ (see Fig. 2.2). Moreover, it is assumed that the electrons propagate normal to the target rear side ($\phi = 90^\circ$, $\psi = 0^\circ$) with no divergence (see Eq. 2.32).

D. Calculations of Polarization Characteristics of COR

D.1. Simulation Model

In the sections 4.2 and 4.3, the discussion of coherence effects required the assumption of a laminar hot electron current with no divergence which is directed normal to the target rear surface ($\psi = 0$ in coordinate system of Fig. 2.2). This approximation was justified because the spectrum of COR is expected to be mainly influenced by the temporal structure of the hot electron current. Any divergence of the hot electron current would only result in a slight reduction in coherence, which in turn results in a stronger spectral intensity decrease of COR towards shorter wavelengths. Nevertheless, the polarization characteristics of the imaged rear surface COR emission spot are influenced by the spatial and angular distribution as well as the energy of the hot electron current. Therefore, these parameters need to be taken adequately into account when calculating the polarization characteristics of the imaged COR emission spot. With the computational capabilities at hand, it was, however, not feasible to fully simulate the COR emitted by a diverging hot electron current as already mentioned in section 2.5.3. Therefore, a much simpler model is suggested in the following. As before, the coordinate system as defined in Fig. 2.2 is used.

D.1.1. Hot Electron Distribution Function

To reduce the complexity and hence the computational time of the COR model, the number of integrals in Eq. 2.25 (and hence Eq. 2.30) and Eq. 2.45, which have to be evaluated numerically, needs to be reduced. Therefore, the temporal structure of the hot electron current and any coherence effects related to that are neglected and only aspects of relevance to the simulation of the polarization characteristics of COR are considered.

The COR model of this section assumes a single, **infinitesimal thin**, **monoenergetic** hot electron sheet with a Gaussian **transverse spatial** distribution. Consequently, the hot electron distribution function (at the target rear surface) is given as

$$h(\vec{r}_\perp, t, \vec{u}) = Cf(\phi, \psi) \delta(|\vec{u}| - u_T) \delta\left(t - \frac{d_0}{\beta c \cos \psi}\right) \exp\left(-\frac{|\vec{r}_\perp - \vec{v}_\perp t|^2}{2\sigma_r^2}\right), \quad (\text{D.1})$$

with the transverse position $\vec{r}_\perp = (x, y)^T$, the transverse velocity $\vec{v}_\perp = (v_x, v_y)^T$, the Dirac delta function $\delta(x)$, and the fixed absolute normalized momentum $u_T = \gamma_T \beta_T$ of the monoenergetic electron sheet, where $\gamma_T = (k_B T_h / m_e c^2) + 1$. To consider a diverging hot electron current

($\sigma_\psi \neq 0$), a Gaussian angular distribution centered around zero is used as a first approximation of the angular velocity distribution of the hot electrons, thus

$$f(\phi, \psi) = f(\psi) = \exp\left(-\psi^2/2\sigma_\psi^2\right). \quad (\text{D.2})$$

Consequently, the total emitted energy per unit angular frequency ω , solid angle Ω and area (on the target rear surface) is calculated in this model from

$$\begin{aligned} \left. \frac{d^2 W}{d\omega d\Omega dx dy} \right|_{\text{CTR}} &= \frac{e^2 N(N-1)}{4\pi^3 \epsilon_0 c} \left(\left| \int d^3 \vec{u} \int_{-\infty}^{\infty} dt E_{\parallel} e^{i(\omega t - \vec{k}_{\perp} \cdot \vec{r}_{\perp})} h(\vec{r}_{\perp}, t, \vec{u}) \right|^2 \right. \\ &\quad \left. + \left| \int d^3 \vec{u} \int_{-\infty}^{\infty} dt E_{\perp} e^{i(\omega t - \vec{k}_{\perp} \cdot \vec{r}_{\perp})} h(\vec{r}_{\perp}, t, \vec{u}) \right|^2 \right), \end{aligned} \quad (\text{D.3})$$

for TR and from

$$\left. \frac{d^2 W}{d\omega d\Omega dx dy} \right|_{\text{CSR}} = \frac{e^2 N(N-1)}{16\pi^3 \epsilon_0 c} \left| \int d^3 \vec{u} \int_{-\infty}^{\infty} dt \vec{E}_{\text{SR}}(\omega, \Omega, \vec{u}) e^{i(\omega t - \vec{k}_{\perp} \cdot \vec{r}_{\perp})} h(\vec{r}_{\perp}, t, \vec{u}) \right|^2, \quad (\text{D.4})$$

$$\text{with } \vec{E}_{\text{SR}}(\omega, \Omega, \vec{u}) = \int_{t_1}^{t_2} dt' \frac{\vec{n} \times \left[(\vec{n} - \vec{\beta}(t')) \times \dot{\vec{\beta}}(t') \right]}{(1 - \vec{n} \cdot \vec{\beta}(t'))^2} e^{i\omega[t' - \vec{n} \cdot \vec{r}(t')/c]}, \quad (\text{D.5})$$

for SR. The electric fields E_{\parallel} and E_{\perp} for TR are calculated using Eq. 2.26 and Eq. 2.27. Usually, $t_1 = -\infty$ and $t_2 = \infty$ are chosen in Eq. D.5 to calculate the electric field of SR as the integrand is only nonzero for times t where $\dot{\vec{\beta}}(t) \neq 0$ (i.e. only at times when the electron is accelerated and therefore emits SR). The phase factor $e^{i(\omega t - \vec{k}_{\perp} \cdot \vec{r}_{\perp})}$ takes into account that different electrons arrive at different times and positions at the target rear surface and therefore their phase differs. For the chosen coordinate system (see Fig. 2.2), the transverse wave vector $\vec{k}_{\perp} = (k_x, k_y)^T$ depends on the angles α and θ .

Strictly speaking, SR is emitted over the whole trajectory $\vec{r}(t')$ of a hot electron at the target rear surface. Taking this into account lies, however, beyond the scope of this work. Instead, the total SR emitted along the trajectory $\vec{r}(t')$ of an hot electron is approximated to have been emitted at only one point \vec{r}_{\perp} . As the radiation cone of the electron points only for a small part of the electron trajectory towards the microscope objective, most of the radiation collected by the microscope objective was emitted inside a small spatial region. This simplifies the calculation of SR because the total emitted CSR energy can be numerically calculated in two steps. First, the electric field strength of SR (see Eq. D.5) is calculated for a specific trajectory $\vec{r}(t')$ for a single electron. In the next step, the calculated electric field strength at the target rear surface is added (in the calculation the integrals are transformed to sums) to the total CSR electric field strength only at the position \vec{r}_{\perp} where the electron arrived at the target rear surface. However, one should keep in mind that this is a coarse approximation which limits the meaningfulness of the calculated CSR polarization characteristics but was however necessary to limit the computation time to feasible values. If this two-step approximation is not used, the order of the integrals in Eq. D.4 needs to be slightly changed and \vec{E}_{SR} additionally also depends on \vec{r}_{\perp} which slows down the calculations. For a quantitative discussion of the polarization characteristics of CSR, a detailed model with much less simplifications,

implemented for parallelized calculation on a big computer cluster, should be used instead.

Due to the chosen hot electron distribution function in Eq. D.1, the integrals over t and u in Eq. D.3 and Eq. D.4 can be easily evaluated analytically. The total emitted energy per unit angular frequency ω , solid angle Ω and area (on the target rear surface) therefore is given as

$$\left. \frac{d^2 W}{d\omega d\Omega dx dy} \right|_{\text{CTR}} = \frac{e^2 N(N-1)}{4\pi^3 \epsilon_0 c} \left(\left| \int_0^{2\pi} d\phi \int_0^{\pi/2} d\psi u_T^2 \sin \psi E_{\parallel} e^{i\Lambda} h(\vec{r}_{\perp}, \psi, \phi) \right|^2 + \left| \int_0^{2\pi} d\phi \int_0^{\pi/2} d\psi u_T^2 \sin \psi E_{\perp} e^{i\Lambda} h(\vec{r}_{\perp}, \psi, \phi) \right|^2 \right), \quad (\text{D.6})$$

for TR and as

$$\left. \frac{d^2 W}{d\omega d\Omega dx dy} \right|_{\text{CSR}} = \frac{e^2 N(N-1)}{16\pi^3 \epsilon_0 c} \left| \int_0^{2\pi} d\phi \int_0^{\pi/2} d\psi u_T^2 \sin \psi \vec{E}_{\text{SR}}(\omega, \Omega, u_T, \psi, \phi) e^{i\Lambda} h(\vec{r}_{\perp}, \psi, \phi) \right|^2, \quad (\text{D.7})$$

for SR, with $\vec{E}_{\text{SR}}(\omega, \Omega, u_T, \psi, \phi)$ as defined in Eq. D.5 and the phase term

$$\Lambda = \omega \frac{d_0}{\beta_T c \cos \psi} - \vec{k}_{\perp} \cdot \vec{r}_{\perp}. \quad (\text{D.8})$$

Moreover, the reduced hot electron distribution

$$h(\vec{r}_{\perp}, \psi, \phi) = C \exp\left(-\psi^2 / 2\sigma_{\psi}^2\right) \exp\left(-\frac{(x - d_0 \tan(\psi) \cos(\phi))^2 + (y - d_0 \tan(\psi) \sin(\phi))^2}{2\sigma_r^2}\right) \quad (\text{D.9})$$

is used in the above equations. As only hot electrons flying in forward direction are considered, the upper limit of the integral over ψ is reduced to $\pi/2$ in Eq. D.6 and Eq. D.7.

D.1.2. Electron Trajectory Model for SR

After traversing the target rear surface, the electron is assumed to be accelerated back to the target due to the electric sheath field and magnetic fields induced by the return current at the target rear side. This phenomenon is called "fountain effect" [134, 135]. For simplicity, this trajectory is approximated as an arc. The length of the trajectory (i.e. the arc length) depends on the initial polar angle ψ at the moment when the electron traverses the target rear surface as illustrated in Fig. D.1.

In the presented model, it is assumed that the electrons are only accelerated and therefore emit SR outside of the target at the target rear side. Moreover, the hot electrons are assumed to recirculate only once. These assumptions need to be included in the formula for the acceleration $\dot{\beta}(t')$. Instead, however, the integral limits in Eq. D.5 are chosen as

$$t_1 = 0, \quad t_2 = \frac{\pi - 2\psi_0}{c\beta/\rho}, \quad (\text{D.10})$$

with the electron trajectory radius ρ , to resemble that a hot electron only emits SR when it is

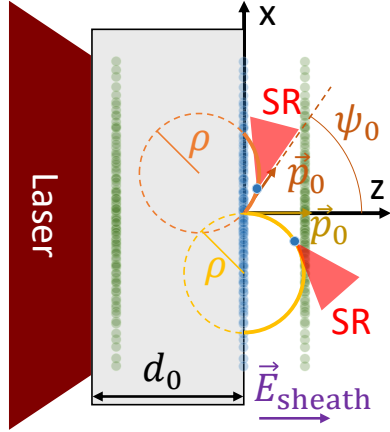


Figure D.1.: A schematic cross section of the laser-solid interaction (as sketched in Fig. 2.2 and Fig. 2.5) with the parameters of the CSR model presented in the text. The laser is incident from the left on the target (indicated as a gray rectangle) and accelerates electrons to the target rear side. Due to the electric sheath field and magnetic fields induced by the return current at the target rear side, the electrons are accelerated back to the target on a curved trajectory ("fountain effect" [134, 135]) which is approximated as a circle. Due to this acceleration, the electrons emit SR in a cone along their momentary velocity vector. As shown for two electrons (indicated in orange and yellow), the arc length of the circle in vacuum depends on the initial polar angle ψ_0 at the time $t' = 0$ when the electron traverses the rear target surface. The radius ρ of the trajectories, the electron bunch size and the target thickness is roughly to scale for $d_0 = 400$ nm. Moreover, no divergence (i.e. $\sigma_\psi = 0$) is considered for the schematic drawing of the electron bunch shape to improve the clarity of the drawing.

accelerated in the electric sheath field outside of the target. Nevertheless, the definitions in Eq. D.10 are only meaningful if a particle trajectory $\vec{r}(t')$ is specified. An electron is defined to traverse the target rear surface at $t' = 0$. For a circular trajectory in the coordinate system defined in Fig. 2.2, the polar angle of the momentum (and hence velocity) vector is given as

$$\psi(t') = \psi_0 + \beta t' / \rho, \quad (\text{D.11})$$

whereas the azimuthal angle is constant, thus $\phi(t') = \phi_0$. Taking these initial conditions into account, the circular electron trajectory $\vec{r}(t')$ is obtained via integrating the electron velocity $\vec{\beta}(t')$ once, thus

$$\vec{r}(t') = \rho \begin{pmatrix} \cos \phi_0 (\cos \psi_0 - \cos \psi(t')) \\ \sin \phi_0 (\cos \psi_0 - \cos \psi(t')) \\ \sin \psi(t') - \sin \psi_0 \end{pmatrix}. \quad (\text{D.12})$$

Two such circular electron trajectories are sketched in Fig. D.1 as an example.

Analogous to section 2.5.1, the radius ρ of the circular electron trajectory is approximated as the target rear side Debye length, hence $\rho \approx \lambda_{D, \text{rear}}$. In [128] and in section 2.5.1, the ponderomotive hot electron temperature (see Eq. 2.12) has been used to calculate $\lambda_{D, \text{rear}}$. In the current section, however, the hot electron temperature scaling by T. KLUGE *et al.* [113] (see Eq. 2.13) is used. Inspired by [128], the transverse electron beam size increase due to divergence is modeled as

$$r_{\text{rear}} = r_0 + d_0 \tan(\Delta_\psi), \quad (\text{D.13})$$

with the initial hot electron beam radius $r_0 = \sqrt{2 \ln 2} \sigma_r$ at the target front surface and the Half Width at Half Maximum (HWHM) $\Delta_\psi = \sqrt{2 \ln 2} \sigma_\psi$ of the angular hot electron momentum distribution $f(\psi)$ (Eq. D.2). Next, the electron density $n_{e,0}$ at the target rear surface is approximated using the laser energy density in the focal spot, the fraction $\Pi_{L \rightarrow e}$ of absorbed

laser energy by the hot electrons, the hot electron current size at the target rear side (see Eq. D.13), and the energy $k_B T_h$ of a single hot electron. Consequently,

$$n_{e,0} = \frac{\Pi_{L \rightarrow e} W_L}{c \tau_L \pi (r_0 + d_0 \tan(\Delta_\psi))^2} \frac{1}{k_B T_h}, \quad (D.14)$$

where W_L is the laser pulse energy and τ_L is the laser pulse width. Here, $\Pi_{L \rightarrow e} = 0.25$ is chosen as an approximation because this value lies in the middle of the range of published investigations on quantifying $\Pi_{L \rightarrow e}$ [59, 185–187]. Hence, . Inserting Eq. D.14 into Eq. 2.4 then gives the Debye length, and hence the electron trajectory radius ($\rho \approx \lambda_{D, \text{rear}}$), at the target rear surface

$$\lambda_{D, \text{rear}} = \sqrt{\frac{\epsilon_0 c (k_B T_h)^2}{e^2 \Pi_{L \rightarrow e} I_L r_0^2 / (r_0 + d_0 \tan \Delta_\psi)^2}}, \quad (D.15)$$

with the hot electron temperature T_h calculated from Eq. 2.13 and the laser intensity $I_L = W_L / \tau_L \pi r_0^2$.

D.1.3. Acceptance Cone of Microscope Objective

As mentioned before, only the aspects of relevance to the simulation of the polarization characteristics of COR are considered. With the chosen electron distribution function in Eq. D.1 and Eq. D.2, the emitted COR is calculated from the average over ψ and ϕ and the number of integrals which have to be evaluated numerically is drastically reduced. In that way, the computational time of the plots presented in section D.2 is limited to a maximum of ten days (on a standard computer). As the microscope objective used to image COR (see Fig. 3.1) has an acceptance angle of roughly 30.2° , it is not sufficient to consider only one observation direction ($\theta = 37^\circ$ and $\alpha = 90^\circ$). The acceptance angle is defined with respect to the optical axis of the microscope objective and therefore can be imagined as a cone. The tip of this acceptance cone is placed at the object and the cone opens itself towards the microscope objective. All the COR from one point on the target rear surface with a wave vector \vec{k} inside this acceptance cone of the microscope objective is imaged onto the same position on the camera [10]. Hence, one needs to average the calculated COR energy over the acceptance cone Ω_{obj} of the microscope objective. To define the angles which lie inside the acceptance cone of the microscope objective, it is convenient to define a rotated coordinate system S' as illustrate in Fig. D.2. In the coordinate system S' , wave vectors \vec{k}' which fulfill $\theta' \leq 15.1^\circ$ lie inside the acceptance cone of the microscope objective. Hence, the averaging over the acceptance cone is done via averaging over $\alpha' \in [0^\circ, 360^\circ)$ and $\theta' \in [0^\circ, 15.1^\circ]$. The wave vectors \vec{k} , and hence the angles θ and α needed for the COR model evaluation, are obtained by rotating the \vec{k}' vectors by -37° (i.e. a clockwise rotation by 37°) around the x-axis.

D.1.4. Numerical Evaluation and Parameters

The temporal integral in Eq. D.5 are evaluated using the composite Simpson's rule [194] with a sufficient fine discretization of t' . All integrals in Eq. D.6 and Eq. D.7 are transformed to sums to be able to evaluate them numerically. To limit the computational time, a coarse

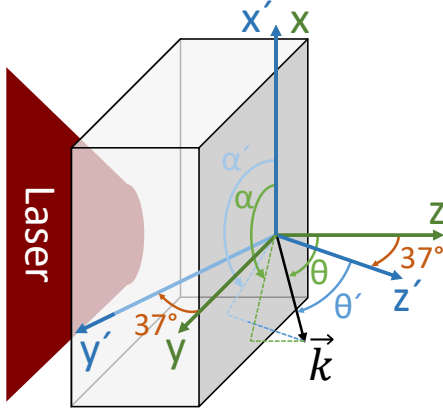


Figure D.2.: A schematic drawing of the laser-solid interaction with coordinate system S and S' . The target (e.g. a thin aluminum foil) and its orientation is indicated as a gray plate. The laser is incident from the left on the target front side. An exemplary wave vector \vec{k} of COR is illustrated as a black arrow. In coordinate system S (the one from Fig. 2.2), the z -axis is parallel to the target rear surface normal. The coordinate system S' is rotated by -37° around the x -axis with respect to coordinate system S . In S' , the z' -axis is parallel to the optical axis of the microscope objective which is used in the experiment to image COR. The acceptance cone of the microscope objective is given as $\theta' \leq 15.1^\circ$.

discretization (i.e. large spacings ϑ between the grid points) of the angles α', θ', ϕ , and ψ has to be used. The error of the composite Simpson's rule is of the order $\mathcal{O}(\vartheta^4)$. Hence it seems more reasonable for large ϑ , to use the composite trapezoidal rule [194] for numerical integration whose error is of order $\mathcal{O}(\vartheta^2)$. The Simpson's rule uses a polynomial of order 2 to interpolate the function, which is to be integrated, between the grid points. The trapezoidal rule, on the other hand, uses a polynomial of order 1. Using the composite trapezoidal rule, an integral is transformed to a sum in the following way:

$$\int_a^b f(x) dx = w_i \sum_{i=1}^M f(x_i), \quad \text{with } w_i = \begin{cases} \vartheta_x/2 & i \in \{1, M\} \\ \vartheta_x & \text{else} \end{cases}, \quad (\text{D.16})$$

where M is the number of grid points x_i and $\vartheta_x = \frac{b-a}{M-1}$ is the spacing between the grid points x_i .

Applying the composite trapezoidal rule to Eq. D.6 and Eq. D.7 and taking the averaging over the acceptance cone $\Omega_{\text{obj.}}$ of the microscope objective into account, the total emitted energy per unit angular frequency ω , solid angle Ω and area (on the target rear surface) is calculated from

$$\begin{aligned} \left. \frac{d^2 W}{d\omega d\Omega dx dy} \right|_{\text{CTR}} &= \frac{e^2 N(N-1)}{4\pi^3 \epsilon_0 c} (|E_S(x, y)|^2 + |E_P(x, y)|^2) \\ &\approx \frac{e^2 N(N-1)}{4\pi^3 \epsilon_0 c} \left(\left| \sum_{j=1}^{M_{\alpha'}} \sum_{l=1}^{M_{\theta'}} \sum_{m=1}^{M_{\phi}} \sum_{n=1}^{M_{\psi}} E_{\parallel, j, l, m, n} f_{j, l, m, n} \right|^2 \right. \\ &\quad \left. + \left| \sum_{j=1}^{M_{\alpha'}} \sum_{l=1}^{M_{\theta'}} \sum_{m=1}^{M_{\phi}} \sum_{n=1}^{M_{\psi}} E_{\perp, j, l, m, n} f_{j, l, m, n} \right|^2 \right), \end{aligned} \quad (\text{D.17})$$

for CTR and from

$$\begin{aligned} \left. \frac{d^2 W}{d\omega d\Omega dx dy} \right|_{\text{CSR}} &= \frac{e^2 N(N-1)}{16\pi^3 \epsilon_0 c} (|E_S(x, y)|^2 + |E_P(x, y)|^2) \\ &\approx \frac{e^2 N(N-1)}{4\pi^3 \epsilon_0 c} \left| \sum_{j=1}^{M_{\alpha'}} \sum_{l=1}^{M_{\theta'}} \sum_{m=1}^{M_{\phi}} \sum_{n=1}^{M_{\psi}} \vec{E}_{\text{SR}, j, l, m, n} f_{j, l, m, n} \right|^2, \end{aligned} \quad (\text{D.18})$$

for CSR. Here, the matrix elements $f_{j, l, m, n}$ are defined as

$$f_{j, l, m, n} = w_j w_l w_m w_n u_T^2 \sin \psi_n k^2 \sin \theta'_l \exp(i\Lambda_{j, l, n}) h_{m, n}, \quad (\text{D.19})$$

where $h_{m, n} = h(\vec{r}_{\perp}, \phi_m, \psi_n)$. Moreover, $\vec{E}_{\text{SR}, j, l, m, n} = \vec{E}_{\text{SR}}(\omega, \Omega_{j, l}, u_T, \phi_m, \psi_n)$ is calculated from Eq. D.5. The electric field strengths of TR, namely $E_{\parallel, j, l, m, n} = E_{\parallel}(\alpha_j, \theta_l, \phi_m, \psi_n, u_T)$ and $E_{\perp, j, l, m, n} = E_{\perp}(\alpha_j, \theta_l, \phi_m, \psi_n, u_T)$, are calculated from Eq. 2.26 and Eq. 2.27. The sums cover the range of $\alpha'_j \in [0^\circ, 360^\circ]$, $\theta'_l \in [0^\circ, 15.1^\circ]$, $\phi_m \in [0^\circ, 360^\circ]$, and $\psi_n \in [0^\circ, 90^\circ]$. Hence, the following spacings have been used, namely

$$\mathfrak{d}_{\alpha'} = \frac{2\pi}{M_{\alpha'} - 1}, \quad \mathfrak{d}_{\theta'} = \frac{\pi \cdot 15.1 / 180}{M_{\theta'} - 1}, \quad \mathfrak{d}_{\phi} = \frac{2\pi}{M_{\phi} - 1}, \quad \text{and} \quad \mathfrak{d}_{\psi} = \frac{\pi / 2}{M_{\psi} - 1}. \quad (\text{D.20})$$

With the spacings \mathfrak{d} at hand, the weights w_j , w_l , w_n , and w_m can be calculated from Eq. D.16. In the above equations, approximation signs have been used instead of equal signs to signify that the numerical evaluation of the integrals using sums is in practice only an approximation. Furthermore, the normalization constant C in Eq. D.9 is calculated from

$$1 = \sum_{j=1}^{M_{\alpha'}} \sum_{l=1}^{M_{\theta'}} \sum_{m=1}^{M_{\phi}} \sum_{n=1}^{M_{\psi}} w_j w_l w_n w_m u_T^2 \sin \psi_n k^2 \sin \theta'_l h_{m, n}. \quad (\text{D.21})$$

The total electric field strengths $E_S = \sum_{x, y} E_S(x, y)$ and $E_P = \sum_{x, y} E_P(x, y)$ need to be calculated for a comparison to the polarization characteristics of COR measured in the experiment (see Fig. 4.10). To do so, the electric field vectors of CSR and CTR, calculated for every j , l , m and n , need to be projected onto the axes for S- and P-polarization as defined by the experimental setup. The P-polarization axis lies in the yz-plane and is perpendicular to $\vec{k}(\alpha = 90^\circ, \theta = 37^\circ)$, for the coordinate system defined in Fig. 2.2. The S-polarization axis is parallel to the x-axis. To limit the computational time of these simulations which are presented in section D.2, discretization steps of 5° have been chosen for all angles. The xy-plane is discretized using a resolution of $\mathfrak{d}_x = \mathfrak{d}_y = 50 \text{ nm}$. Moreover, the computational x- and y-axis range from $-2r_{\text{rear}}$ to $2r_{\text{rear}}$ (see Eq. D.13).

Finally, one should note that imaging of COR at an angle of 37° , as implemented in the experimental setup, is not fully taken into account in the presented model. For simplification, the radiation collected by the microscope objective is calculated as a function of the rear surface position \vec{r}_{\perp} but the process of imaging this radiation at oblique angle is not considered.

Important Note The model presented in this section makes a lot of assumptions to limit the computational time to feasible values. Therefore, the calculations performed with this model, which are presented in the next section, are of limited significance. Instead, these computational results are rather meant to serve as a demonstration of the opportunities and capabilities that the COR simulations provide to interpret the experimental results and to draw conclusions on the angular velocity distribution and the size of the hot electron current. Hence, all the conclusions presented in the next section are preliminary. A conclusive discussion and interpretation of the polarization characteristics observed in the experiment needs a more detailed and accurate COR model.

D.2. Results of Simulations and Comparison to Experiment

The polarization ratio E_S/E_P of the measured COR changes with target thickness, laser intensity, and the COR's source size, as shown in Fig. 4.10. To link these changes in the polarization of the measured COR to characteristics of the hot electron current, the polarization ratio E_S/E_P has been calculated using the COR model introduced in the last section. This COR model depends mainly on the target thickness d_0 , hot electron divergence Δ_ψ , temperature T_h and initial size $r_0 = \sqrt{2\ln 2}\sigma_r$ of the hot electron current. Therefore, the polarization ratio E_S/E_P has been calculated for different values of d_0 , T_h , r_0 and Δ_ψ at $\lambda = 515$ nm. The results of these calculations are depicted in Fig. D.3, where E_S/E_P is plotted as a function of Δ_ψ for a few different model parameter combinations. In comparison to the experimental investigations, the COR calculations use the hot electron beam radius at the target front surface as a parameter. To get a quick estimate of the hot electron beam radius r_{rear} (and hence the COR emission spot size) at the target rear surface for different Δ_ψ , Eq. D.13 is used to display the hot electron beam diameter $2r_{\text{rear}}$ as the upper horizontal axis in the plots in Fig. D.3. For most of the subfigures in Fig. D.3, a hot electron temperature has been used which is comparable to the temperature determined from fits to experimental data (see section 4.3.1).

Hot Electron Divergence and Target Thickness Analyzing the different subfigures in Fig. D.3, a few observations can be made: In general, the relative strength of S-polarized TR and SR increases in the calculations with increasing divergence Δ_ψ (i.e. width of the angular momentum distribution) of the hot electron current. Here, a divergence (half angle) between 7° and 40° is reasonable. This range covers the different hot electron divergence values determined from K_α emission measurements [58, 195, 196], from measurements of the electron beam spatial profile with a scintillator [197] or layered image plates [198] and from rear surface COR measurements [66, 72, 73]. Furthermore, in [195] an overview over different published experiments is given which shows that the electron beam divergence increases with laser intensity. Such a divergence increase with laser intensity would fit very well to the slight increase of the polarization ratio with laser intensity which has been observed in the experiment for the 400 nm and 2 μ m thick target (see Fig. 4.10). Furthermore, the calculated polarization ratio of TR and SR increases with target thickness as a comparison of Fig. D.3d, Fig. D.3h, and Fig. D.3j shows. In case of a similar hot electron divergence, the

COR emission spot at the target rear surface is larger for thicker targets. Hence, the increase in polarization ratio with target thickness might be explained by a stronger spatial overlap (and hence interference) in thicker targets of the radiation emitted by electrons traveling in different directions. These results are in good agreement with the experimental results plotted in Fig. 4.10b, where an increase of the polarization ratio with target thickness and COR emission spot size has been detected.

TR or SR? The COR calculations results plotted in Fig. D.3 indicate that SR is probably the dominating emission process in the experiments of this thesis and not TR. The polarization ratio of the calculated TR is too low for reasonable simulation parameters to fit to the experiment. Based on the results of section 4.3, it seems less likely that the actual hot electron temperature in the experiment was substantially higher than the estimated value of $T_h \approx (292 \pm 22)$ keV. However, if the hot electron temperature has been underestimated by a factor of two, the calculated polarization ratio of TR becomes comparable to the polarization characteristics observed in the experiment for a divergence between $\Delta\psi = 20^\circ$ and $\Delta\psi = 40^\circ$, as Fig. D.3c, Fig. D.3f, and Fig. D.3i indicate. However, for such a large divergence, the hot electron beam diameter at the target rear surface (and hence the COR's source size) would be much larger for the $2\mu\text{m}$ and $8\mu\text{m}$ thick target than what was observed in the experiment (see section 4.1.2.1 and section 4.4.1). To finally resolve if rather SR or TR was the dominating emission mechanism in the experiment, a precise measurement of the hot electron temperature together with an absolute measurement of the COR's source size (as discussed in the next paragraph) would be beneficial. In that way, the range of reasonable parameter values in the COR polarization calculations could be narrowed.

Hot Electron Beam Size and Temperature For the 400 nm and $2\mu\text{m}$ thick targets, the calculation results plotted in Fig. D.3b and Fig. D.3g suggest that the initial size of the electron beam, which is then enlarged due to divergence, was probably below $1\mu\text{m}$. Hence, the hot electron beam diameter at the target rear surface is comparable to (or even smaller than) the resolution limit of the $(520 \pm 20)\text{ nm}$ camera ($d_{\text{lim}} = 1.2\mu\text{m}$) for the 400 nm and $2\mu\text{m}$ thick target. For example, the relative amount of S-polarization in the calculated TR and SR is too low to fit to the polarization ratio observed in the experiment if a larger electron beam diameter of $2r_0 = 1.2\mu\text{m}$ is assumed (see Fig. D.3d and Fig. D.3h). In contrast to the thinner targets, an electron beam diameter of $2r_0 = 1.2\mu\text{m}$ works sufficient well to explain the measured polarization ratio of COR emitted from the $8\mu\text{m}$ thick target if SR is the dominating emission process (see Fig. D.3j). If one compares the COR calculations for different electron beam diameters in Fig. D.3e, Fig. D.3g, and Fig. D.3h, it can be seen that the polarization ratio decreases with an increasing initial electron beam size r_0 . This might be related to a stronger overlap for larger r_0 which results in a more pronounced interference of COR emitted by electrons propagating in different directions. Looking at Fig. D.3a, Fig. D.3b, and Fig. D.3c, it can be seen that the polarization ratio E_S/E_P of SR decreases with increasing hot electron temperature T_h . For TR, the calculations suggest a reversed behavior as the polarization ratio E_S/E_P of TR increases with T_h .

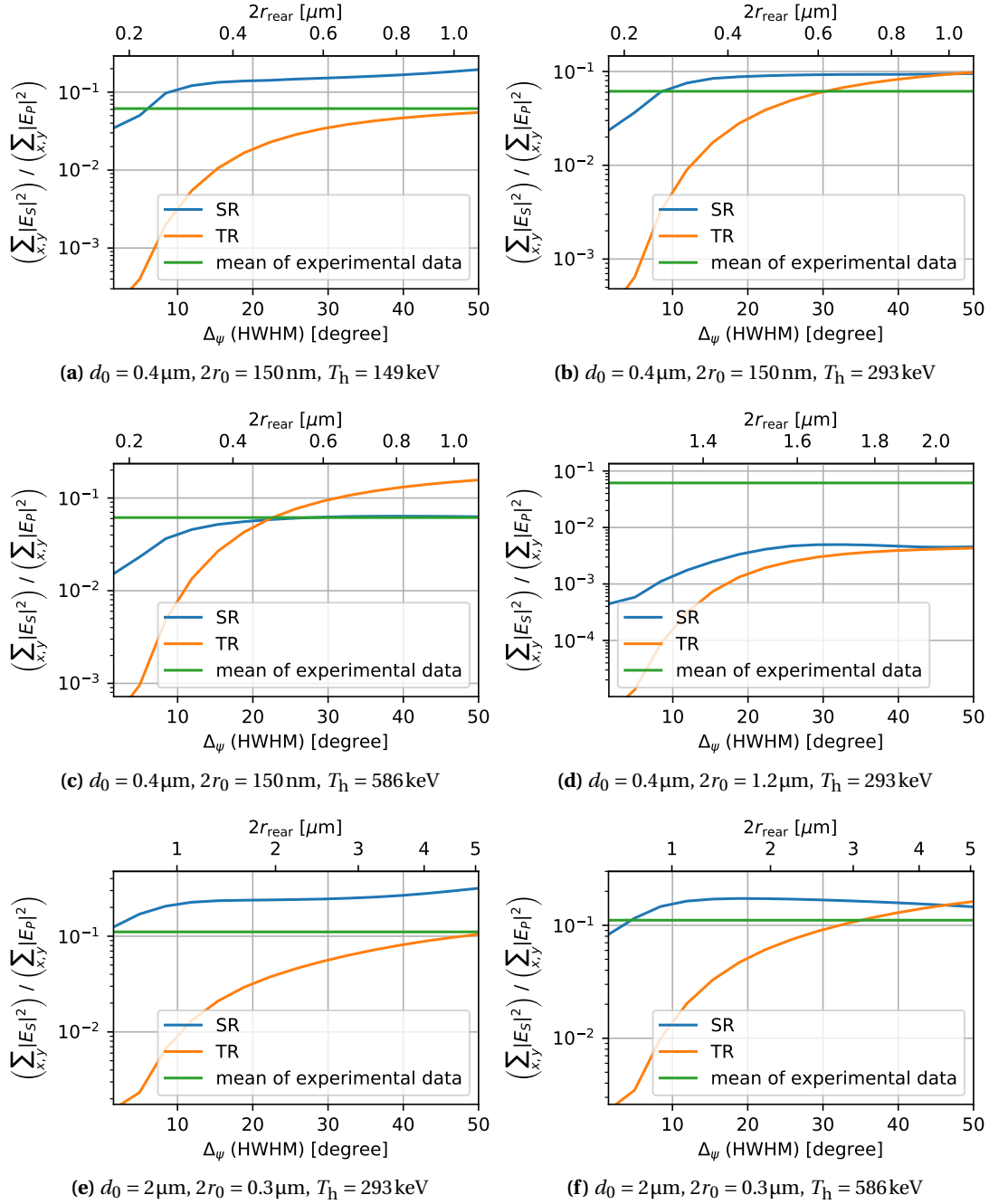


Figure D.3.: Ratio of S-polarized (perpendicular to optical table) COR radiation energy at 515 nm to P-polarized (parallel to optical table) COR radiation energy at 515 nm as a function of the width Δ_ψ of the angular momentum distribution (i.e. the divergence) of the hot electron current. The optical table is parallel to the yz-plane in Fig. 2.2. The plotted polarization ratio $E_S/E_P = \sum_{x,y} E_S(x,y) / \sum_{x,y} E_P(x,y)$ has been calculated from Eq. D.17 for TR (orange line) and from Eq. D.18 for SR (blue line). As specified in the subfigure captions, E_S/E_P is plotted for different parameter combinations of d_0 , T_h , and r_0 . Additionally, the mean polarization ratio of the experimental data is plotted for the respective target thickness d_0 as a green horizontal line. The horizontal plot axis (Δ_ψ) extends from 3° to 50° .

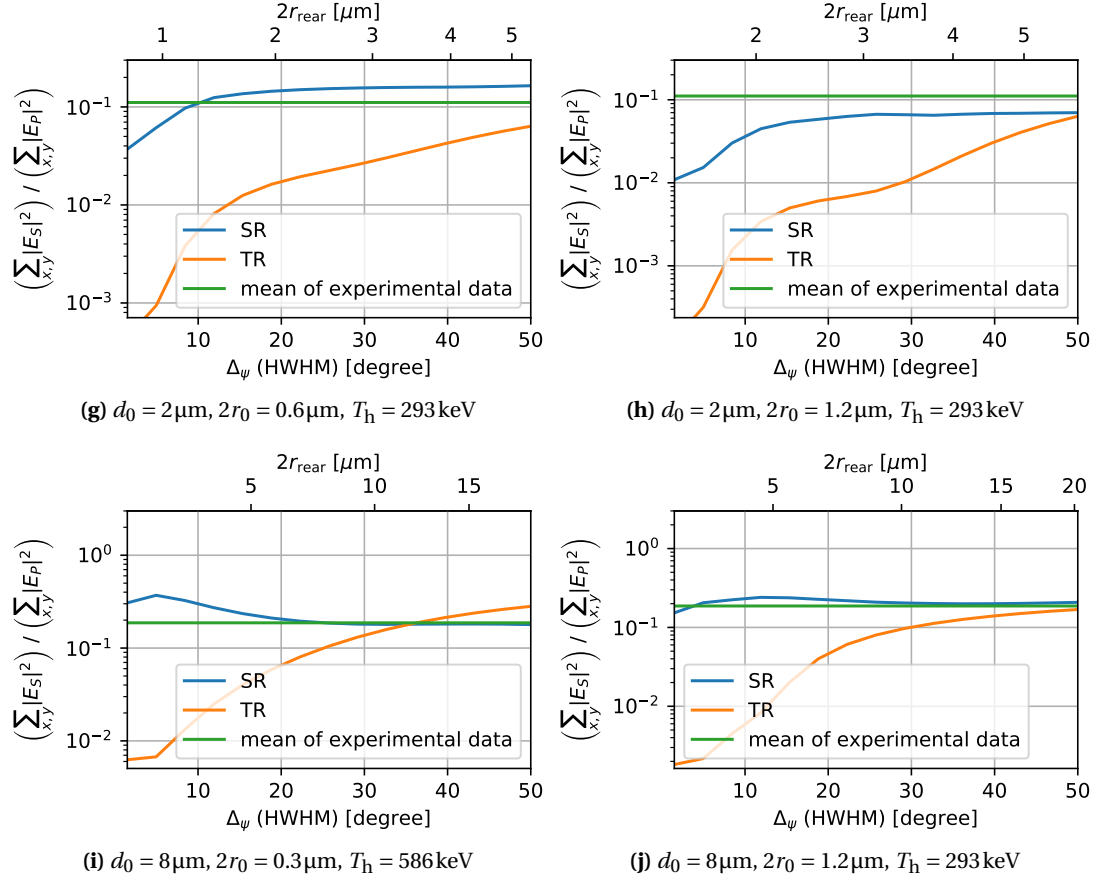


Figure D.3.: Ratio of S-polarized (perpendicular to optical table) COR radiation energy at 515 nm to P-polarized (parallel to optical table) COR radiation energy at 515 nm as a function of the width Δ_ψ of the angular momentum distribution (i.e. the divergence) of the hot electron current. The optical table is parallel to the yz -plane in Fig. 2.2. The plotted polarization ratio $E_S/E_P = \sum_{x,y} E_S(x,y) / \sum_{x,y} E_P(x,y)$ has been calculated from Eq. D.17 for TR (orange line) and from Eq. D.18 for SR (blue line). As specified in the subfigure captions, E_S/E_P is plotted for different parameter combinations of d_0 , T_h , and r_0 . Additionally, the mean polarization ratio of the experimental data is plotted for the respective target thickness d_0 as a green horizontal line. The horizontal plot axis (Δ_ψ) extends from 3° to 50° .

E. Additional Experimental Data

To study electron transport in high-intensity laser-solid interaction, the POLARIS laser was focused onto thin Al target foils. The optical rear surface radiation emitted by hot electrons, which are accelerated by the laser field at the target front side, has been measured with the experimental setup sketched in Fig. 3.1. In this chapter, additional experimental data and plots are shown to serve as a supplement to the experimental data discussed in chapter 4. The experimental data has been described, analyzed and discussed in chapter 4 in detail. Therefore, only a brief description of the figures presented in this chapter is given.

In Fig. E.1, some exemplary spatial COR intensity and polarization distributions are plotted for different target thicknesses. Fig. E.1 shows the experimental data of Fig. 4.1 again, but now a linear color scale has been used to display spatial COR intensity distribution. The experimental data plotted in Fig. E.1 has been calibrated according to the procedures described in section 3.3. The characteristics of the laser pulse, which induced the emission of the measured COR, are specified in the heading of each subfigure. Moreover, the horizontal angle $\varphi_{\text{parabola}}$ of the parabola which focuses the laser pulse on the target is stated in the subfigure heading. Each subfigure contains four color plots. The first, third, and fourth plot of every subfigure show the spatially resolved COR intensity in different spectral regions. The camera (see Fig. 3.1 for the experimental setup) is specified in the heading of each color plot according to the spectral range which is investigated by this camera. The second plot of each subfigure shows the polarization characteristics by plotting the ratio $|E_S|/|E_P|$ of the absolute electric field strength at (520 ± 20) nm for the two measured polarization directions (horizontal (E_P) and vertical (E_S) to the optical table or to the y-axis according to Fig. 3.1). The imaged rear surface COR emission spot is oriented as if one would look directly at the target rear side with the coordinate system specified in Fig. 2.2. The scaling of the x- and y-axes has been calibrated. However, the offset of the x- and y-axes has not been calibrated. Instead, a white line is plotted which acts as a y-axis-reference as it refers to a fixed position at the target rear surface.

Similar to Fig. 4.1 and Fig. E.1, exemplary spatial COR intensity and polarization distributions are plotted in Fig. E.2 for different target thicknesses. The figure composition, axis labels and plot headings of Fig. 4.1 has been described in section 4.1 and in a reduced form in the last paragraph. This description holds also true for Fig. E.2. The experimental data plotted in Fig. E.2 has been calibrated according to the procedures described in section 3.3.

The Position variations of the COR emission spot seen in Fig. E.2 are due to pointing fluctuations of the POLARIS laser but also due to realignment of the focusing parabola angle. This realignment was sometimes necessary to adjust the position of the COR emission spot to be imaged onto the entry slit of the imaging spectrometer.

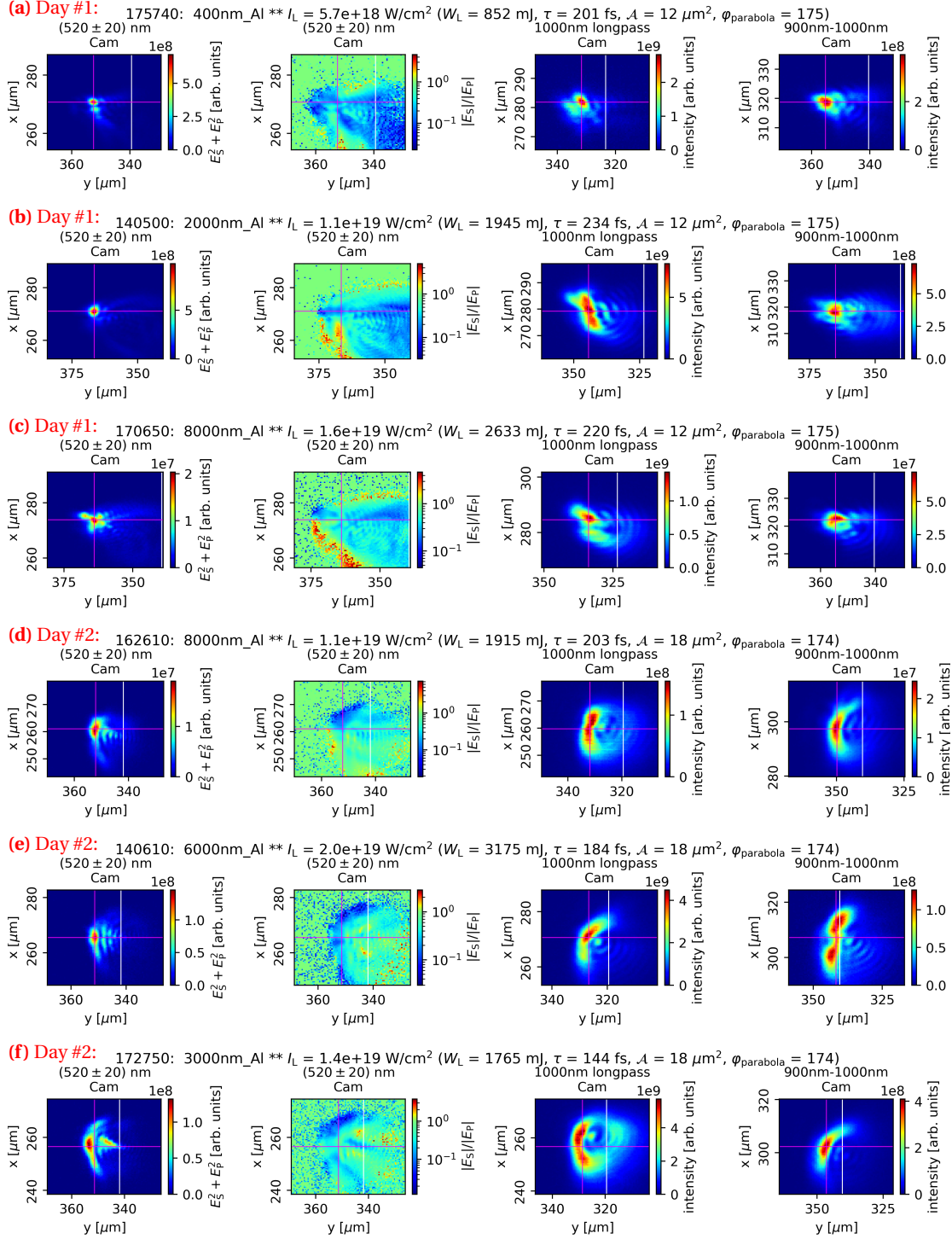


Figure E.1: Plots of the intensity I and polarization characteristics of the COR measured on two different days. The Al target thickness is specified together with the laser parameters and the horizontal angle of the focusing parabola (in arbitrary units) in the heading of each subfigure, which consists of four color plots. The underlying camera is specified in the plot heading. A magenta crosshair marks the center of mass (c.o.m.) of the region where the measured intensity I fulfills $I > I_{\text{max}}/2$. The x- and y-axes are not offset calibrated. Therefore, the white line acts as a y-axis-reference because it refers to a fixed position at the target rear surface.

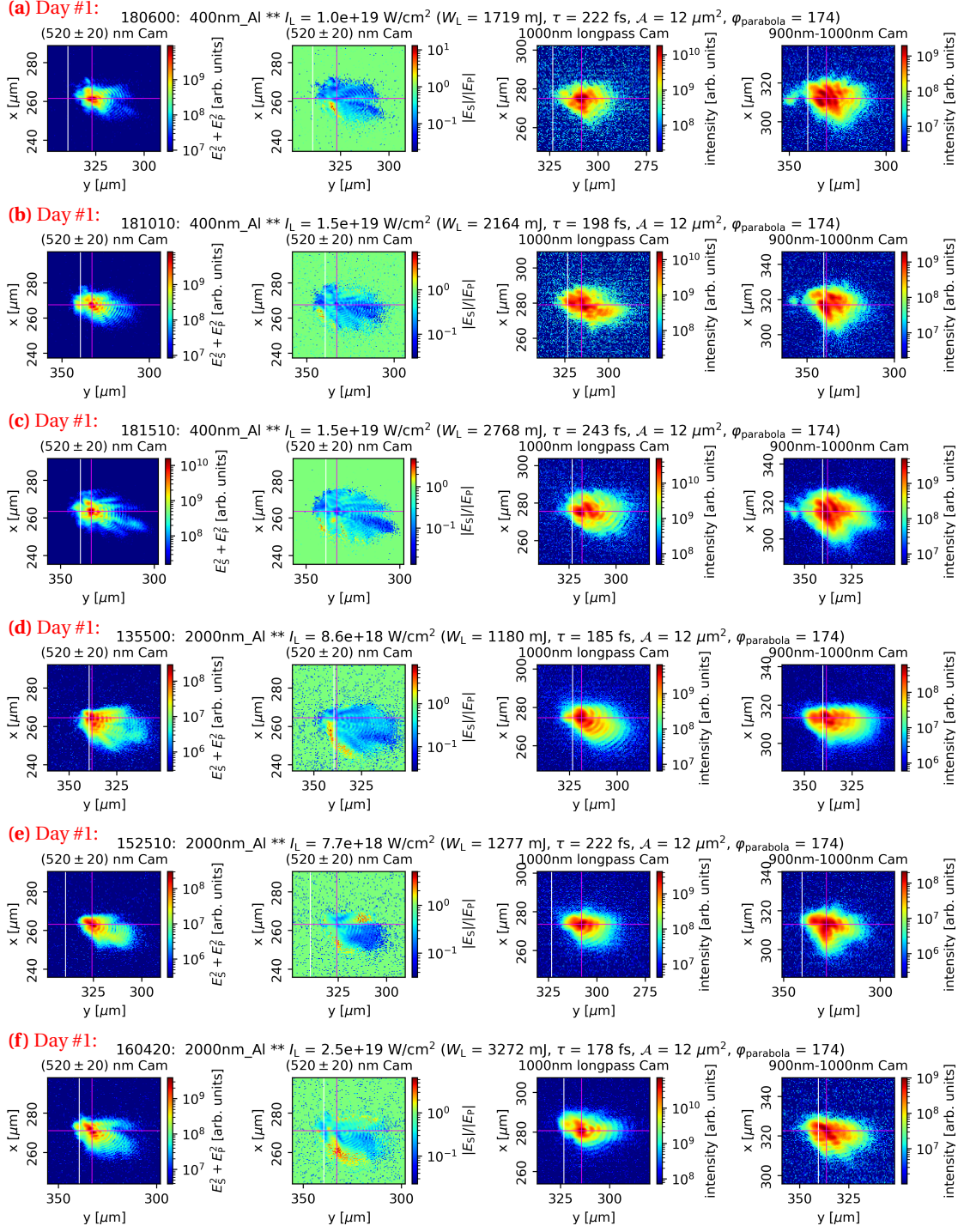


Figure E.2: Plots of the intensity I and polarization characteristics of the COR. To illustrate the changes for consecutive shots, COR data from three different laser shots is shown for every target thickness. The Al target thickness is specified together with the laser parameters and the horizontal angle of the focusing parabola (in arbitrary units) in the heading of each subfigure, which consists of four color plots. The underlying camera is specified in the plot heading. A magenta crosshair marks the center of mass (c.o.m.) of the region where the measured intensity I fulfills $I > I_{\text{max}}/2$. The x- and y-axes are not offset calibrated. Therefore, the white line acts as a y-axis-reference because it refers to a fixed position at the target rear surface. The figure continues on the next page.

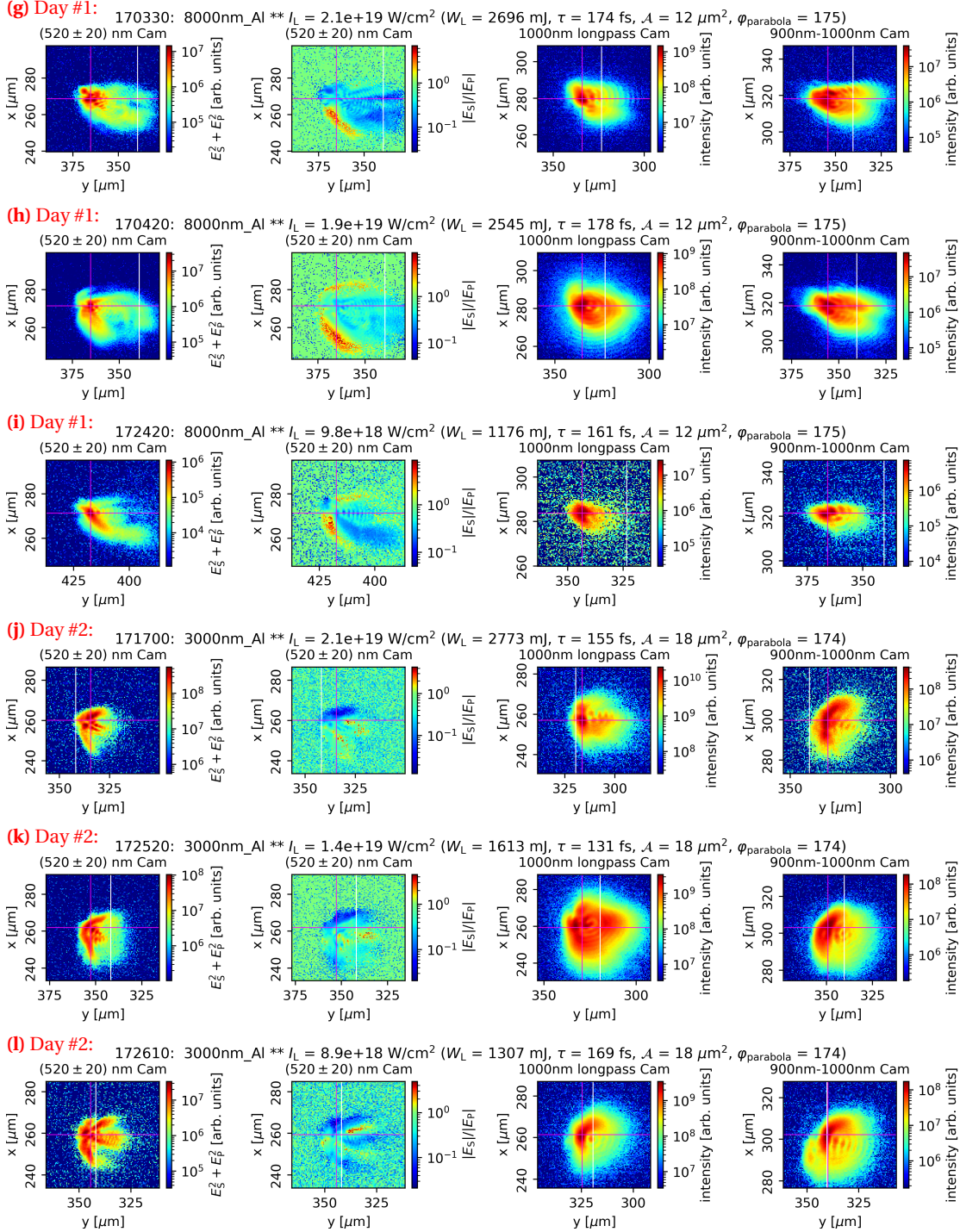


Figure E.2.: Plots of the intensity I and polarization characteristics of the COR for different target thicknesses and experiment days. For every target thickness, COR data from three different laser shots is shown. The Al target thickness is specified together with the laser parameters in the heading of each subfigure, which consists of four color plots. The underlying camera is specified in the plot heading. A magenta crosshair marks the center of mass (c.o.m.) of the region where the measured intensity I fulfills $I > I_{\text{max}}/2$. The x- and y-axes are not offset calibrated. Therefore, the white line acts as a y-axis-reference because it refers to a fixed position at the target rear surface. The figure continues on the next page

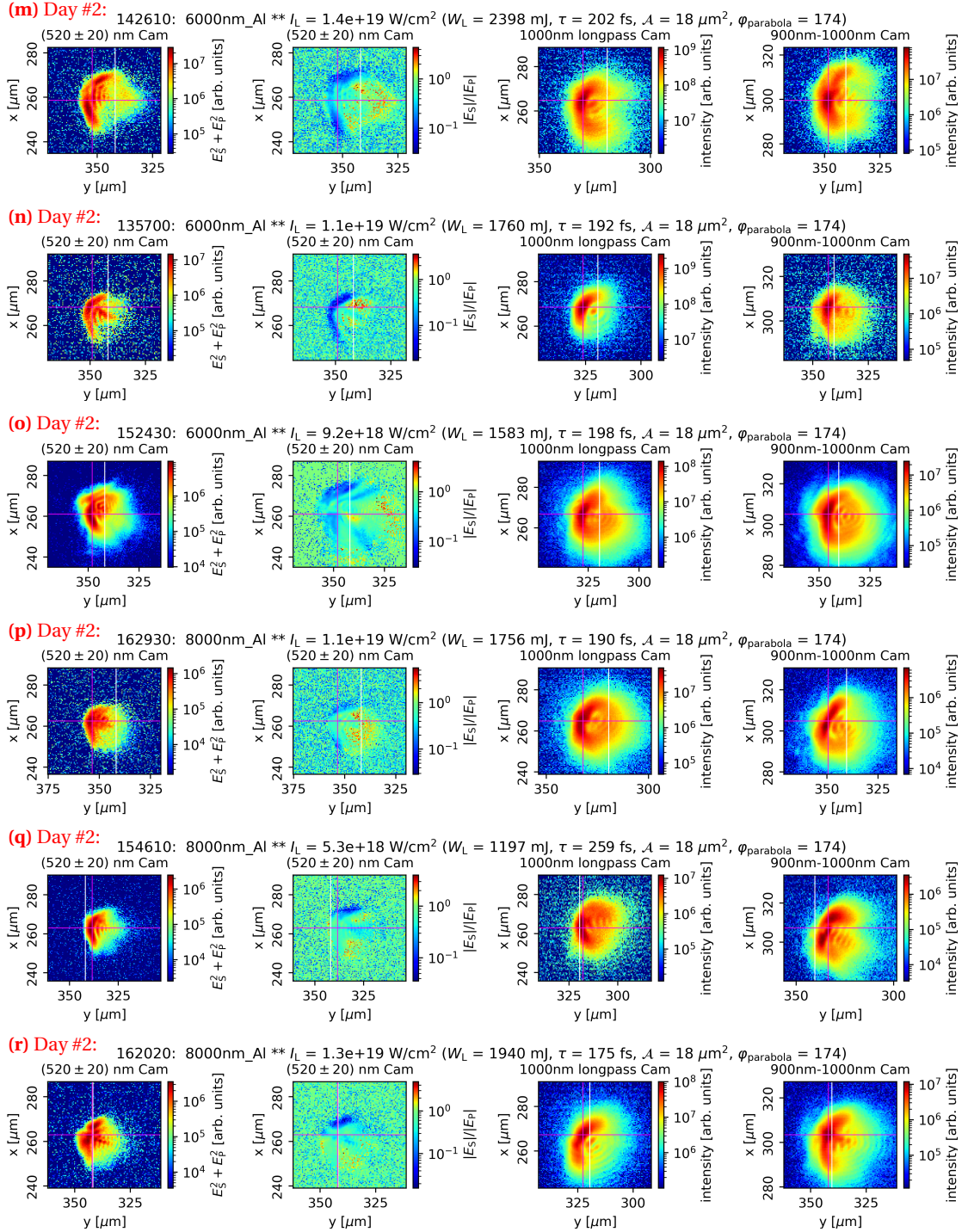


Figure E.2.: Plots of the intensity I and polarization characteristics of the COR for different target thicknesses and experiment days. For every target thickness, COR data from three different laser shots is shown. The Al target thickness is specified together with the laser parameters in the heading of each subfigure, which consists of four color plots. The underlying camera is specified in the plot heading. A magenta crosshair marks the center of mass (c.o.m.) of the region where the measured intensity I fulfills $I > I_{\text{max}}/2$. The x- and y-axes are not offset calibrated. Therefore, the white line acts as a y-axis-reference because it refers to a fixed position at the target rear surface.

As discussed in section 4.2, the total emitted COR energy W_{COR} per laser shot, is a relatively robust measure of COR. W_{COR} is proportional to the total pixel count of the camera, which has been calibrated according to the procedures described in section 3.3. The W_{COR} measured with the three different cameras on experiment day #2 is plotted in Fig. E.3 for the different target thicknesses as a function of laser intensity.

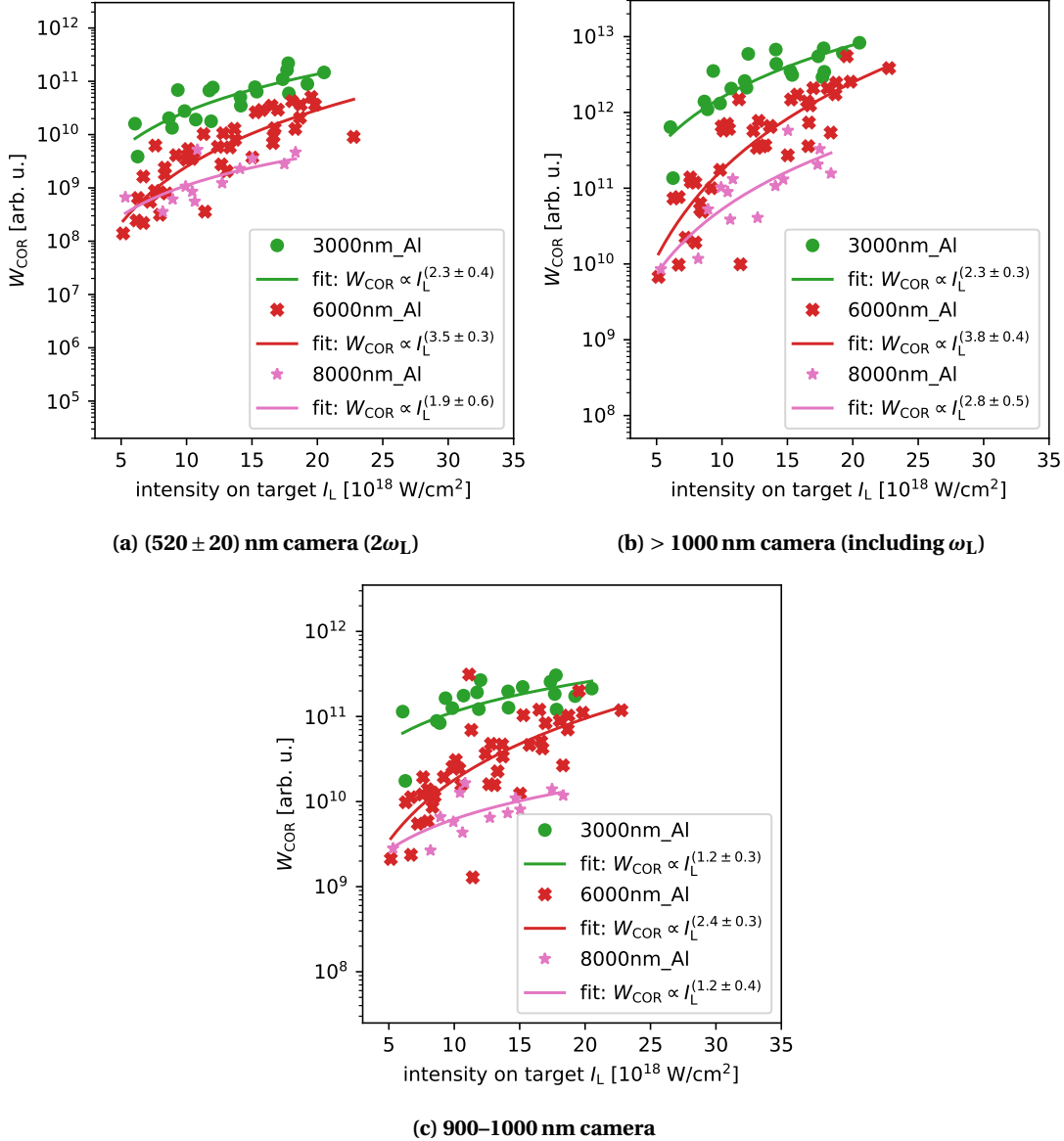


Figure E.3.: The total COR energy W_{COR} emitted per laser shot in different spectral ranges (i.e. the total pixel count of the calibrated (see section 3.3.1) camera) as a function of the laser intensity on the target front surface. The spectral range is specified in the subfigure heading. Every data point has been extracted from the COR images acquired for this particular laser shot on experiment day #2. The COR energy W_{COR} is plotted for the different investigated target thicknesses. Moreover, the function $W_{\text{fit}} = G \cdot I_L^{\Xi}$, with the variable parameters G and Ξ , has been fitted to the measured $W_{\text{COR}}(I_L)$ as specified in the legend.

Selbstständigkeits- und Nutzungserklärung

Ich erkläre, dass ich die vorliegende Masterarbeit selbständig und nur unter Verwendung der angegebenen Hilfsmittel und Quellen angefertigt habe. Aus fremden Quellen übernommene Gedanken, Werte und Zitate sind als solche deutlich kenntlich gemacht. Die Masterarbeit ist bisher weder im In- noch im Ausland in gleicher oder ähnlicher Form als Prüfungsleistung verwendet worden oder als Veröffentlichung erschienen. Die eingereichte schriftliche Fassung entspricht der auf dem elektronischen Speichermedium.

Seitens des Verfassers bestehen keine Einwände, die vorliegende Masterarbeit für die öffentliche Nutzung zur Verfügung zu stellen.

Ort, Datum

Sebastian Hell